AHRTI Air-Conditioning, Heating and Refrigeration Technology Institute

Final Report

AHRTI Report No. 06030-02

NOVEL MATERIALS FOR HEAT EXCHANGERS

Phase II Final Report

January 2013

Anthony M. Jacobi (PI)
Kashif Nawaz
Jessica Bock

AIR CONDITIONING AND REFRIGERATION CENTER
MECHANICAL SCIENCE AND ENGINEERING
UNIVERSITY OF ILLINOIS
1206 West Green Street
Urbana, IL 61801

a-jacobi@uiuc.edu
ph. 217/333-4108

Prepared for

AIR-CONDITIONING, HEATING AND REFRIGERATION TECHNOLOGY INSTITUTE, INC
2111 Wilson Boulevard, Suite 500, Arlington, Virginia 22201-3001

DISCLAIMER

This report was prepared as an account of work sponsored by the Air-Conditioning, Heating and Refrigeration Technology Institute, Inc. (AHRTI). Neither AHRTI, its research program financial supporters, or any agency thereof, nor any of their employees, contractors, subcontractors or employees thereof - makes any warranty, expressed or implied; assumes any legal liability or responsibility for the accuracy, completeness, any third party's use of, or the results of such use of any information, apparatus, product, or process disclosed in this report; or represents that its use would not infringe privately owned rights. Reference herein to any specific commercial product, process, or service by trade name, trademark, manufacturer, or otherwise, does not necessarily constitute nor imply its endorsement, recommendation, or favoring by AHRTI, its sponsors, or any agency thereof or their contractors or subcontractors. The views and opinions of authors expressed herein do not necessarily state or reflect those of AHRTI, its program sponsors, or any agency thereof.

Funding for this project was provided by (listed alphabetically):
- Air-Conditioning, Heating and Refrigeration Institute (AHRI)
- Copper Development Association (CDA)
- Heating, Refrigeration and Air Conditioning Institute of Canada (HRAI)
- New York State Energy Research and Development Authority (NYSERDA)

EXECUTIVE SUMMARY

Through earlier work on this project (*Phase I*), a literature review and analysis were completed to identify new materials holding promise for use in heat exchangers. That work also identified current impediments to using these materials. Two findings of that earlier work were: (1) metal and carbonaceous foams have potential for use in heat exchangers; and (2) the main technical barrier to their application is a lack of heat transfer and pressure drop performance data. The current study (*Phase II*) provides performance data necessary for a more complete assessment of foams as heat exchanger materials.

Although a review of the literature was completed in *Phase I*, new information has since become available. In this *Phase II* report, the literature review is updated with a special focus on the structure of metal foams in Chapter 1, an updated review of pressure-drop performance in Chapter 2, and an updated review of heat transfer performance in Chapter 3. Ancillary reviews of the thermal conductivity of metal foams and their performance as compared to conventional fins are provided in Appendices F and G, respectively.

In Chapter 1 an effort to understand and quantify the geometry of metal foams is presented. While the Kelvin unit-cell geometry is almost universally adopted for foam modeling, the Weaire-Phelan (WP) unit cell geometry is known to possess a lower Gibbs energy. New X-ray micro-computed tomography (μCT) results show that neither the Kelvin cell nor the WP cell is in full agreement with the real metal foam geometry. Discrepancies exist because metal foams do not reach equilibrium configurations prior to solidification. The WP cell is shown to be more realistic than the Kelvin model. The μCT results are also used to find information such as ligament length, orientation, and diameter. These data are then used to better understand water retention, and to develop pressure-drop and heat transfer correlations.

An evaluation of water drainage in metal foams shows that foams with pore diameters below about 2 mm retain water with very little drainage; however, for pore diameters above about 3 mm, water readily drains from metal foams. Foam porosity and geometry are very important to the drainage behavior in metal foams. A comparison of drainage behavior shows foam with a large pore diameter to hold less water than does a louvered fin.

Heat transfer and pressure drop behavior are key to the design of heat exchangers, and the current work provides a set of general, accurate curve fits for predicting the friction factor and Colburn j factor for metal foams. The curve fits are based on data from wind tunnel experiments with foams of varying pore diameter for air face velocities ranging from 0.5 m/s to 6 m/s. The friction factor and Colburn j factors are fit with relative RMS deviations of 14.9% and 4%, respectively. Under dry-surface conditions with fixed pressure gradient, the heat transfer per unit volume, per unit temperature difference for metal foams with a large pore diameter is almost twice that of a louver fin. Under wet-surface conditions, the pressure drop for foams with a large pore diameter increases slightly, but the heat transfer is significantly higher. Under frosted-surface conditions, foam heat transfer performance drops precipitously. Metal-foam heat exchangers might be attractive for dehumidifying applications. A more detailed summary, including the friction factor and Colburn j factor correlations, is provided in Chapter 4.

NOMENCLATURE

Symbols

A_{fr}	Frontal area (m^2)
A_{min}	Minimum flow area (m^2)
c_p	Specific heat at constant pressure (J/kg-K)
C	Inertia coefficient
D_h	Hydraulic diameter (m)
D_f	Fiber diameter (m)
D_p	Pore diameter (m)
$\Delta P/L$	Pressure drop per unit length (Pa/m)
G	Mass flux (kg/s-m^2)
$\bar{h}$	Average heat transfer coefficient (W/m^2-K)
j	Colburn factor
k_{eff}	Effective thermal conductivity (W/m-K)
k_{fluid}	Fluid thermal conductivity (W/m-K)
K	Permeability ($m^{1/2}$)
L_h	Characteristic length of heated surface (m)
LMED	Log mean enthalpy difference (C)
LMTD	Log mean temperature difference (C)
Nu	Nusselt number
PPI	Pores per inch
Pr	Prandtl number
q	Heat transfer rate (W)
Re_{Dh}	Reynolds number based on hydraulic diameter
Re_K	Reynolds number based on permeability
$\bar{T}$	Average temperature (C)
V	Face velocity (m/s)

Greek letters

ε	Porosity
$\bar{\rho}$	Average density (kg/m^3)
$\bar{\mu}$	Average dynamic viscosity (N-s/m^2)
η_f	Fin efficiency
η_o	Surface efficiency

Subscripts

air,in	Inlet air
air,out	Outlet air

TABLE OF CONTENTS

Chapter 1 — Aluminum metal foam structure and water retention

1.1 Introduction

In many applications, air-cooling heat exchangers operate with the heat-transfer surface below the dew point of the air, in order to dehumidify the conditioned air. Condensate accumulates on the surface and is retained by surface tension unless removed by gravitational or air-flow forces. Retained condensate profoundly affects the heat transfer and pressure drop performance and plays an important role in the overall performance of the air-conditioning system. It also has implications on air quality: condensate blown off the heat exchanger surface can directly affect occupant comfort, and water provides a medium for biological activity on air-handling surfaces. With growing concerns about the quality of conditioned air, designers often strive for heat exchanger designs that provide efficient condensate drainage in off-cycle operation. Unfortunately, although there have been numerous studies of the effect of condensate retention on the thermal–hydraulic performance of heat exchangers, very little research in the open literature has addressed the drainage behavior, especially the drainage under off-cycle conditions. This concern becomes more important when considering heat exchangers having porous media with a complex, three-dimensional geometry. Metal foams have been found to exhibit promising heat transfer for use on the air side of heat exchangers, due to their complex geometry and high surface-area-to-volume ratio. Both of these effects enhance the heat transfer performance, but at the same time presumably due to this highly complex structure, condensate retention may be problematic.

Early studies of liquid retention on heat transfer surfaces were reported in 1948 by Katz and Geist [1], who conducted experiments with pure R-12, n-butane, acetone, and water vapor, supplied by a boiler and condensed on six horizontal finned tubes in a vertical column. Assuming gravity the dominant factor, they calculated the values of the heat coefficient from Nusselt theory and found that deviations between experimental and theoretically calculated coefficients for the top tube were less than 14% for most fluids, with only a 5% discrepancy for acetone. While it is not possible to simply extend their findings to the complex geometries used in contemporary heat exchangers or to situations with binary or multi-component mixtures, their early experiments and modeling demonstrate the importance of understanding drainage behavior in order to predict thermal performance.

Karkhu and Borovkov [2], Rifert *et al.* [3], Honda *et al.* [4], and Rudy and Webb [5] focused their research on the surface tension force during condensate retention. They proposed that surface tension could be the dominant force in condensate drainage for the integral-fin tube of their studies. Rudy and Webb [5] conducted static measurements of the amount of condensate forming on an integral-finned tube. Their model to predict the amount of the surface flooded during condensation on a horizontal, integral-fin tube agreed with experiments to within ±10% over most of the test range.

All of the above research was directed toward integral-fin tube heat exchangers, while Osada *et al.* [6] and [7] performed heat transfer and condensate visualization studies using single-fin models of flat-tube evaporators. They examined the effects of surface wettability, louver geometry, and heat exchanger inclination. Osada *et al.* [6] and [7] H. conducted research on corrugated multi-louvered fins under dehumidification and concluded that fin geometry, wettability, and the characteristics of the airflow, especially at the exit face of the heat exchanger were important factors in condensate drainage. They also found that coil inclination greatly influenced the thermal performance of an evaporator.

McLaughlin and Webb [8] examined fin geometry effects on drainage and retention characteristics using a tabletop apparatus to study a single-fin which was brazed to a plate chilled by circulating “ice-water” through a tube brazed to it. Their scheme allowed optical access to the fin during the formation and subsequent drainage of condensate. McLaughlin [9] also compared the retained water measured in their “dip test” to that measured in a wind tunnel. They weighed a dry coil, dipped it in a bucket of water, removed it from the water and began to weigh the wet coil after 15 s. The heat exchanger was allowed to drain for 120 s in the vertical position, and then a thin piece of aluminum was touched to the bottom of the core to remove water clinging to the lower manifold. They found the mass of remaining water to be within 10% of that measured in a wind tunnel. The remaining condensate (per fin) in their dip test was found to be 3% lower than that in their single-fin tests. It should be noted that all wind-tunnel experiments were conducted with the air frontal velocity of 2.4 m/s, and the dip test was conducted in quiescent surroundings.

Zhong *et al.* [14] proposed a new method to assess the condensate drainage behavior of the air side surface of the compact heat exchangers, referring to it as a *dynamic dip test*. This method provided highly repeatable data for real-time drainage. Results from experiments for more than 20 flat-tube and round-tube-and-fin heat exchangers were compared to results obtained in wind tunnel experiments. The data showed geometrical effects such as the impact of the tube type on condensate drainage. The heat exchangers retaining the most and the least condensate in a steady-state wind-tunnel test, likewise held the most and the least in a dynamic dip test. However, different amounts of water were retained on the air-side surface during dynamic dip tests and wind-tunnel experiments. They also developed a model based on gravity, surface tension and viscous effects to help understand and predict the drainage behavior of heat exchangers. The new model and experimental approach were found to be a useful in screening heat exchangers for condensate retention and for assessing off-cycle drainage behavior.

Elsherbini and Jacobi [15] developed a model for predicting the amount of condensate retained as drops on the air-side of heat exchangers operating under dehumidifying conditions. For a surface with a given surface wettability, characterized by the advancing contact angle (θ_A), the maximum diameter for a retained drop was obtained from a balance between gravitational and surface tension forces. A logarithmic function was used to describe the size-distribution of drops on fins, based on the fraction of fin-area covered by liquid. The volumes of individual drops were calculated by a geometric method for approximating the three-dimensional shapes of drops on vertical and inclined surfaces. The total volume of condensate accumulated on a coil was then found by multiplying the size-distribution and volume functions and integrating overall drop diameters. The model was successful in predicting measurements by other researchers of the mass of condensate retained on plain-fin heat exchangers. A critical fin spacing to avoid the formation of condensate bridges was also predicted.

Although prior research has shown that air-side condensate retention has an important effect on the thermal-hydraulic performance of compact heat exchangers, limited work has been reported on measuring retention and drainage from the air-side surface. One approach to such measurements is to measure the mass of a heat exchanger operating under dehumidification conditions in a wind tunnel. In an alternate method, referred to as dynamic dip testing, a heat exchanger is submerged in a tank while suspended on a mass balance; the water level in the tank is suddenly reduced and the weight of the heat exchanger is measured as a function of time. This method is simple, inexpensive, and relatively fast. By comparing dynamic-dip-test data to data from wind-tunnel experiments with the same specimens, researchers have established the general value of dynamic dip testing as a screening tool.

Although dynamic dip testing has been demonstrated as to be relatively easy method to assess condensate drainage behavior—a heat exchanger holding more water in a dip test also tends to hold more condensate in a wind-tunnel experiment—Liu and Jacobi [16] found the reliability of the method to be affected by many factors which are often ignored. Dip test results as well as retention visualization for 22 heat exchanger specimens with different configurations and surface wettability were reported and discussed with relevant dip test and wind-tunnel experimental data available from the literature. The data demonstrate that when dealing with round-tube heat exchangers with unusual wettability (hydrophilic or hydrophobic), dip tests can sometimes give an evaluation which is counter to the results in the wind-tunnel. In terms of surface wettability, the receding contact angle (θ_R) was found to be the primary factor affecting a dip test, while the contact angle hysteresis ($\theta_A - \theta_R$) becomes more important in a condensing environment. It was observed that dip test measurement is very sensitive to the "dipping rate", or the speed at which a specimen is withdrawn from the water reservoir.

In the next section, a state-of-the art geometric characterization of aluminum metal foams will be presented, with the goal establishing the most appropriate geometric model of the metal foams. Following that, results from dynamic dip tests of metal foams will be presented, in order to assess the drainage behavior of this material.

1.2 Geometric classifications of open-cell metal foams

1.2.1 Introduction.

The problem of accurately describing the geometrical structure of foams has a long history. In 1887 Lord Kelvin proposed a solution to what has become known as 'the Kelvin problem' [22], how to partition three-dimensional space into cells of equal volume with the smallest possible surface area. Such a configuration would represent the minimum-surface-energy geometry, and would be thermodynamically preferred for equilibrium closed-cell foams of vanishing liquid content. Since Kelvin proposed the problem, the search for a minimum-surface-area unit cell has drawn the attention of many researchers [22-34]. The idealized geometry of metal foams has been connected to the geometry of bubbles, soapy froths, and wet foams and has resulted in a body of literature replete with foam descriptions [35-43].

Kelvin conjectured that the tetrakaidecahedron satisfied the requirements of a space-filling polyhedron that with minimum surface area. The tetrakaidecahedron consists of six square and eight hexagonal faces, and is constrained by Plateau's laws for equilibrium structures [44]. The Kelvin unit cell, shown in Figure 1.1, can also be considered a body-centered-cubic (bcc) structure with slightly curved faces, which allow the cell to satisfy Plateau's rules.

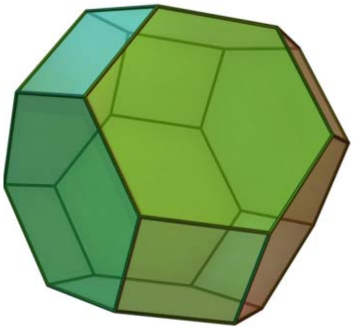

Figure 1.1[58]: Kelvin unit cell

More than a century after Kelvin's proposed solution, Weaire and Phelan introduced a counter-example that succeeded in reducing the surface energy of the unit cell [25]. The Weaire-Phelan (WP) unit cell consists of multiple, irregular polyhedra of equal volume: six 14-sided polyhedra and two 12-sided polyhedra, as shown in Figure 1.2. It was derived from a tetrahedrally close-packed (tcp) structure, a family of structures that are commonly observed in chemical clathrates [28] and was optimized using the "Surface Evolver" package of Brakke [45] to determine the curvature required to minimize surface area. With advances in computational methods, increasingly complicated unit cells can be analyzed in pursuit of improved solutions to the Kelvin problem [29].

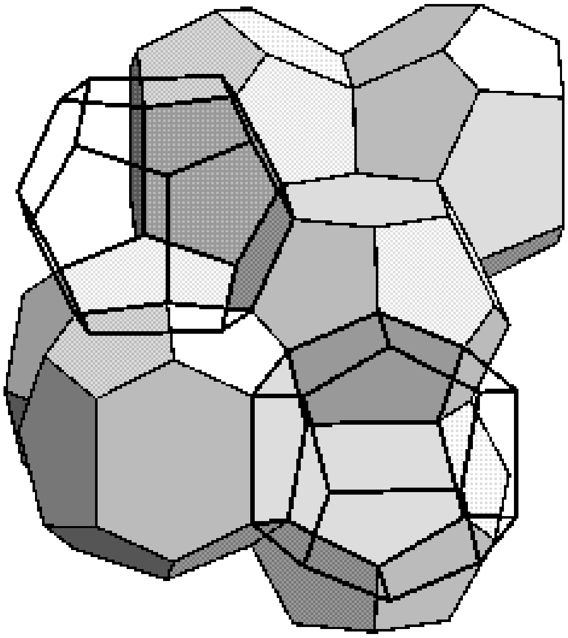

Figure 1.2[46]: Weaire-Phelan unit cell

The isoperimetric quotient (*IPQ*), as defined in Equation 1.1, is the figure of merit for area minimization at fixed volume (or volume maximization at fixed area). The volume and surface area of a single unit cell are V_{unit} and A_{unit}, respectively. The WP unit cell improved *IPQ* as compared to the Kelvin unit cell, having about 0.3% less surface area per unit volume. However, there is no proof that this structure provides a global minimum.

$$IPQ = \frac{36\pi V_{unit}^2}{A_{unit}^3} \tag{1.1}$$

It is important to note that although the WP unit cell has pores of equal volume, they are not of equal pressure, where pore pressure and volume are based on a soapy-film model in which each pore is enclosed by a thin film of soap. Kelvin's model exhibits pores of both equal pressure and volume. Kusner and Sullivan compared the WP and Kelvin unit cells and conjectured that the Kelvin unit cell is the best model for foam with equal volumes and equal pressures [28].

New combinations of polyhedra to form space-filling unit cells are constantly being developed and analyzed [23, 29, 32, and 35], but, to date, no structure has been demonstrated to have an *IPQ* superior to that based on the Weaire-Phelan unit cell.

Prior research in the metal foam literature has generally regarded the Kelvin unit cell as the idealized foam structure best describing metal foams [18, 20, 43, and 47]. This unit cell is relatively easy to model as a single pore described by a regular polyhedral. The Weaire-Phelan unit cell has a significantly more complicated geometry owing to the fact that it is comprised of eight irregular polyhedral pores. However, vertex data are available for construction of the individual pores [46], from which a unit cell may be modeled. Due to the more complicated geometry of the WP unit cell, many researchers have continued to adopt the Kelvin model for simplicity [43].

The geometry of foams remains an active area of research, and recent software developments [45] have improved the modeling of space-filling polyhedra and led to the introduction of new, idealized unit cells to describe foam structures [23,35]. Many of the unit cells that have been proposed have been derived from the study of soapy froths [24, 38]. Metal foams, although formed from wet foams, are intrinsically different from these soapy froths. Metal foams are not equilibrium structures [48], because quenching or solidification of the metal occurs before the foam reaches equilibrium. Thus, the dynamics of the foam formation and solidification may play a significant role in the ultimate geometrical structure. It is currently unclear which of the extant models provides the best description of metal-foam geometry. In this work we focus on characterizing the geometry of metal foams and comparing it to the Kelvin and WP unit cells.

1.2.2 Methodology for geometric study

Some prior work has been done regarding the classification of closed-cell metal foam structures using X-rays and computed tomography (X-ray CT) [49, 57]. Work has also been published on the use of X-ray CT for characterizing polymer foams and open-celled metal foams [47, 48, 50-54]. The current approach is to obtain geometric data for several Duocel® Al-6106-T6 open-cell metal foam samples of varying porosity using X-ray CT, and to use the results for a comparison to idealized geometries.

1.2.2.1 Experimental methods for geometric study. In order to classify the geometry of the metal foam samples investigated in this study, X-ray micro-computed tomography (μCT) was employed. This technology, originally developed in 1972 as a medical imaging method [55], is currently widely used as a non-destructive method for characterizing the structure and composition of materials. Common applications of X-ray CT include stress test analysis, biological evolution and growth studies, density and composition studies, failure analysis, and oil drilling feasibility analyses [56].

X-ray CT can be performed at various resolution scales depending on the machine capabilities and sample size. The metal foam samples in this study had porosities designated by the manufacturer as 5, 10, and 20 PPI (pores per inch)[1]. Thus, the pore sizes ranged from about 1.25 mm to 5 mm, and because of the small pore size a fairly high spatial resolution was required, leading to the use of X-ray μCT. The Microscopy Suite at the Beckman Institute for Advanced Science and Technology at the University of Illinois at Urbana-Champaign granted access to the Xradia Bio MicroCT (MicroXCT-400) apparatus for collecting X-rays of several metal foam samples.

A schematic of an X-ray μCT apparatus is shown in Figure 1.3. The sample was mounted on a rotating plate between the X-ray source and the detector. X-ray images were collected as each sample rotated 194 degrees at increments of 1/8 of a degree, resulting in 1553 images per sample. A filter is placed before the camera to convert the x-ray to digital images. The camera exposure time was set to one second. A computer algorithm stores these images as two-dimensional slices, known as radiographs. The CT software can then create 3D volumetric renderings by reconstructing the CT slices (radiographs).

---

[1] The manufacturer's designation of 5, 10, and 20 PPI is not an SI unit; nevertheless, we will adopt the manufacturer's designation to avoid confusion and for convenience.

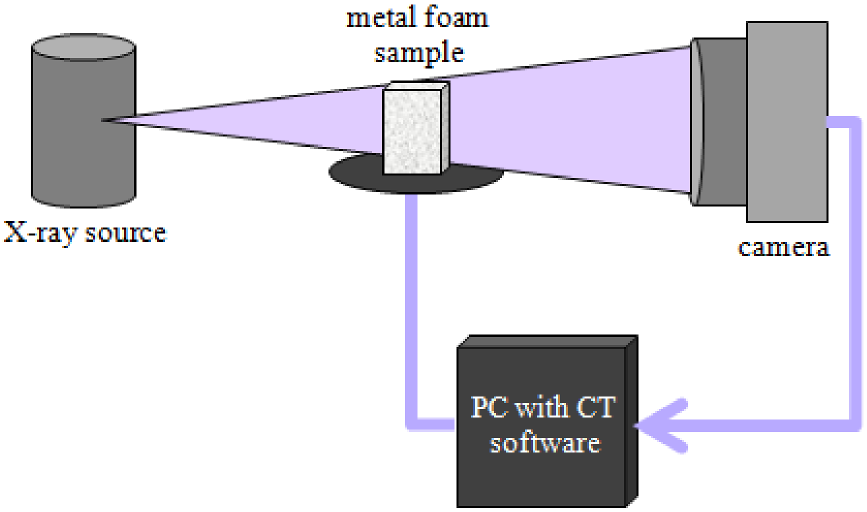

Figure 1.3: Schematic of X-ray µCT apparatus

The intensity and clarity of the x-ray images is dependent on the experimental apparatus and the density variations in the object being scanned. In this study, the X-ray power was set to the maximum of 8 Watts and 90 keV. As the metal foam samples were Al-6101-T6, the images obtained showed high contrast between the metal (2.7 g/cm^3) and the air (0.00119 g/cm^3). This sharp contrast simplified image analysis by showing the metal-air interface clearly.

1.2.2.2 Analytical methods for geometric study. Montminy *et al.* [48] describe in detail the use of software created to extract similar geometric data from the X-ray µCT images of open-cell, polyurethane foams. This software, FoamView©, created as part of doctoral thesis research on polymer foams at the University of Minnesota, is available along with a user manual as "Supplemental Material" to reference [48].

FoamView© is not commercially available, there is no technical support, nor is its use widely reported in the literature. Therefore, an independent validation was undertaken as part of this work. The FoamView© software uses as an input a group of 2D images, provided by the user, to generate a 3D reconstruction of the object being analyzed. A stick-figure model is created and modified to match the geometry of the object. In order to validate the FoamView©-generated data, faux 2D images mimicking CT slices of prescribed 3D geometries were created using standard drawing software. The 3D rendering of the reference files was then analyzed using the

FoamView© features to create a stick-figure model identical to the reference structure. From the stick-figure model, output files were generated, listing the locations of the vertices as well as vertex pairs that connect to form lines, or edges. The output files were then compared to the reference data of known vertex locations and line lengths. The FoamView© generated data proved to match the geometry of the reference files, providing confidence in the image analysis software.

FoamView© provides geometric data regarding strut length and distribution but does not report data describing the diameter, or thickness, of the struts. In order to obtain such data, the 2D X-ray slices, or radiographs, can be analyzed. The radiograph images clearly show the cross-section of the struts. The scale for these images is known, so the dimensions of the strut cross-sections can be calculated. It is important to note that the struts have triangular cross-sections. Many prior publications regarding metal foams assumed the struts to be circular cylinders [17, 18, 21, and 47]. Few publications have reported that the strut cross-sections are triangular [19].

The radiographs can also provide information about the strut distribution. The number of struts intersecting a plane can be determined within a known area for each radiograph. Multiple radiographs can be analyzed to get an average strut distribution that accounts for different locations within the foam.

From the FoamView© analysis and the examination of the radiographs, an effective description of the metal foam can be realized. The geometric data of real metal foams can then be compared to idealized unit cells and adopted in modeling applications.

1.2.3 Experimental results for geometric study

Approximately 1000 images were collected for each metal foam sample. The image sizes were 3.1 x 1.3 x 1.3 cm. Due to the file size limitations of FoamView©, only 300 of these images could be used at one time in the geometric analysis, reducing the sample size to 1.3 x 1.3 x 1.3 cm. It was assumed that this sample size could be considered representative of the entire foam sample, as the volume of a single pore is significantly smaller. This assumption was supported by comparing the results for two different samples from the same foam, as well as results for two different foams of the same PPI. The images chosen for analysis in FoamView© were selected from the center of the X-ray data set to avoid irregularities near the foam edges, such as scattering or structural damages that may have occurred in the handling or cutting of the metal foam samples.

An image analysis technique called thresholding could be used on the 2D radiographs obtained from the X-rays before uploading the images to the FoamView© software, or as part of the FoamView© analysis. By applying a threshold to the images, some of the unwanted reflections and scattering of the X-rays were eliminated. A raw image of the radiographs obtained for 10 PPI, open-celled, aluminum metal foam is shown in Figure 1.4, where the void space, or air, is shown by darker shades and the metal foam cross-sections are shown in lighter shades. The scattering and reflections of the X-rays can be seen near the edges of the foam struts where the shading becomes slightly darker.

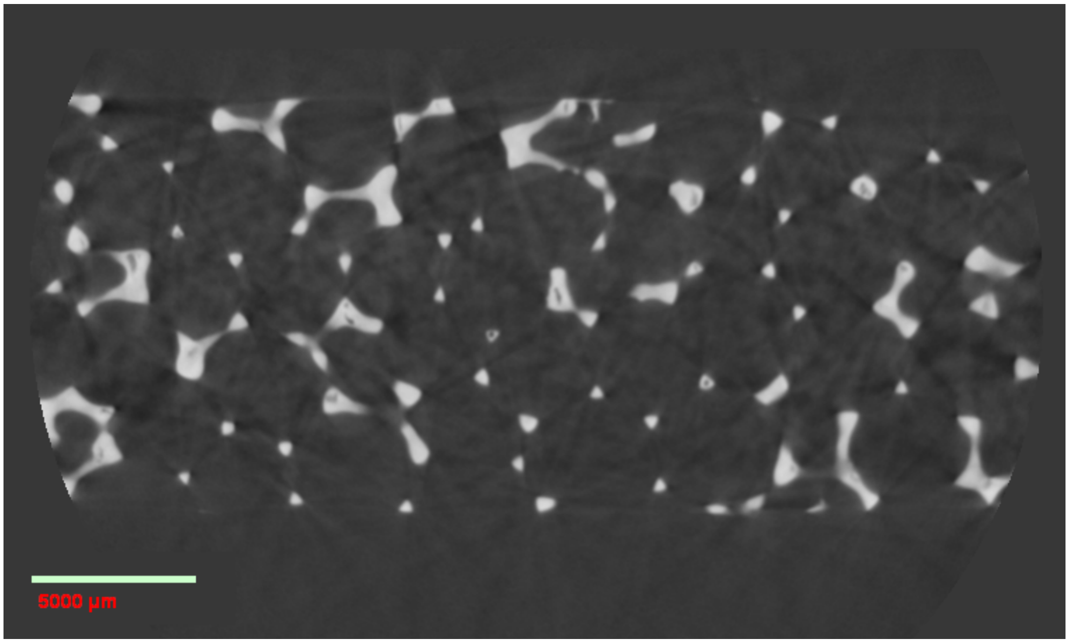

Figure 1.4: Radiograph (raw data), 10 PPI

The default images obtained from the Xradia BioCT scanner, like that shown in Figure 1.4, showed the void as dark space and the aluminum as bright space. While the FoamView© software allowed the user to specify whether the material in question was shown as black or white in the images, it was discovered that computing time decreased when the X-rays were uploaded with the void space represented by white. In order to save computing time, the radiographs images were inverted. In attempts to reduce computing requirements, thresholding was also applied to the raw images to make a clearer distinction between metal and void.

The intended use of the imaging software provided by Xradia is to view the X-ray μCT scans, converting the radiographs to a 3D rendering, and to provide alternative viewing techniques for a qualitative image analysis. There are few such tools available which allow for quantitative image analysis. In order to extract multiple measurements and qualitative data from the images, an additional software package, specializing in image analysis, was required. An example of the 3D rendering produced from the X-ray images is shown in Figure 1.5 for a 5 PPI metal foam. Due to the conical shape of the X-rays, the corners of the sample appear lighter, and slightly distorted. These extremities were not in the focal point of the x-ray and were therefore neglected during the image analysis.

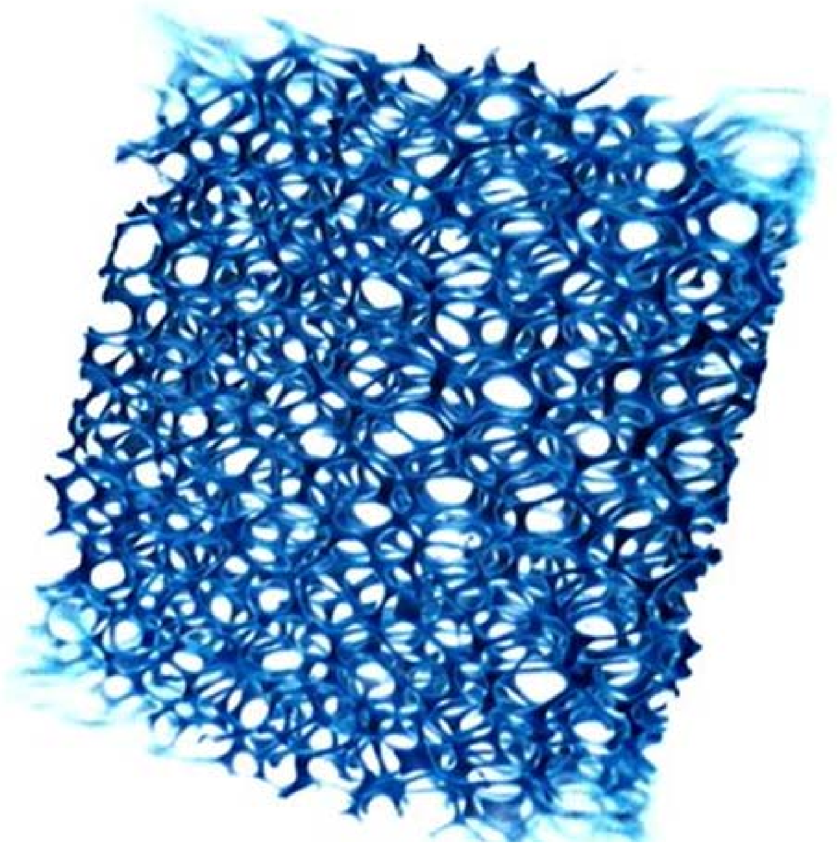

Figure 1.5: 3D rendering of X-ray CT data, 5 PPI

As previously stated, the imaging software utilized in the X-ray μCT process is inadequate for obtaining quantitative data. However, a few qualitative observations can be made from the X-ray μCT images. One conclusion that can be drawn from the radiographs is that the cross-sectional area of the metal foam ligaments, or struts, is triangular for these high-porosity metal foams. These cross-sections can be seen in Figure 1.6, for a 5 PPI metal foam sample.

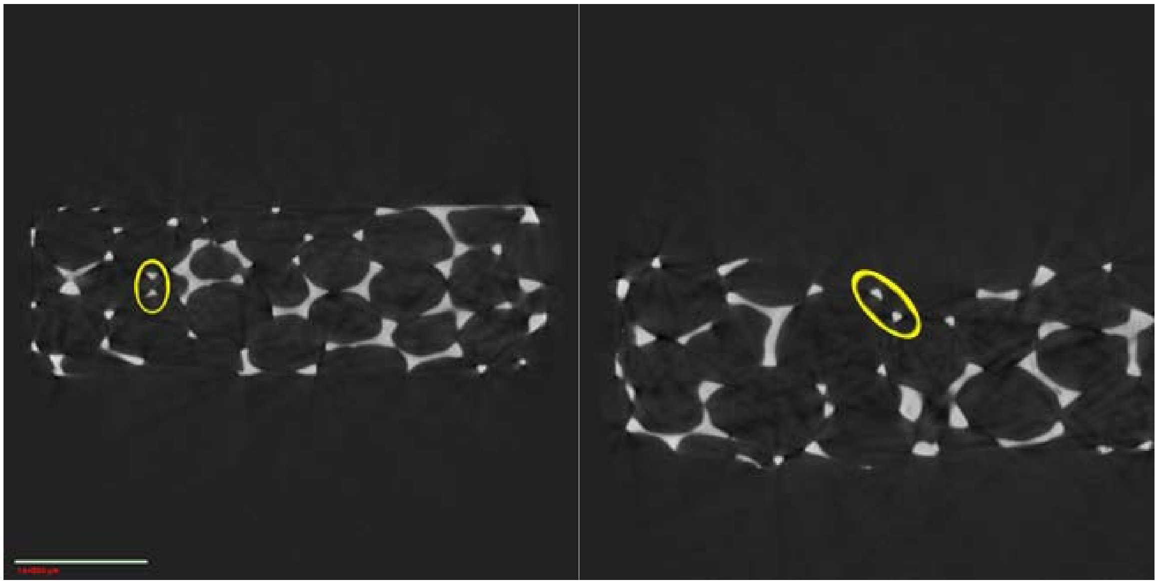

Figure 1.6: Radiographs with triangular cross-sections circled, 5 PPI

Because open-celled metal foams are a promising material for many new uses, a number of recent publications can be found attempting to model the foam for various purposes. Modeling the thermal conductivity, for example, requires some knowledge about the geometry of the foam. In many of these emerging models the ligaments are assumed to have circular cross-sections. One technique for improving these models would be to adjust the model to account for triangular ligaments, rather than cylindrical.

Additional information can be gained from the radiographs without specialized image analysis software. When describing the metal foam structure, it may be beneficial to know the average number of ligaments that intersect a given area. Using the appropriate scale on the radiograph images, the number of ligaments intersecting the viewing plane can be accounted for. In order to aid in the analysis, Microsoft Paint ® was used to segregate the image into sections of known cross-sectional area. The struts within each section were then counted, as shown in Figure 1.7.

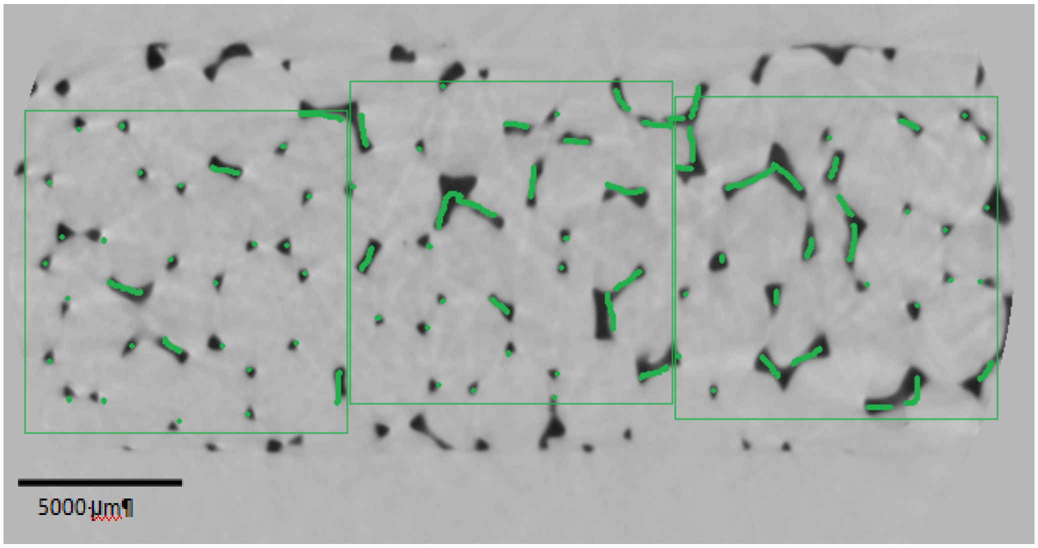

Figure 1.7: Determining strut density from radiographs, 10 PPI

More than ten data sets were analyzed to find an average value representative of the foam sample. The results are provided in Table 1.1.

Table 1.1: Average strut density determined from X-ray µCT data

Foam PPI	Strut Density [struts/m^2]	Standard Deviation
5	92000	14400
10	221000	17800
20	305000	30700

An average hydraulic diameter could also be determined from the radiographs. Some judgment was required when determining the representative strut diameters. In order to obtain accurate values, measurements should be restricted to only the struts that perpendicularly intersected the viewing plane. These struts should appear on the radiographs as triangles that are neither elongated nor connected to additional lengths of foam. Hydraulic diameters were determined by counting the pixels in a strut cross-section. An example radiograph of 10 PPI metal foam, from which hydraulic diameters were recorded, is shown in Figure 1.8. Analyzing multiple images for each of the foam PPI values, more than 150 measurements were averaged to obtain a representative strut diameter. The averaged results are shown in Figure 1.9.

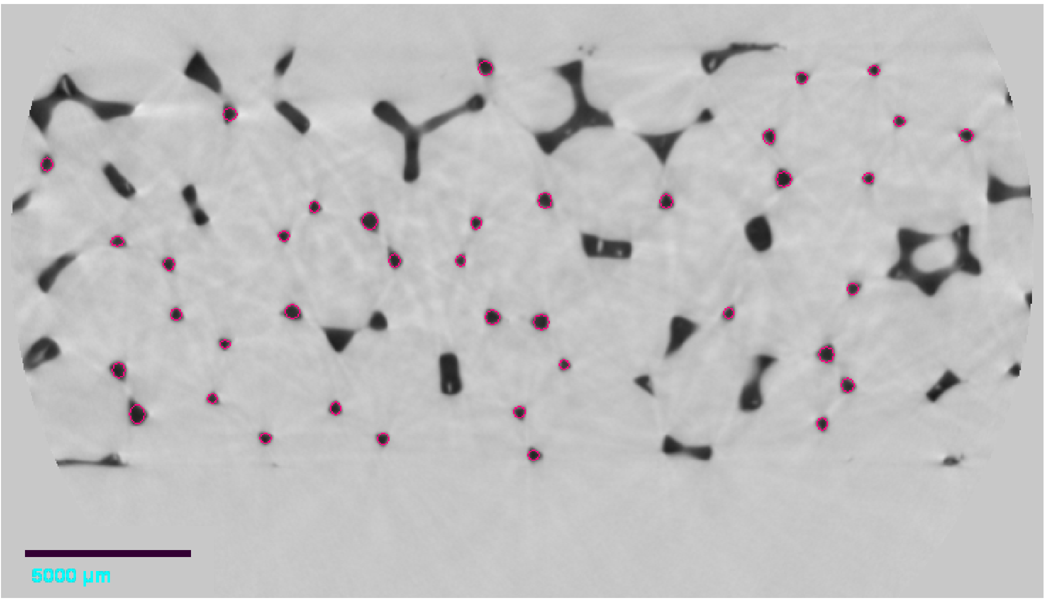

Figure 1.8: Determining strut diameter from radiographs, 10 PPI

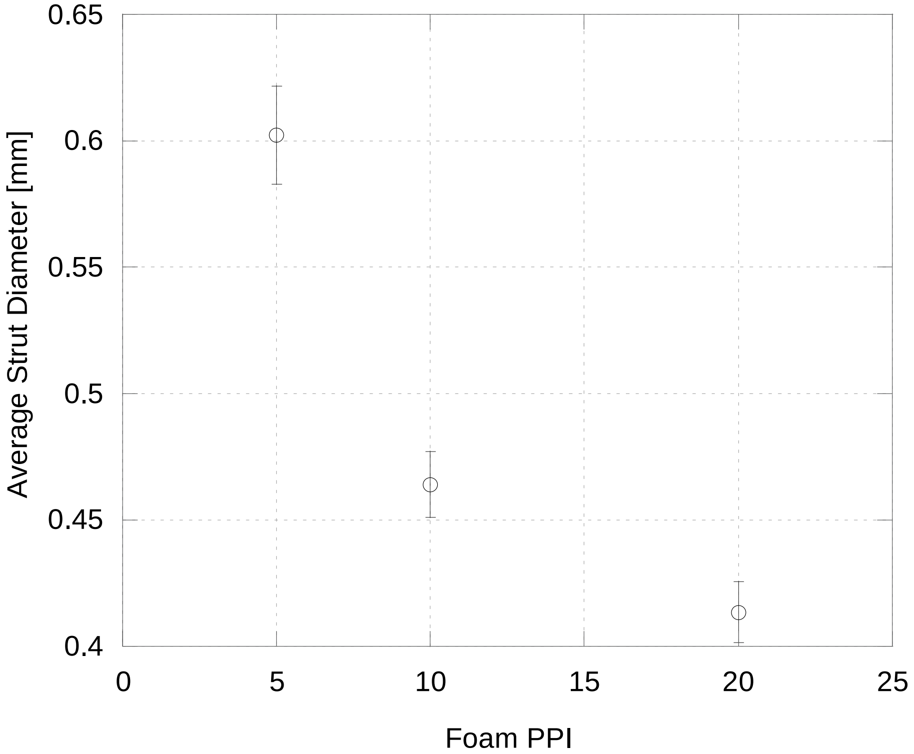

Figure 1.9: Strut diameter determined from X-ray µCT vs. foam PPI

The figure shows strut diameter decreasing with increasing PPI. Thus, as the pore diameter decreases, so does the strut diameter. The average diameters obtained from the radiography analysis are compared to the diameter values provided by the manufacturer in Table 1.2.

Table 1.2: Average strut diameters determined from X-ray μCT data compared to data provided by the manufacturer

Foam PPI	X-ray Data [mm]	Mfg Data [mm]
5	0.6023	-----
10	0.4641	0.3937
20	0.4169	0.2134

Disregarding the 5 PPI foam, as the manufacturer provided no corresponding data for the diameter, it is clear that there is a significant difference between the manufacturer-reported diameter and measured diameter. For these samples, the measured diameter was taken as the more accurate value, as it was experimentally obtained rather than taken from a generalized curve.

After analyzing the raw X-ray images for strut density, diameter, and cross-sectional geometry, advanced image analysis software was required in order to extract additional geometric information. Commercially available software packages, like Amira®, are commonly used for CT analysis. However, due to the structure of the metal foams, the pre-packaged software was insufficient for the required analysis. Amira® could be used for manipulating the images to create visual aids, but the software had difficulty differentiating the pores. In the literature, at least two names of software specializing in foam image analysis were mentioned. Ozella3D was considered proprietary and unavailable to the public [50]. FoamView©, however, was provided as supplementary material online with the citing article [48].

FoamView© requires the input of a series of X-ray CT images. After uploading these images, an appropriate scale, and defining if the foam is black or white in the images, the software creates a 3D rendering. This initial rendering is a volume file, which requires a large amount of computing power.

From the 3D volume, a surface can be created and smoothed using a surface creation tool. Manipulating the surface file requires less computing power, so the volume file is usually set aside once the surface has been created. A sample surface rendering is shown in Figure 1.10 for foam with 10 PPI, where a fog effect has been applied to show depth.

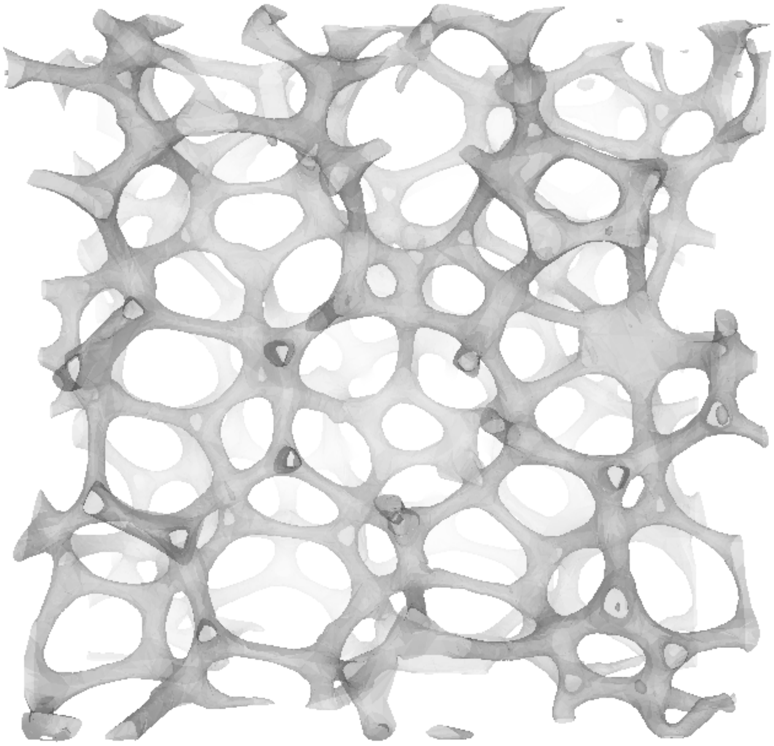

Figure 1.10: Foamview surface rendering, 10 PPI

From the surface rendering, the FoamView© software can create a crude stick figure of the foam structure. The stick figure consists of lines and dots, representing the struts and vertices, respectively. Modification of the stick figure to correspond to the surface rendering is achieved using the built-in functions of the software. An image of the completed stick figure for a 10 PPI metal foam sample is shown in Figure 1.11.

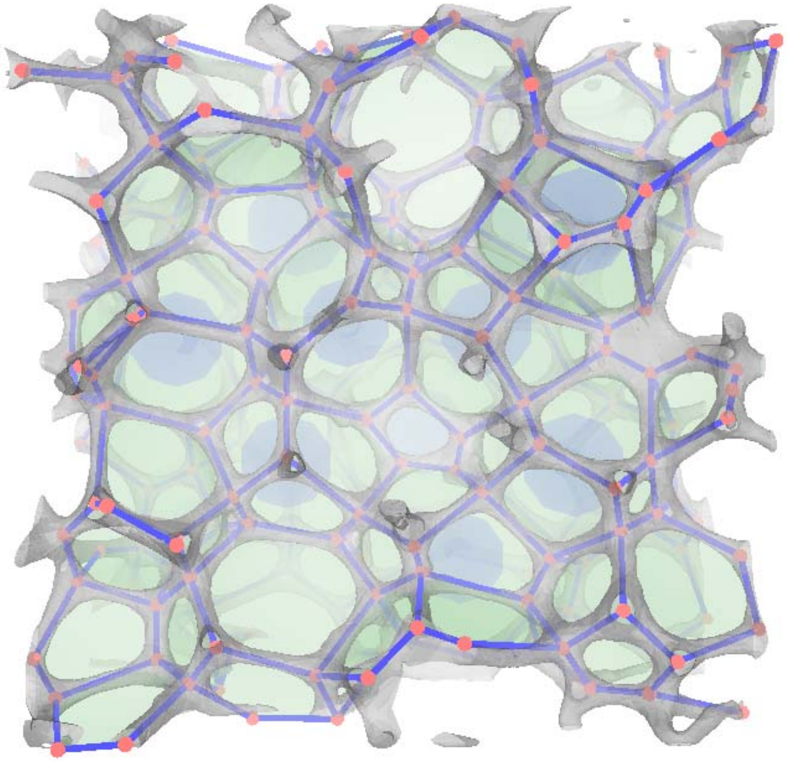

Figure 1.11: Foamview completed stick figure, 10 PPI

The completed stick figure can be viewed alone for quicker response time and a simplified view of the foam structure. During stick figure modification the software recognizes when windows are formed and pores and completed. Windows are automatically shaded green, and blue spheres appear to signify enclosed pores. FoamView© keeps a running total of the number of struts, vertices, windows, and pores recognized in the stick figure. A screenshot of a completed stick figure for 10 PPI metal foam and the FoamView© interface are shown in Figure 1.12.

FoamView generates a report of measurements and statitistics from the completed stick figure. The report includes information about the average strut length and orientation, window shapes, pore (cell) sizes, and interior angles. Additional information such as surface area and volume can be obtained from the surface and volume renderings; however, these values have not been verified. The data can be exported as a Microsoft Excel Worksheet, or viewed in FoamView© as histograms and tabulated values.

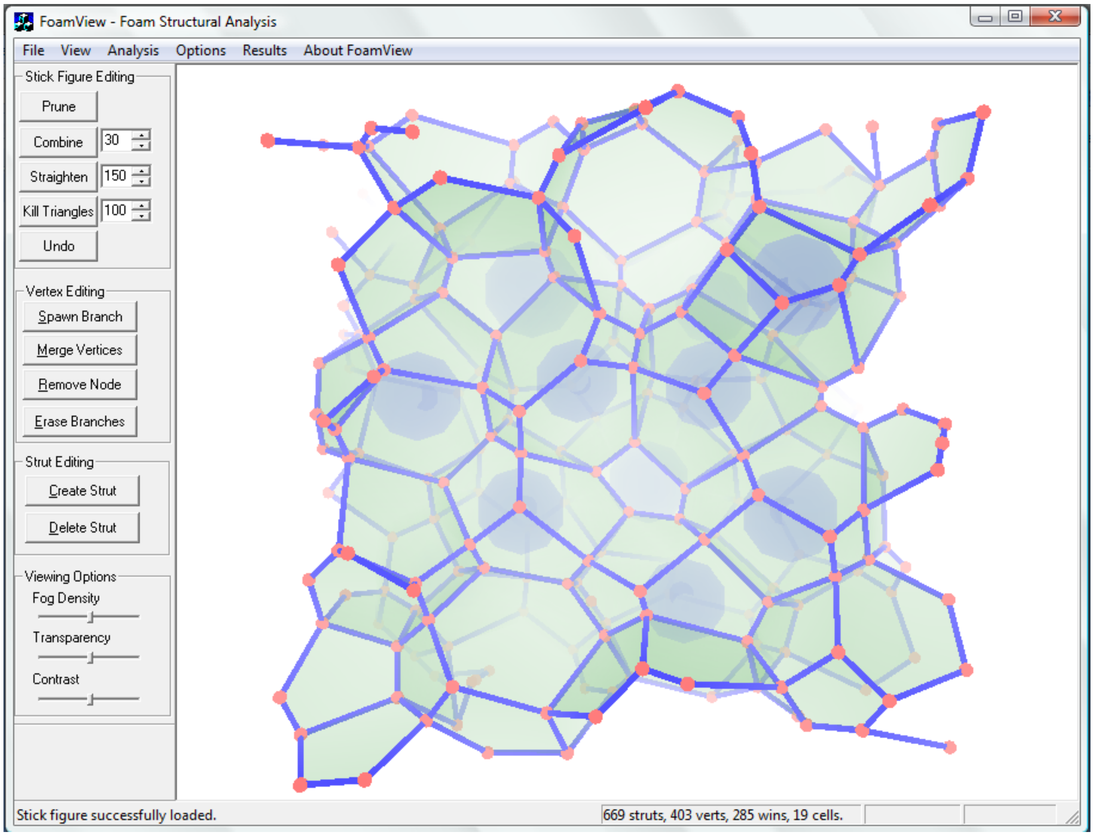

Combine 30

Straighten 150

Kill Triangles 100

Stick figure successfully loaded.

669 struts, 403 verts, 285 wins, 19 cells.

Figure 1.12: Foamview interface showing completed stick figure, 10ppi

The image analysis was conducted for four metal foam samples. Two samples of 20 PPI metal foams were chosen to investigate the repeatability between samples. Some variation was expected considering that the two samples did not have identical void fractions. Two data were analyzed with FoamView© for a 5 PPI sample to investigate the repeatability within a single piece of foam. The results showed good repeatability between samples for 20 PPI foams and data for the 5 PPI foam sample. The results for strut length and orientation of 5, 10, and 20 PPI metal foams, where the 5 PPI and 20 PPI data are averaged values from the two stick figures, are summarized in Table 1.3.

It is clear from the values shown in the table that there is considerable variation in the strut length, which leads to a large standard deviation. This variation may be related to the foam manufacturing process. If the metal foam is created from a gasified liquid metal, then the structure does not reach equilibrium before solidification [48]. The strut length distributions for the different foam samples are shown in Figure 1.13.

Table 1.3: Summary of strut geometry from X-ray μCT data

Foam	average orientation vectors			azimuthal angle	length	standard deviation
PPI	x	y	z	[°]	[m]	[m]
5	0.683	0.508	0.525	58.33	0.00192	0.00069
10	0.554	0.514	0.655	49.08	0.00149	0.00052
20	0.533	0.643	0.552	56.54	0.00112	0.00042

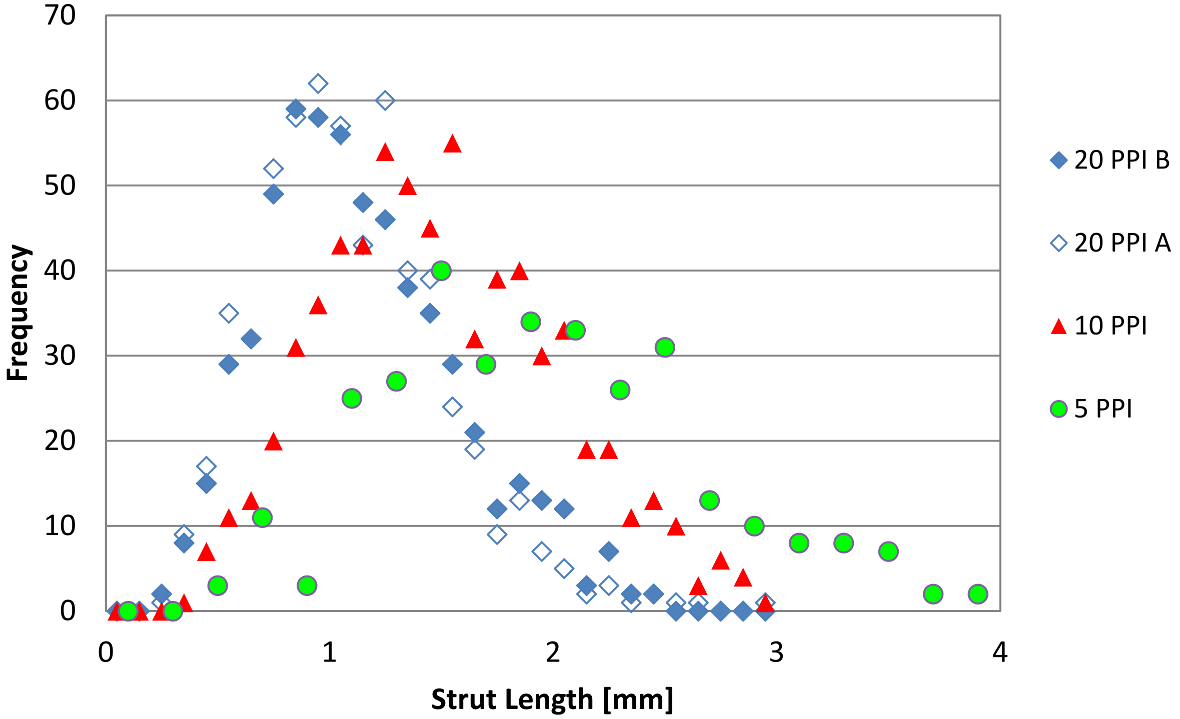

Figure 1.13: Strut length distribution

The data reflect variation in strut lengths for a given sample of foam and that the average strut length becomes gradually larger as PPI decreases, which can be expected. When compared to the strut length distribution in an ideal unit cell, the results differ significantly. The Kelvin unit cell has only one strut length, as all windows consist of regular polygons. The Weaire-Phelan unit cell is comprised of four different strut lengths, which is still far from the foam geometry found here, but it is a better representation of the metal foam than is the Kelvin unit cell.

The window shape distributions for the different foam samples are given in Figure 1.14 and are compared to unit-cell models in Table 1.4. The predominance of pentagons supports the adoption of the Weaire-Phelan unit cell; however, the presence of quadrilaterals suggests that there may be room for improvement. Although the Kelvin unit cell does contain quadrilaterals, it omits pentagons, which are the most frequently occurring shape in real foams. Thus, the choice of the Weaire-Phelan unit cell is further supported.

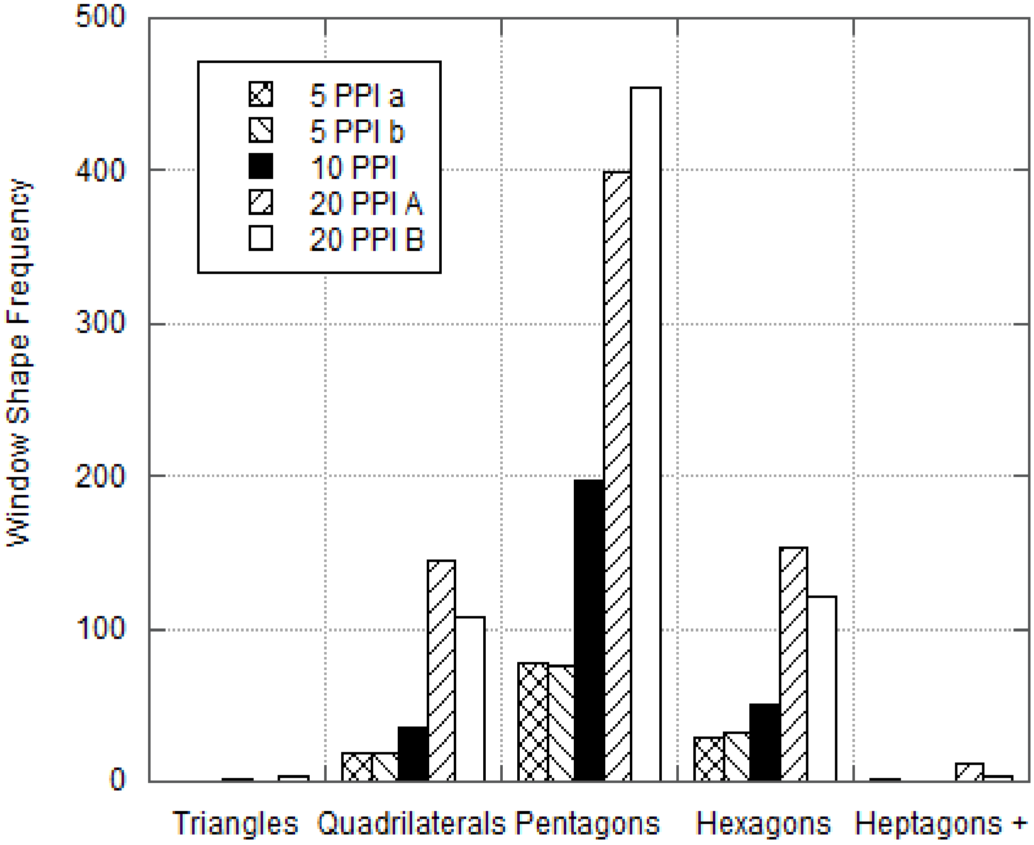

Figure 1.14: Normalized window shape distribution

Table 1.4: Window shape distribution (as a percentage of total) from X-ray μCT data compared to ideal unit cells

FOAM SAMPLE	Triangles	Quadrilaterals	Pentagons	Hexagons	Heptagons+
5 PPI A	0.0	15.1	61.1	22.2	1.6
5 PPI B	0.0	15.1	61.1	22.2	1.6
10 PPI	0.4	12.6	69.1	17.9	0.0
20 PPI A	0.0	20.4	56.5	21.6	1.5
20 PPI B	0.4	15.6	65.9	17.7	0.4
Kelvin	0.0	42.9	0.0	57.1	0.0
Weaire-Phelan	0.0	0.0	88.7	11.3	0.0

1.2.4 Discussion and conclusions of geometric study

X-ray μCT imaging is an effective and convenient means for obtaining a digitized rendering of the real metal foam structures. The X-ray images and specialized image analysis software allowed for the extraction geometric data and characterization of the real foam structure. Four aluminum foam samples were analyzed: one 5 PPI sample, one 10 PPI sample, and two 20 PPI samples. The two 20 PPI samples were chosen to investigate geometric differences between two samples of the same foam PPI, from the same manufacturer.

The image analysis revealed a large variation in strut size, which highlighted the irregularity of the metal foam structure. Standard deviations for the strut length were on the order of 40% of the average value. Values for interior strut angles and average number of windows on a given pore matched those provided in the literature per mathematical requirements. The distributions of the window shapes were compared to the ideal unit cells as a means of determining the most accurate model. The Weaire-Phelan unit cell was proven to be more accurate due to the dominate presence of pentagonal windows, which are not included in the Kelvin unit cell. However, the presence of quadrilateral windows suggests that improvements on the Weaire-Phelan unit cell may exist, with respect to modeling metal foams.

In conclusion, the real structure of open-celled metal foams is highly irregular. This irregularity can be attributed to the non-equilibrium production process and is an inherent characteristic of metal foams. In attempts to model the behavior and characteristics of metal foams, many researchers assume an idealized geometry. Current and future models could be improved by recognizing that the cross-sectional area of the struts is triangular, rather than circular. Improvements can also be made by replacing the ideal Kelvin unit cell model with the more complicated Weaire-Phelan unit cell. While the Weaire-Phelan unit cell is currently more accurate in describing actual metal foams, there is still room for improvement. As new unit cells are proposed, such as the p42a unit cell [35], the Weaire-Phelan model may be replaced with an ideal geometry that more closely matches the actual geometry of metal foams.

1.3 Dynamic dip testing of open-cell metal foams

Because the experimental methods associated with dynamic dip testing (developed with prior ARTI funding) have been explained in detail elsewhere [14], the methods will not be described in detail. The essence of the experiment is to submerge a specimen in water and then suddenly lower the water level until the specimen is suspended above the water, recording the weight of the specimen as a function of time as the water drains from it.

1.3.1 Sample characteristics

All five of the foam samples used in the experiments for the dynamic dip testing, were 75 mm long (gravitational direction), 25.4 mm wide and 13 mm thick. Estimated geometric data for the specimens are provided in Table 1.5, where the average strut diameter, d_f, pore diameter, d_P, and porosity are provided. The foam samples where fixed between flat faux tubes, with the longest dimension aligned with gravity for the dynamic dip tests. A sixth sample, that of a louvered fin, was included for comparison, its geometry is described in Table 1.6 and Figure 1.15.

Table 1.5: Characteristics of metal foam samples

Sample #	Porosity	PPI	d_f (mm)	d_P (mm)
1	0.953	5	0.50	4.02
2	0.942	10	0.40	3.13
3	0.933	20	0.30	2.70
4	0.927	40	0.25	2.02
5	0.913	45	0.20	2.00

Table 1.6: Geometric characteristics of the louver-fin sample

L_p (mm)	F_p (mm)	F_l (mm)	L_l (mm)	α （deg）	F_d (mm)	T_p (mm)	δ_f (mm)	N_{LB} (-)
1.14	1.4	12.43	11.15	29	25.4	14.26	0.114	2

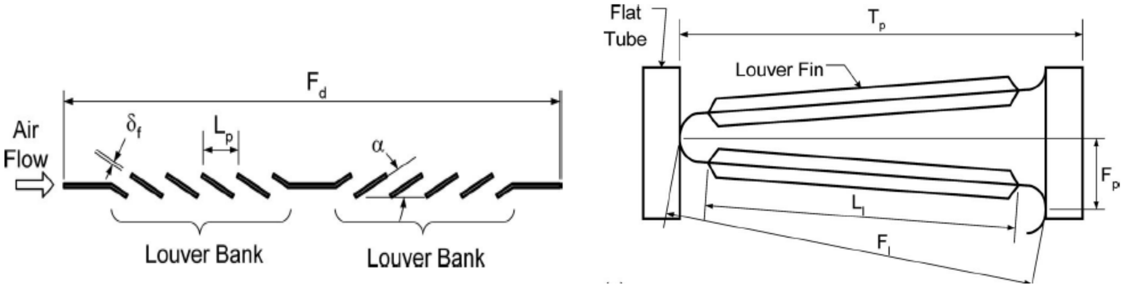

Figure 1.15: Geometric characteristics of the louver-fin sample

1.3.2 Results of dynamic dip tests

The results for the water retention behavior are described below for the samples described above. All of the samples were completely submerged in water. Before starting the test, the samples were checked to make certain that no air bubbles were trapped inside, ensuring that water was completely touching the whole surface of the sample.

1.3.2.1 Effect of porosity. Porosity is an important factor in characterizing the metal foams, though there are other criteria available for distinguishing different types. Generally metal foams are produced in 5, 10, 20 and 40 PPI sizes (where PPI is the pores per inch). This characterization is an approximation made by counting the pores in one inch along one dimension so foam characterized by 5PPI will have 5 pores in a length of 1 inch.

The water retention in grams per unit volume for samples with five different porosities is presented in Figure 1.16. Experiments on all the samples were conducted under same conditions and equal time was given to analyze the steady state behavior for the water retained in the sample. It can be observed from the curves that porosity has a high impact on the water retention, as a 45 PPI sample with smaller sized pores retains much more water than does the 10 PPI sample. In order to provide further perspective, images of samples are provided in Figure 1.17.

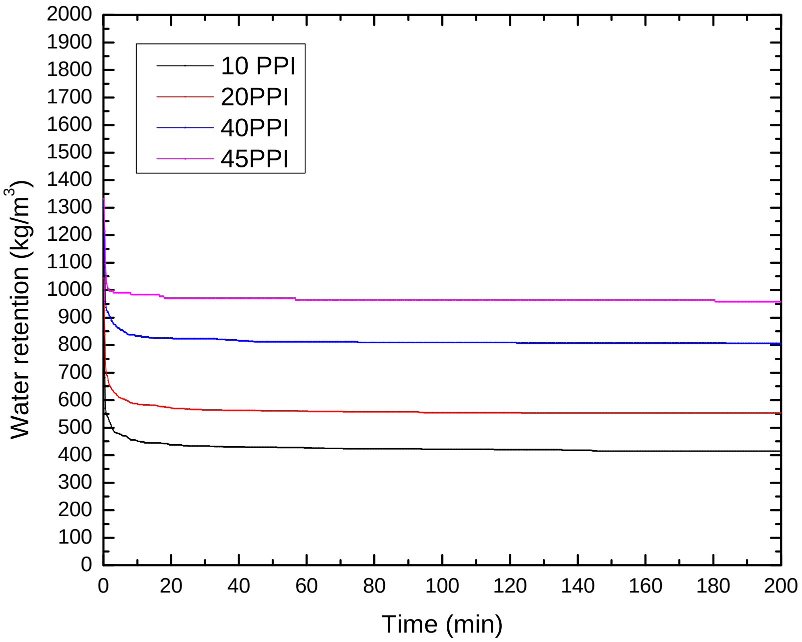

Figure 1.16: Water retention for metal samples with different porosities

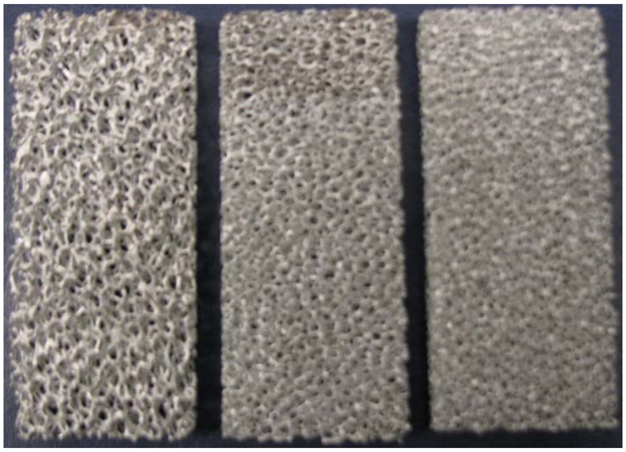

Figure 1.17: Metal foam samples with different porosities (10, 20 and 40PPI)

1.3.2.2 Effect of treatment (Beohmite process). Surface treatments are sometimes conducted to improve the water drainage performance of compact heat exchangers. Work was undertaken to explore whether such treatments might be effective in promoting drainage from a metal foam sample. Samples were cleaned using acetone, but there was not much improvement in the drainage behavior. Then a Beohmite process was implemented in which the samples were washed in boiling soapy water for about 5 minutes. After this treatment the sample surface was altered, as can be seen in Figure 1.18. In order to quantify the effect of this treatment on water drainage, the dynamic dip test was carried out on treated samples. The results for the 10 PPI sample before and after treatment are compared in Figure 1.19. Surprisingly, the Beohmite process, which typically promotes drainage, had an adverse effect on the drainage behavior; the treated sample held about 20% more water compared to an untreated sample.

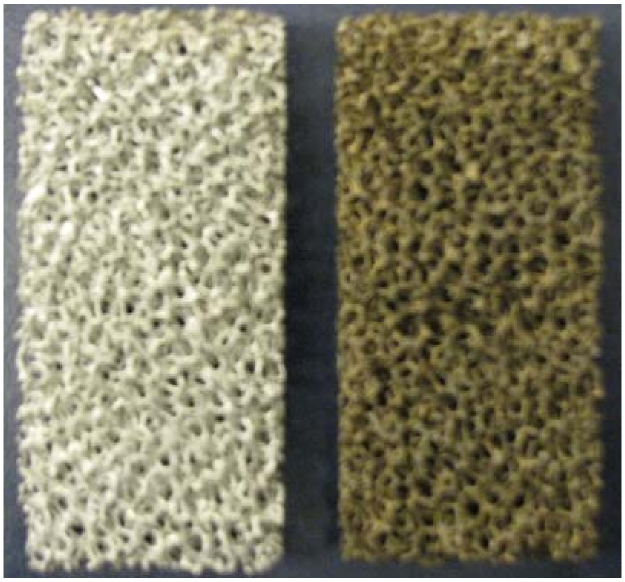

Figure 1.18: 10 PPI Metal foam sample before and after treatment

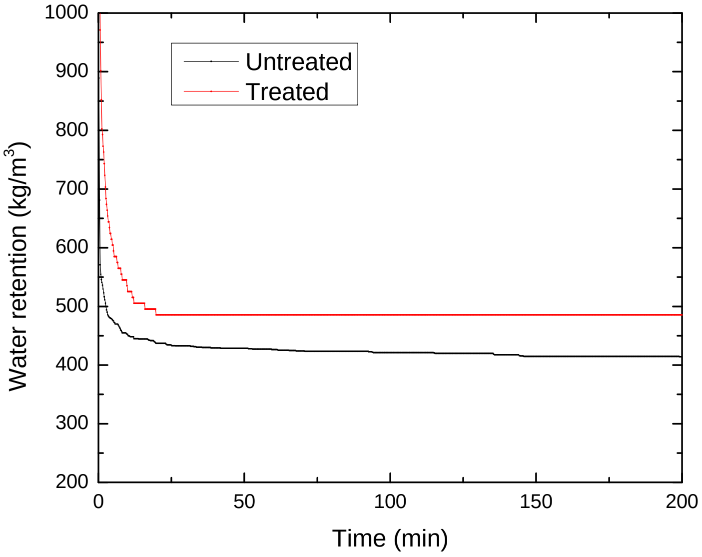

Figure 1.19: Water retention for treated and untreated samples

The surface roughness is increased due to the treatment. This causes the contact line length to increase and more water is retained by the treated samples. Another possible explanation for the treated samples holding more water is the formation of oxide layer on the surface, which makes it more hydrophilic. SEM images of treated and untreated samples are compared in Figure 1.20.

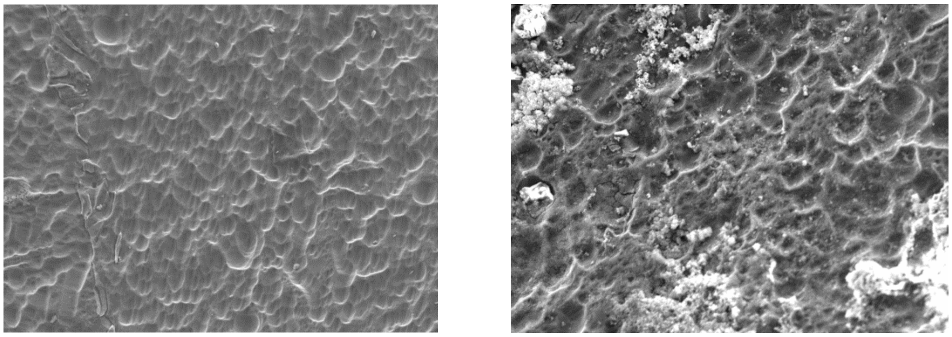

(a) (b)

Figure 1.20: SEM images of metal foam surface: (a) untreated, and (b) treated

1.3.2.3 Effect of combining samples with different porosities. During the experiments an interesting phenomenon was noted and explored, involving the effect of porosity when foams with different porosities are assembled in a single sample. Experiments were conducted on such samples, with five layers of foam with different porosities. Five samples had five layers of foam with porosities 5 PPI, 10 PPI, 20 PPI, 40 PPI and 45 PPI. A sixth sample had 5 layers of foam sandwiched together with foam layers having porosities 10-20-40-20-10 PPI. Hence the total volume of all samples was the same. The 5 layers for each sample were joined using aluminum wires to hold the samples together. The results for the dynamic dip test experiments are shown in Figure 1.21. As expected, the 40 PPI sample held more water than the 10 PPI sample, but strange behavior was shown by the sample having 5 layers of three different types of foam joined in the sequence described above. The amount of water retained was nearly the same as that of the 10 PPI sample after achieving the steady state. This effect suggests that combinations of foam could be used in designs where heat transfer, pressure drop, and condensate retention effects are all important. Such an approach might resolve the critical issue of water drainage while maintaining the same heat transfer performance.

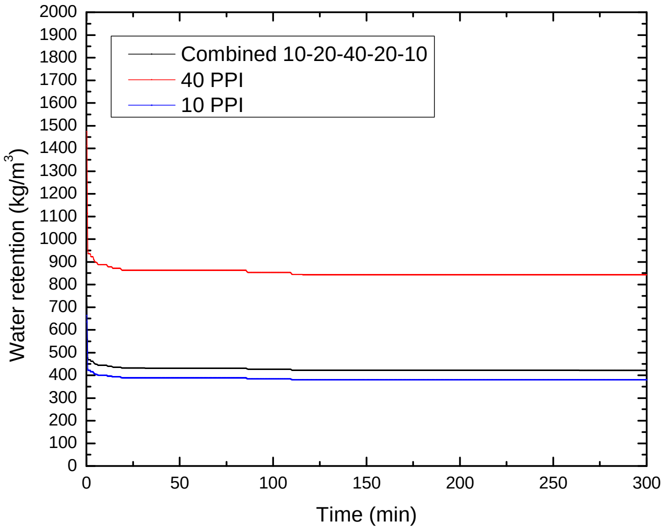

Figure 1.21: Water retention for combined samples

<u>1.3.2.4 Effect of geometrical orientation.</u> The orientation of the sample can affect the water retention of samples. Two different orientations are presented in Figure. 1.22. To explore this effect, experiments were conducted with copper samples. When the same samples were tested with different orientation, the vertical orientation held less water compared to horizontal orientation (Figure 1.23). The relative difference between vertical and horizontal orientation did not change much when foams with different porosities were tested.

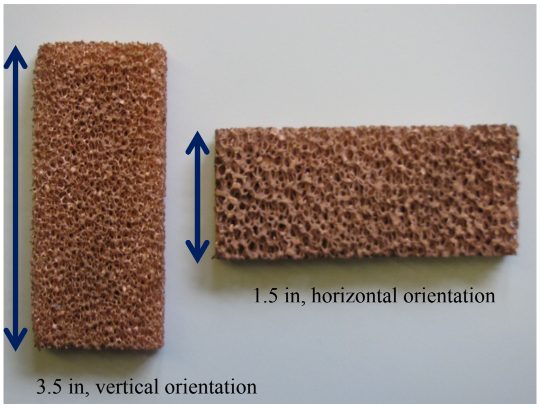

Figure 1.22: Horizontal *vs.* vertical orientation

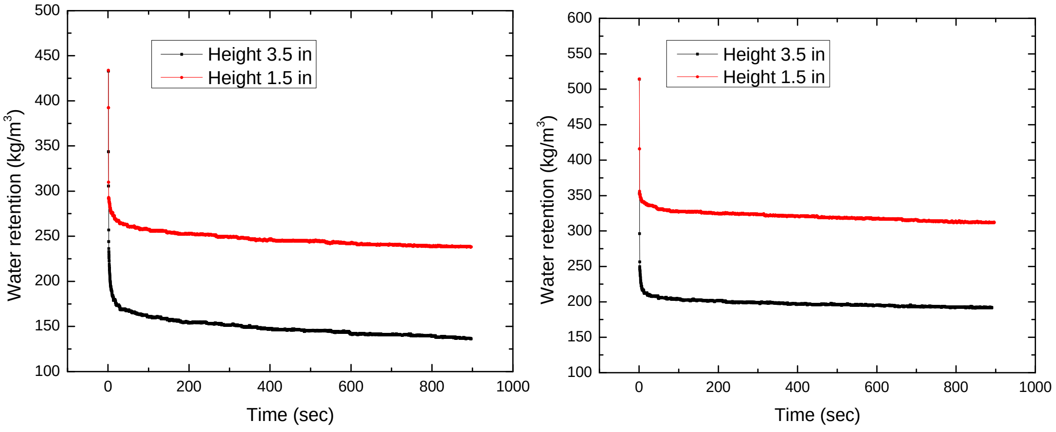

(a)

(b)

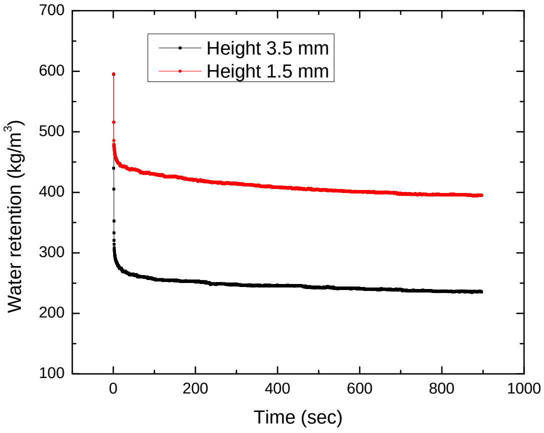

(c)

Figure 1.23: Water retention of copper foams with different orientations (a) 10 PPI (b) 20 PPI (c) 40 PPI

1.3.2.5 A comparison to a louvered fin. Louver fins are extensively used in compact heat exchanger designs. We selected a state-of-the art louvered fin design to compare the drainage behavior of metal foam to a louvered-fin design. Dynamic dips tests were conducted in order to make the comparison. The overall dimensions of the samples were similar and the test conditions for both were identical and these experiments were conducted without any side plates, simply as a screening experiment. The results are provided in Figure 1.24 and the specimens are shown in Figure 1.25.

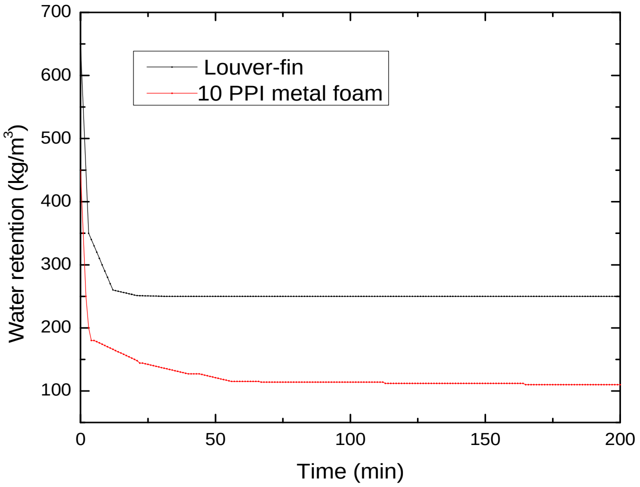

Figure 1.24: Water retention for 10PPI metal foam and the louvered fin (without side plates)

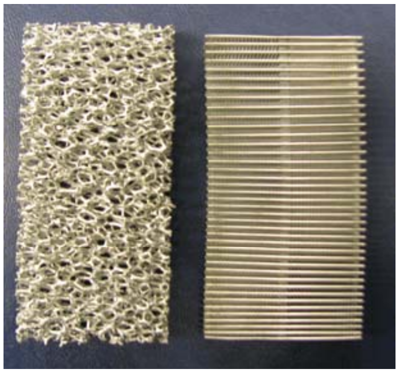

Figure 1.25: Metal foam and louvered fin samples used in the comparative dynamic dip tests

The dynamic dip test results show very large improvements in drainage for the metal foam sample. The 10 PPI metal foam sample held much less water under both steady and transient conditions as compared to the louvered fin. Based on these data one can anticipate that the metal foam heat exchanger will have a lower increase in pressure drop associated with wet-surface operation, compared to its dry-surface pressure drop, than does a louvered-fin design. 10 PPI foam was selected for comparison as it has a sufficient surface area to volume ratio for compact design, with a relatively low pressure drop compared to larger PPI foams (20 and 40). Certainly, the 5 PPI foam with larger pores compared to 10 PPI would have performed even better.

1.3.4 Conclusion

From general experience with porous media, an engineer might anticipate that metal foams would manifest significant water retention, making them unattractive for operation under wet-surface operating conditions. However, dynamic dip tests conducted to quantify the water drainage behavior convincingly demonstrate that metal foams can drain water much more effectively than louvered fins. Water retention depends on factors such as the porosity and surface treatment. When foams of differing PPI are combined into a composite structure, their water retention characteristics can be altered. The composite foam exhibits a drainage behavior like that of the best-draining foam in the composite.

1.4 References

[1] Katz, D.L., and Geist, J.M. "Condensation of six finned tubes in a vertical row," *ASME Transactions,* pp. 908–914, 1948.

[2] Karkhu, V.A., and Borovkov, V.P. "Film condensation of vapor at finely-finned horizontal tubes," *Heat Transfer-Soviet Research,* Vol. 3, pp. 183–191, 1971.

[3] Rifert, V.G., Barabash, P.A., Golubev, A.B, Leot'yev, G.G., and Chaplinskey, S.I. "Investigation of film condensation enhanced by surface forces," *Heat Transfer-Soviet Research,* Vol. 9, pp. 23–27, 1977.

[4] Honda, H., Nozu, S., and Mitsumori, K. "Augmentation of condensation on horizontal finned tubes by attaching a porous drainage plate," *Proceedings of ASME-JSME Joint Thermal Engineering Conference*, Honolulu, Hawaii, pp. 20–24, March 1983.

[5] Rudy, T.M., and Webb, R.L. "An analytical model to predict condensate retention on horizontal integral-fin tubes," *Journal of Heat Transfer,* Vol. 107, pp. 361–368, 1985.

[6] Osada, H., Aoki, H., Ohara,T., and Kuroyanagi,I. "Experimental analysis for enhancing automotive evaporator fin performance," *Proceedings of the International Conference on Compact Heat Exchangers and Enhancement Technology for the Process Industries*, pp. 439–445, 1999.

[7] Osada, H., Aoki, H., Ohara, T., and Kuroyanagi, I. "Research on corrugated multi-louvered fins under dehumidification," Heat *Transfer-Asian Research,* Vol. 30, pp. 383–393, 2001.

[8] McLaughlin, W.J., and Webb, R.L. "Condensate drainage and retention in louver fin automotive evaporators," *Proceedings of the SAE International Congress*, Detroit, MI, Paper No. 2000-01-0575, March 2000.

[9] McLaughlin, W.J. "The effect of condensate on the air side performance of louver fin automotive evaporators," *MS thesis*, Department of Mechanical Engineering, Pennsylvania State University, 1999.

[10] Korte, C., and Jacobi, A.M. "Condensate retention effects on the performance of plain-fin-and-tube heat exchangers: Retention data and modeling," *Journal of Heat Transfer,* Vol.123, pp. 926–936, 2001.

[11] Bull, B.R., and Jacobi, A.M. "A study of the application of vortex generators to enhance the air-side performance of heat exchangers," *Technical Report TR-214*, Air Conditioning and Refrigeration Center, University of Illinois at Urbana-Champaign, 2003.

[12] Kim, G.J., and Jacobi, A.M. "Condensate accumulation effects on the air-side thermal performance of slit-fin surfaces," *Contract Report CR-26*, Air Conditioning and Refrigeration Center, University of Illinois at Urbana-Champaign, 2000.

[13] ASHRAE Handbook-*Fundamentals*, American Society of Heating, Refrigerating and Air-Conditioning Engineers, Inc., Atlanta, GA, 2001.

[14] Zhong, Y., Joardar, A., Gu, Z., Park, Y., and Jacobi, A.M. , "Dynamic Dip Testing as a Method to Assess the Condensate Drainage Behavior from the Air-side Surface of Compact Heat Exchangers," *Experimental Thermal and Fluid Science*, Vol. 29, pp. 957-970, 2005.

[15] ElSherbini, A., and Jacobi, A.M. "A model for condensate retention on plain-fin heat exchangers," *Journal of Heat Transfer,* Vol. 128, pp. 427-433, 2006.

[16] Liu, L., and Jacobi, A.M. "Issues Affecting the Reliability of Dynamic Dip Testing as a Method to Assess the Condensate Drainage Behavior from the Air-side Surface of Dehumidifying Heat Exchangers," *Experimental thermal and Fluid Science,* Vol. 32, pp. 1512-1522, 2008.

[17] Ghosh, I. "How good is open-cell metal foam as heat transfer surface?," *Journal of Heat Transfer,* Vol. 131, pp.1-8, 2009.

[18] Dai, Z., Nawaz, K., Park, Y. G., Bock, J., and Jacobi, A.M. "Correcting and extending the Boomsma-Poulikakos effective thermal conductivity model for three-dimensional, fluid-saturated metal foams." *International Communications in Heat and Mass Transfer,* Vol. 37, pp. 575-580, 2010.

[19] Bhattacharya, A., Calmidi, V. V., and Mahajan, R. L. "Thermo-physical properties of high porosity metal foams." *International Journal of Heat and Mass Transfer,* Vol.45 pp. 1017-1031, 2002.

[20] Mahjoob, S., and Vafai, K. "A synthesis of fluid and thermal transport models for metal foam heat exchangers," *International Journal of Heat and Mass Transfer,* Vol. 51, pp. 3701-3711, 2008.

[21] Ghosh, I. "Deterioration in heat transfer due to axial conduction of heat in open cell metal foam," *Porous Media and its Applications in Science, Engineering, and Industry: 3rd International Conference,* Paper No. 1254, pp. 254-259, 2010.

[22] Thomson, W. "On the division of space with minimum partitioned area," *Acta Mathematica,* Vol. 11, pp. 121-134, 1887.

[23] Rivier, N. "Seifenblasenrhetorik, or the Sound of the Last Trumpet?" *Forma,* Vol. 11, pp. 195-198, 1996.

[24] Almgren, F., and Taylor, J.E. "Soap Bubble Clusters," *Scientific American*, pp. 82-93, 1976.

[25] Weaire, D., and Phelan, R. "A counter-example to Kelvin's conjecture on minimal surfaces," *Philosophical Magazine Letters,* 1994.

[26] Weaire, D. and Phelan, R. "The structure of monodisperse foam," *Philosophical Magazine Letters*, 1994.

[27] Rivier, N., and Aste, T. "Organized Packing," *Forma,* Vol. 11, pp. 223-231, 1996.

[28] Kusner, R., and Sullivan, J. M. "Comparing the Weaire-Phelan Equal-Volume Foam to Kelvin's Foam," *Forma,* Vol. 11, pp. 233-242, 1996.

[29] Aboav, D. A. Kelvin "'Division of Space', and its Aftermath," *Forma,* Vol. 11, pp. 243-254, 1996.

[30] Kraynik, A. M., and Reinelt, D. A. "Elastic-Plastic Behavior of a Kelvin Foam," *Forma,* Vol. 11, pp. 255-270, 1996.

[31] Coxeter, H. S. M. "Close-Packing and Froth," *Illinois Journal of Math*, Vol. 2, pp. 746-758, 1958.

[32] Phelan, R. "Generalizations of the Kelvin Problem and Other Minimal Problems," *Forma,* Vol. 11, pp. 287-302, 1996.

[33] Honda, H., Morita, T., and Tanabe, A. "Establishment of epidermal cell columns in mammalian skin: Computer simulation," *Journal of Theoretical Biology*, Vol. 81, pp. 745-759, 1979.

[34] Tanemura, M. Kelvin “Polyhedra and Analysis of Crystallization,” *Forma*, Vol. 11, pp. 317-325, 1996.

[35] Gabbrielli, R. “A new counter-example to Kelvin's conjecture on minimal surfaces,” *Philosophical Magazine Letters,* pp. 483-491, 2009.

[36] Sullivan, R. M., Ghosn, L. J., and Lerch, B. A. “A general tetrakaidecahedron model for open-celled foams,” *International Journal of Solids and Structures,* Vol. 45, pp. 1754-1765, 2008.

[37] Ross, S., and Prest, H. F. “On the morphology of bubble clusters and polyhedral foams,” *Colloids and Surfaces,* Vol. 21, pp. 179-192, 1986.

[38] Williams, R. E. “Space-filling polyhedron: Its relation to aggregates of soap bubbles, plant cells, and metal crystallites,” *Science,* Vol. 161, pp. 276-277, 1968.

[39] Saadatfar, M., Barry, J., Weaire, D., and Hutzler, S. “Ordered cylindrical foam structures with internal bubbles,” *Philosophical Magazine Letters,* pp. 661-668, 2008.

[40] Van Der Net, A., Delaney, G. W., Drenckhan, W., Weaire, D., and Hutzler, S. “Crystalline arrangements of microbubbles in monodisperse foams,” *Colloids and Surfaces A: Physicochemical and Engineering Aspects,* Vol. 309, pp. 117-124, 2007.

[41] Kriszt, B., and Faure, K. “Characterization of the cell structure of metallic foams. [Charakterisierung der zellstruktur von metallischen schäumen],” *Praktische Metallographie/Practical Metallography,* Vol. 40, pp. 537-555, 2003.

[42] McDonald, S. A., Mummery, P. M., Johnson, G., and Withers, P. J. “Characterization of the three-dimensional structure of a metallic foam during compressive deformation,” *Journal of Microscopy,* Vol. 223, pp. 150-158, 2006.

[43] Krishnan, S., Murthy, J. Y., and Garimella, S. V. “Direct Simulation of Transport in Open-Cell Metal Foam,” *Journal of Heat Transfer*, Vol. 28, pp. 793-800, 2006.

[44] J.A.F. Plateau “Statique Experimentale et Theorique des Liquides Soumis aux Seules Forces Moleculaires,” Gauthier-Villard, Paris, 1873.

[45] Brakke, K. A. “Minimal surfaces, corners, and wires,” *The Journal of Geometric Analysis,* Vol. 2, pp. 11-36, 1992.

[46] Weaire-Phelan Bubbles. <www.steelpillow.com/polyhedra/wp/wp.htm>.

[47] Schmierer, E. N., Razani, A., Keating, S., and Melton, T. “Characterization of high porosity open-celled metal foam using computed tomography,” *American Society of Mechanical Engineers, Heat Transfer Division, HTD*, Vol. 375, pp. 415-424, 2004.

[48] Montminy, M. D., Tannenbaum, A. R., and MacOsko, C. W. “The 3D structure of real polymer foams,” *Journal of Colloid and Interface Science,* Vol. 280, pp. 202-211, 2004.

[49] Saadatfar, M., Garcia-Moreno, F., Hutzler, S., Sheppard, A. P., Knackstedt, M. A., Banhart “Imaging of metallic foams using X-ray micro-CT,” *Colloids and Surfaces A: Physicochemical and Engineering Aspects,* Vol. 344 pp. 107-112, 2009.

[50] Michaeli, W., Schrickte, L., and Berdel, K., “Structural analysis of polymeric foams,” *Proceedings of the Skyscan User Meeting, pp*. 51-54, 2009.

[51] Lin, C. L., Videla, A. R., Yu, Q., and Miller, J. D. “Characterization and analysis of porous, brittle solid structures by X-ray micro computed tomography,” Journal of Morphology*,* Vol. 62, pp. 86-89, 2010.

[52] Vabre, A., Legoupil, S., Buyens, F., Gal, O., Riva, R., and Gerbaux, O. “Metallic foams characterization with X-ray microtomography using Medipix2 detector,” *Nuclear Instruments and Methods in Physics Research, Section A: Accelerators, Spectrometers, Detectors and Associated Equipment,* Vol. 576, 2007.

[53] Maire, E., Fazekas, A., Salvo, L., Dendievel, R., Youssef, S., and Cloetens, P. “X-ray tomography applied to the characterization of cellular materials. Related finite element modeling problems,” *Composites Science and Technology*, Vol. 63, 2003.

[54] Winter Jr., J. M., Green Jr., R. E., Waters, A. M., and Green, W. H. “X-ray computed tomography of ultralightweight metals,” *Research in Nondestructive Evaluation,* Vol. 11, pp. 199-211, 1999.

[55] Industrial computed tomography systems. <www.xviewct.com>.

[56] Xradia solutions overview. <http://xradia.com/solutions/index.php>.

[57] Bodla, K.K., Murthy, J.Y., and Garimella, S.V. "Microtomography-based simulation of transport through open-cell metal foams," *Numerical Heat Transfer, Part A: Application.* Vol. 58, pp. 527-544, 2010.

[58] <http://en.wikipedia.org/wiki/Truncated_octahedron>.

Chapter 2 — Pressure drop for air flow through open-cell foams

2.1 Introduction

Pressure drop is an important design consideration for many heat exchangers, because the pressure drop at a given volumetric flow rate directly determines the fan power requirement. Generally a design goal is to minimize this power expenditure. Typically, increased compactness (higher heat transfer surface area per unit volume) leads to an increase in pressure drop per unit flow length. Metal foam heat exchangers have very high surface-area-to-volume ratios and are thus anticipated to have relatively large pressure drop per unit length. This expectation is reinforced by the complex geometry of the foams which results in a high degree of boundary layer restarting and wake destruction by mixing. Foams exhibit very high heat transfer coefficients and the heat-momentum analogy also suggests the pressure drop per unit flow length will be large. In this chapter the pressure-drop performance of metal foam heat exchangers is considered. The pressure drop per unit length has been determined experimentally, and results are compared to explore the effect of foam geometry. Based on the experimental results, a model has been developed to predict the pressure drop per unit length based on the pore diameter and flow depth. Although an earlier phase of this project resulted in an extensive literature review, that earlier review has been extended and enhanced. Comparing the extant work to the new experimental results shows deficiencies in our current ability to predict pressure drop for air flows through metal foams. The new model is an attempt to extend that earlier work. The effect of condensation on the pressure drop has also been analyzed. Surprisingly, but as suggested in Chapter 1, metal foam heat exchangers perform well under wet-surface conditions, making them more competitive with other compact designs, such as louvered-fin heat exchangers, for dehumidification applications.

2.1.1 Literature review

Metal foams are a relatively new class of materials with low densities and novel thermal, mechanical, and acoustic properties. They were initially developed in 1960s by the US Navy for cooling interballistic missile components and were maintained under secrecy until the early 1980s when they became commercially available in the US. The recent development of a variety of processes for producing them at lower cost, yet with improved properties, has increased their applications [1]. They have been used in aerospace applications [2, 3], geothermal operations, and petroleum processing [4]. Nickel foams have been used in high-power batteries for portable electronics [3]. Metal foam has been considered for use in fuel cells [5], in many chemical and medical applications [6], and by the electrochemical industry [1]. Aluminum has emerged as the prime material for metal foams due to its low density, high thermal conductivity, and its relatively low price. Thermal management applications of metal foams include compact heat exchangers and compact heat sinks for power electronics [2]. The open porosity, low relative density, and high thermal conductivity of the cell edges, large accessible surface area per unit volume, and the ability to mix the cooling fluid by promoting eddies [7] all make metal foam thermal management devices efficient, compact, and light-weight.

Due to their relatively recent emergence and complex structure, metal foams are still incompletely characterized. Interest in using them in contemporary technologies makes the need for fully characterizing them more urgent. Central to this need is an accurate evaluation of the flow characteristics to assist in making the trade-off analysis between the increased heat transfer and the associated increase in the pressure drop for foam heat exchanger and heat sink designs. Extensive reviews of the topic of fluid flow in porous media in general can be found in [8–11]. The porous matrix of metal foam consists of tortuous irregularly shaped flow passages with a continuous disruption of hydrodynamic and thermal boundary layers. The flow recirculates at the back of the solid fibers, and turbulence and unsteady flows often occur [12]. Geometric complexity prevents exact solutions of the transport equations inside the pores [7, 13, and 14]. Thus, researchers rely heavily on experimentation and empirical models, and to a lesser degree on analytical models, as described below.

Seguin *et al.* [15] provided experimental characterization of flow regimes in various porous media. The onset of the turbulent flow regime was found to be at a Reynolds number based on the pore diameter of 470; this corresponds to 0.093 using the permeability-based Reynolds number, Re_K. Lage and Antohe [13] revisited the famous report of Darcy and argued that the ratio between the form and the viscous forces should be used to mark the transition from the linear to the quadratic regimes of the pressure drop behavior. They concluded that the transition is material specific and depends on the internal geometry of the porous medium. Decker *et al.* [16] provided detailed experimental characterization and numerical modeling of the heat and mass transport in highly porous nickel-chromium alloy foam. They used an additional pressure drop term in the momentum equation, which depended on the properties of the foam. The fluid flow models for packed beds did not apply to metal foams, but they contained and described all the relevant transport effects [16].

Bastawros [7] and Bastawros *et al.* [12] provided experimental measurements of the thermal and hydraulic performance of metal foams subject to transverse airflow in the transition regime, i.e., Re_K=1.01. They used 30 pores per inch (PPI) open cell aluminum foam with a porosity of 91.5%. The pressure drop followed a power law when plotted against the flow velocity.

Crosnier *et al.* [5] studied 20 and 40 PPI aluminum foam and 20 PPI stainless steel foam using air. All the porosities were above 90%. The transition from the laminar to the turbulent regime took place at a Darcian velocity of about 1 m/ s. They stated that the larger the pore diameter, i.e., the smaller the PPI the higher the permeability K and the smaller the pressure drop. They also reported that the smaller the pore size, the higher the surface area and thus the higher the mechanical energy dissipation. The Darcian permeability, K, scaled well with the square of the pore size, while the non-Darcian permeability called the passability, which is the ratio of the inertia coefficient c to the square root of K, scaled well with the pore size. The permeability and the passability were functions of the porosity, the pore size, the surface area, and the solid structure of the foam. Khayargoli *et al.* [6] studied the relationship between the permeability and the structural parameters for air flow in nickel and nickel-chromium foams. The velocity ranged from 0 to 15 m/s, while the porosity ranged from 83 to 90%. As the pore size decreased, the surface area increased, creating additional flow resistance. Increasing the thickness of the foam in the flow direction did not affect *K*. An increase in the pore diameter resulted in an increase in *K* and a decrease in *c*, but there was no clear correlation with the porosity. They argued that for large-pore foam, *K* was large and the pressure drop was mainly due to form drag. For this case, the pressure drop correlated with the square of the velocity. The two types of foam tested produced different values of *K* and *c*, due to the differences between their structures. They concluded that while the flow in the foam is very complex, *K* and *c* could be predicted by an Ergun-like model using appropriate constants (presented later).

Tadrist *et al.* [17] investigated the use of aluminum foam for compact heat exchangers. The porosities of the foam were over 90%. They experimentally determined *K* and *c* and used an Ergun-type relation between the pressure drop and the velocity in the foam. Kim *et al.* [18] carried out systematic experiments to study the friction and the heat transfer characteristics of porous fins in a plate-fin heat exchanger using water. The foam fins had porosity in the range 89 to 96% and a thickness of 3 cm in the flow direction. Both the friction and the heat transfer were significantly affected by the permeability and the porosity of the foam fin. They determined the permeability using the Forchheimer model (presented later) and correlated the friction factor to the Reynolds number, the Darcy number, and the geometry.

Paek *et al.* [19] experimentally determined the permeability and the inertia coefficient for water flow through aluminum foam in the porosity range of 89 to 96%. At a fixed porosity, as the cell size decreased, the surface area to volume ratio increased, which increased the resistance to the flow and thus lowered the permeability and increased the pressure drop. The friction factor was correlated to Re_K. The inertia coefficient was very sensitive to the roughness of the foam, which depended on the shape of the ligament and the cell structure.

Current models for packed beds are not suitable for high-porosity metal foam [4] due to the different structure of the foam. Bhattacharya *et al.* [20] provided analytical and experimental results for the permeability and the friction coefficient for aluminum foam. They represented the foam by a two-dimensional array of hexagonal cells and proposed models for the inertia coefficient and the friction factor. Experiments covered porosities from 90 to 98% and pore densities of 5, 10, 20, and 40 PPI. *K* increased with the pore diameter and porosity, while the friction factor depended only on the porosity. They used the Forchheimer equation to describe the pressure drop in the foam, which was fully saturated with air or water.

Du Plessis *et al.* [21] provided a geometrical model for the fluid dynamics in metal foams. The model was verified using water and a glycerol solution flow in metallic foams having 45, 60, and 100 PPI, and porosities of 97.8, 97.5, and 97.3%, respectively. Fourie and Du Plessis [22] extended that work by developing expressions for the characteristic dimension as a function of the cell size and the porosity. They applied the new model to the experimental results of Bastawros *et al.* [12]. The characteristic dimension correlated well with the cell size. Despois and Mortensen [23] presented a microstructure-based model for the permeability of porous metal, and used pure aluminum foam saturated with water and glycerin separately, to validate the model. The porosity ranged from 69 to 88%. The Darcy regime data showed a strong dependence of the permeability on the square of the pore size.

Boomsma *et al.* [24] modeled the flow in aluminum foam using a periodic unit of eight cells. The pressure drop predicted by the model was 25% lower than values obtained by experiment. This difference was reduced to 12% after the wall effects were included in the simulation. The wall effects were probably important due to the small size of the foam sample (12 mm by 38 mm by 80 mm long). They found the Reynolds number based on the pore diameter more applicable than the permeability-based Reynolds number for metal foams. The surface area controlled the viscous drag, which was the dominant factor for the pressure drop in the foam.

Prior to the work reported in the current study, few studies [25–28] used three-dimensional x-ray computed tomography to investigate the microstructure of metal foam. Olurin *et al.* [27] indicated that it was unclear how to precisely characterize the microstructure and the internal architecture of the foam, and that there was no simple standard experimental technique for such characterization. Scheffler *et al.* [28] studied some 20 PPI aluminum foam morphology and reported that the pores were nearly spherical. The ligament diameter showed a maximum at 0.25 mm and the cell diameter showed a bimodal distribution with maxima at 0.75 and 1.9 mm cell. Zhou *et al.* [1] investigated the microstructure and macrostructure of aluminum foam using a combination of optical and scanning electron microscopy. They noted that the cells in 10, 20, and

40 PPI foam were elongated, and that the actual structure was somewhat different from the commonly accepted tetrakaidecahedron. They recorded significant variations in both the face size and the ligament length. In addition, there were numerous closed-cell faces observed [20, 24].

Compressing the foam increases the metal density, makes the foam more suitable for brazing, which improves the heat transfer across the solid-foam interface, and improves the structural rigidity. It also substantially increases the surface area density, which enhances the heat transfer in the foam. Compressed foam has received relatively little attention. There are very few data available in the open literature. Researchers [14, 29–31] have studied 40 PPI compressed foam, and compressed 10 PPI foam has been considered [14]. Boomsma *et al.* [29] and Boomsma and Poulikakos [30] measured the hydraulic and thermal performance of open-cell, 40 PPI aluminum foam, compressed and uncompressed, with porosities between 60.8 and 88.2%. They used the Forchheimer equation to fit their experimental pressure drop data. The compressed foam heat exchangers generated thermal resistances that were two to three times lower than the commercially available heat exchangers, while requiring the same pumping power. Decreasing the pore diameter dramatically decreased the permeability and increased the form coefficient. No correlations were provided. Lage *et al.* [13] presented experimental pressure drop data for air flow through compressed 40 PPI metal foams with porosities in the range of 32 to 62%. For Re_K smaller than 10, there was a third regime beyond the Forchheimer region in which the pressure drop correlated with the velocity using a cubic polynomial. Hwang *et al.* [14] studied the friction drag for airflow in compressed aluminum foam initially having 10 PPI and porosities of 70, 80, and 95%. The permeability and the inertia coefficient were determined from the Forchheimer relation. The friction factor was correlated to the Reynolds number using a power law fit. It increased with decreasing the porosity at a fixed Reynolds number. The best thermal performance was for the 80% porous foam for a given pumping power. No correlations were given for the permeability or the inertia coefficient. Antohe *et al.* [31] experimentally determined the permeability and the inertia coefficients for air and poly-alpha-olefin oil flow in compressed 40 PPI aluminum foam in the porosity range of 30 to 70%. The permeability decreased with decreasing porosity. The inertial coefficient did not have a monotonic variation, but manifested a general tendency to increase with decreasing porosity. They used the permeability-based

Reynolds number of one to indicate the transition from the linear to the quadratic regimes of the pressure drop. The discrepancy between the results obtained with air and oil were 18% for the permeability and 51% for the inertia coefficient.

In general metal foam has not been studied to the same extent as that of other types of porous materials. Paek *et al.* [19] observed that the experimental pressure drop data for metal foam in the literature seemed to be at variance with each other. For packed beds, such data are substantially more consistent. While compressed 40 PPI [30, 31] and 10 PPI [14] foam were tested, to the authors' knowledge compressed 20 PPI foam has never been tested; it has different geometrical parameters, which may offer some performance gains over the other pore densities. In addition, there are no correlations for the inertia coefficient or the permeability in the previous studies of compressed foams. The existing analytical models [20–22], on the other hand, all assume uniform cell structure, which is not applicable to the deformed cells of compressed foam.

A range of flow geometry has been considered. For example, Noh *et al.* [33] reported on the pressure loss in an annulus filled with aluminum foam. Cross sectional geometry is probably not very important. However, entrance, exit and flow development effects may be important. In two intriguing studies, Naakteboren *et al.* [34, 35] investigated the entrance/exit effects on the pressure drop analytically and numerically using analogies between flow through slotted plate placed along a flow channel and flow through porous media. They concluded that for a porous medium with length greater than one hundred times the pore size, the core pressure (due to the porous medium) dominated the entrance/exit pressure drop, and the entrance/exit effects became negligible [35].

Medraj *et al.* [36] investigated the effect of microstructure on the permeability and form drag coefficient for two types of nickel foam. A small section of the study was dedicated to the issue of sample thickness. By considering 5-mm-think and 10-mm-thick samples, they found that there was very little effect of the thickness on the permeability. However, when they further varied the thickness by removing 0.5–1.5 mm sections, the effect of thickness on the pressure drop became apparent. No indication of a minimum thickness for which the permeability would be independent of the thickness was given.

Innocentini *et al.* [37] studied the effect of both sample thickness and sample fixture on the pressure drop in nickel–chromium foam. In a plot of pressure drop versus the Darcy velocity for various sample thicknesses, the effect of thickness on the pressure drop was small. However, when the permeability and the form drag coefficient were plotted against the thickness, the effect of the thickness on these flow properties became strongly evident. The permeability increased linearly and did not reach a constant value for the range of thicknesses tested. The values of the permeability and form drag coefficient given in these studies are strictly applicable to the samples that were tested, and are not material properties that can be applied to other thicknesses of the same foam, primarily because they are functions of thickness, as will be discussed later. International, American, and European standards are available for testing rigid and flexible porous materials, such as polymeric materials [39, 40], textile fabrics [41], filtration media [42] and urethane foams [43]. These standards do not specify the size of the test samples for rigid porous media. Similar observations were made by Innocentini *et al.* [37].

In this study, experimental results are presented for air flowing through a spectrum of commercially available aluminum foam compressed and uncompressed, including 20 PPI foam. Based on experiments, a model for predicting the pressure drop in metal foams is developed using easily measurable parameters. The model assumes an Ergun-type dependence of the permeability on the porosity and relies on experiments to determine some parameters. The new experimental data and correlations provide key information needed for computing the pumping power for foam heat exchanger design and optimization. Results are also presented from an extensive, systematic experimental study of the effect of foam thickness on the viscous and form-drag contributions to the pressure drop for air flowing through three types of aluminum foam—the most common metal foams. This work provides a clear indication as to minimum thickness of the foam in the flow direction for the permeability and form drag coefficient to be 'true' material properties independent of thickness. Finally this chapter provides correlations that predict the pressure drop for air flow in metal foams in terms of thickness and velocity.

2.1.2 Flow relations

When the flow through a porous medium is slow enough (creeping flow), the pressure drop is solely due to viscous drag, and the well-known Darcy equation is satisfactory:

$$\frac{\Delta P}{L} = \frac{\mu}{K} V \tag{2.1}$$

where ΔP is the static pressure drop, L is the length (or thickness) of the porous medium in the flow direction, μ is the fluid viscosity and K is the permeability of the porous medium. The superficial velocity V is calculated by dividing the total volumetric flow rate through the porous medium by the total cross-sectional area to the flow. Such creeping flows in porous media do occur in nature; for example, groundwater flows are commonly modeled with success in this way. However, these flows typically require a low velocity and manifest a low pressure gradient and measuring the velocity and pressure gradient can be challenging in the laboratory. If the flow velocity is high, the Darcy equation can no longer describe the pressure drop. Departure from the Darcy regime is typically expected to occur at some particle Reynolds number for the porous medium:

$$\mathrm{Re}_d = \frac{\rho V d_{50}}{\mu} \tag{2.2}$$

where ρ is the fluid density, and d_{50} is the average particle diameter. The Darcy flow regime is expected for $Re_d \leq$ 1-10.

A critical Reynolds number for anticipating departure from the Darcy regime, based on the porosity of the medium, was developed by du Plessis and Woudberg [44]:

$$Re_C = \frac{26.74\varepsilon(1-\varepsilon)^{1/3}}{\left[1-(1-\varepsilon)^{1/3}\right]} \tag{2.3}$$

Using Eq. (2.3) to calculate Re_c for a particular porous medium, it is expected that when $\mathrm{Re}_d > \mathrm{Re}_c$, the flow will not be in the Darcy flow regime. According to du Plessis and Woudberg [44], for porosities in the range of 90-95%, the critical particle Reynolds number is Re_d=15-20. It is smaller for higher porosity. Metal foams have porosities in this range.

Some authors use a Reynolds number based on the square root of permeability in order to demark the limit for Darcy flow:

$$Re_{\sqrt{K}} = \frac{\rho\sqrt{K}V}{\mu} \tag{2.4}$$

When the value of this Reynolds number is around unity, form drag starts to be important, and the energy dissipation is due to viscous and form drag, and the Hazen-Dupuit-Darcy (widely known as the Forchheimer) equation is often used to relate the pressure drop to the superficial velocity in the porous medium:

$$\frac{\Delta P}{L} = \frac{\mu}{K}V + \rho C V^2 \tag{2.5}$$

where C is a form drag coefficient which can be expressed as $c/K^{0.5}$, and c is a dimensionless coefficient. For a discussion regarding the use of c, Lage and Antohe [31] should be consulted. Both K and C are strongly dependent on the structure of the porous medium. Ergun [45] empirically related the permeability and the form drag coefficient to some structural parameters such the particle diameter. In his work [45] the particle diameter was easy to define, due to the uniform porous media studied. However, for the web-like structure of porous metals, the effective particle diameter is not easy to determine. Different researchers have used various structural parameters as the particle diameter. A recent, thorough discussion regarding this issue is provided by Dukhan and Patel [46].

Making scaling arguments, Lage and Antohe [31] proposed a Reynolds number of the following form to determine the limit for the Darcy flow regime:

$$Re_{CK} = \frac{\rho C K V}{\mu} \tag{2.6}$$

However, a problem arises in determining the critical Reynolds number: either K (Eq. 3) or both K and C (Eq. 2.6) must be known *a priori* determine whether the Darcy regime prevails.

Fortunately, these ambiguities do not complicate the data interpretation in the experiments reported in this chapter, because in the experiments to be reported—where appropriate velocities for air-conditioning and refrigeration systems are adopted—the velocity was always sufficiently high to ensure all data were well into the Forchheimer regime. Unfortunately, the behavior is more complex than that obtained in the Darcy flow regime. Pressure drop modeling is thus expected to follow Eq. (2.5).

For gas flow in porous media, the pressure drop can be large enough that compressibility effects become important. In order to account for variations in gas density, the pressure drop in Eq. (2.5) is computed using the following by some authors[1]

$$\Delta p \equiv \frac{p_i^2 - p_o^2}{p_i} \tag{2.7}$$

where p_i and p_o are the inlet and exit pressures. A detailed description of different correlations for hydraulic performance can be found in Appendix C.

2.2 Experimental results

Pressure drop measurements were obtained in a closed-loop wind tunnel, using the apparatus and procedures outlined in Appendix D. The experimental conditions are summarized in the Table 2.1. The dry-surface pressure drop experiments were conducted under adiabatic conditions, and the test conditions for wet- and frosted-surface conditions, along with experimental uncertainties are detailed in Appendix D.

Table 2.1: Test conditions

Test condition	Inlet air temperature (^{0}C)	Air relative humidity (%)
Dry	33±5	60
Wet	33±5	70
Frost	4±2	70

---

[1] Note that in the current work, the conventional approach for heat exchangers is used, $\Delta P = P_i - P_o$.

The results of the experiments conducted to analyze the pressure-drop performance of heat exchangers when metal foams were used as fins are presented in this section. The relative dependence of pressure drop on geometrical parameters, such as pore diameter, hydraulic diameter and flow depth is evaluated. Results for the pressure drop are compared to different porous media to explore how metal foams perform compared to carbon foams and wire mesh.

2.2.1 Pressure drop and porosity of metal foams

2.2.1.1 Dry surface conditions. The results for the pressure drop per unit length are plotted against the face velocity under dry surface conditions in Figure 2.1. As demonstrated by the figure, the pressure drop per unit length increases with an increase in PPI (a decrease in pore size). The 5 PPI foam, with a pore size of about 4 mm, showed the smallest pressure drop for all face velocities, while the 40 PPI foam, with pore size of about 1.8 mm resulted in the highest pressure drop. Another interesting finding is how the pressure gradient depends on pore size. The pore size differed by about 30% between the 5 PPI and 10 PPI foams, and the pressure gradient increased by roughly 15 to 20 percent at high velocities. At velocities below about 3 m/s, the difference was negligible. However when the pore size becomes smaller the pressure gradient showed an obvious difference even for small face velocities, as can be observed in Figure 2.1. While reducing the data for the pressure gradients, the effect of flat tubes between metal foam fins was neglected, their contribution to pressure drop was very small compared to the porous metal foam.

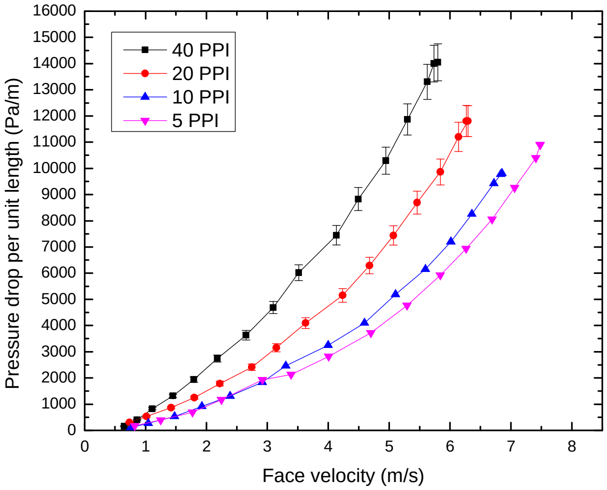

Figure 2.1: Pressured drop per unit length for foams of different porosities under dry conditions

2.2.1.2 Wet surface conditions. Condensate management is important for the performance of heat exchangers when operated under wet-surface conditions. Results for experiments conducted under wet conditions are presented in Figure 2.2. As with dry surfaces, the pressure gradient increases when the face velocity increases. Porosity plays an important role, as it does under dry conditions. Foam with 40 PPI showed higher pressure drop compared to a 10 PPI metal foam sample. An interesting feature, which was considerably different from the results for tests under dry-surface conditions, is that whereas under dry conditions the pressure gradient increases in a quadratic manner with velocity, for wet conditions the pressure gradient increased almost linearly with velocity. The relative differences for different foams under wet conditions were smaller than those observed for dry conditions.

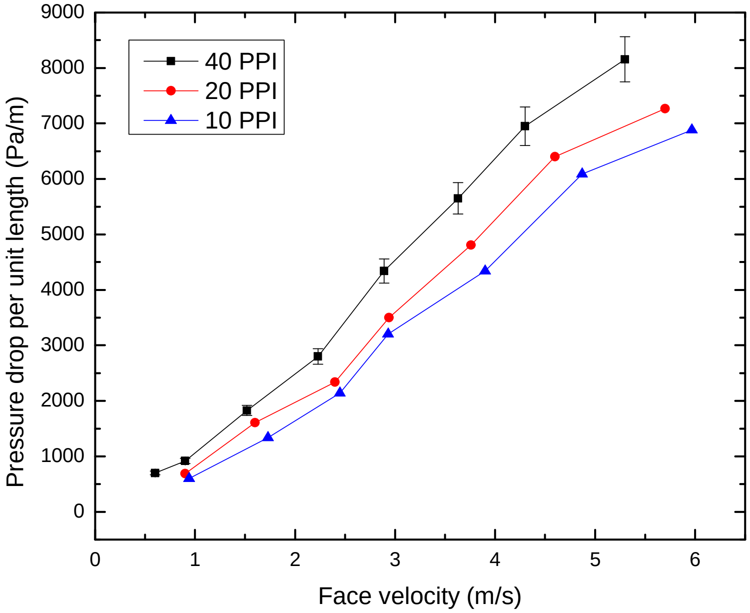

Figure 2.2: Pressured drop per unit length for foams of different porosities under wet conditions

2.2.1.3 Comparison of dry- and wet-surface data. Pressure gradient depends upon the pore size of metal foams under both dry- and wet-surface conditions. It increases as the average diameter of pores becomes smaller. An important feature was observed when the pressure gradient results for dry and wet conditions were compared to each other (10 PPI foam), as shown in Figure 2.3 (for representative data). Surprisingly, the pressure drop is only slightly larger under wet conditions when compared to dry conditions. These experiments were conducted under condensing conditions, using the same sample used for dry conditions. Many compact configurations for heat exchangers manifest a significant increase in pressure gradient under wet-surface conditions, because accumulated condensate blocks the air flow passages. However, that does not occur for these metal foams, making them promising for use under wet-surface conditions. This behavior is due to the good condensate removal ability of metal foams, which was also observed when dynamic-dip tests were performed to compare the drainage behavior to that of louver-fins (see Chapter 1). As discussed in Chapter 1, foams with smaller pores retain more water, so if the same comparison of dry vs wet test is made for foams other than 10 PPI, the relative difference will increase. Thus, better hydraulic performance (lower pressure drop) can be achieved for foams with relatively larger pores (5 and 10 PPI) under wet conditions.

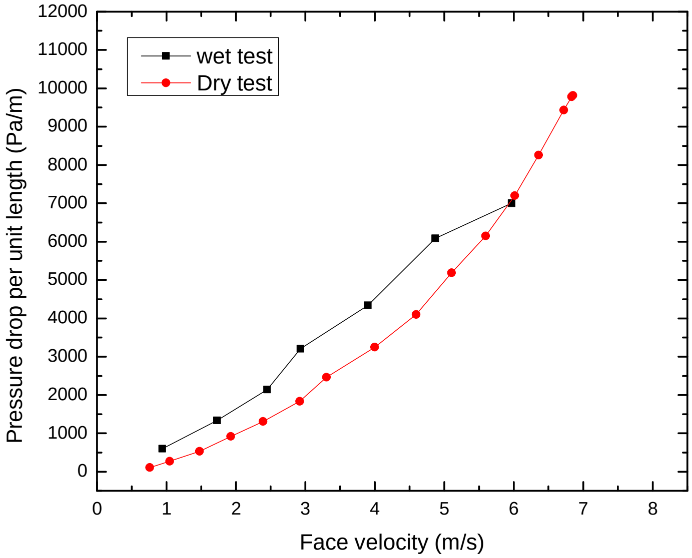

Figure 2.3: Pressured drop per unit length for 10 PPI foam under dry and wet conditions

2.2.1.4 Frosted surface condition. Frost growth can considerably reduce the performance of a heat exchanger. It reduces the heat transfer rate and also increases the pressure drop. In order to analyze metal foam heat exchanger performance under frosting conditions, experiments were conducted with the coolant flowing at temperature of -10 C on the tube side. Such low temperature resulted in frost formation on the metal foam surface, as shown in Figure 2.4. The pressure gradient variation with time is shown for three different face velocities in Figure 2.5.

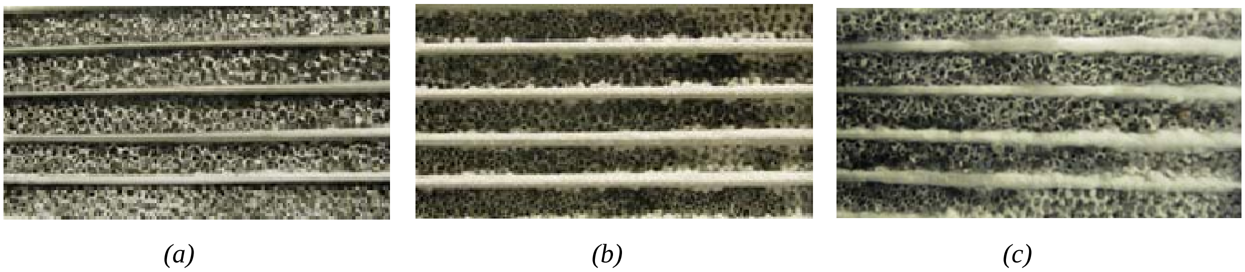
(a) (b) (c)

Figure 2.4: Frost growth at different face velocities (a) 0.5 m/s (b) 0.6 m/s (c) 0.8 m/s

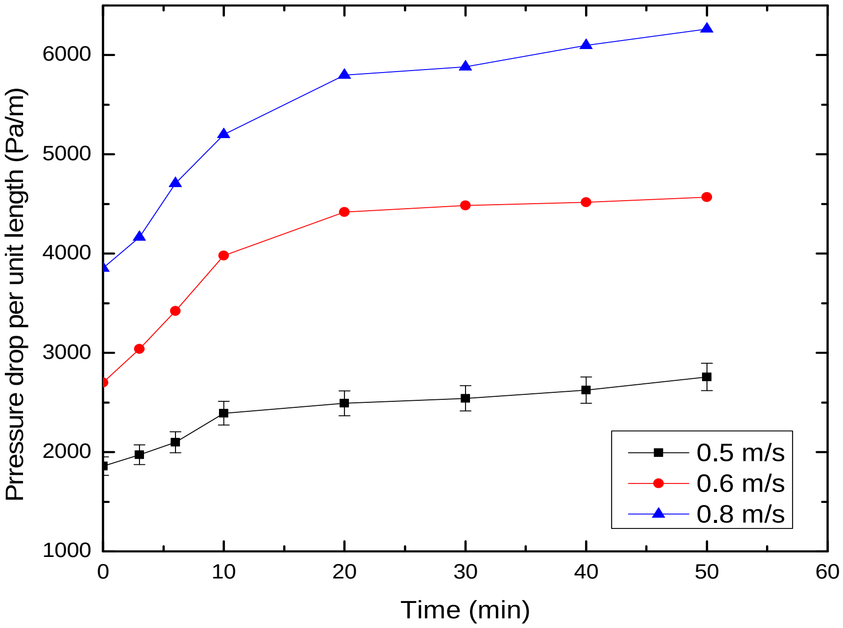

Figure 2.5: Pressured drop per unit length for 10 PPI foam under frosted conditions

For the highest face velocity of 0.8 m/s the largest pressure drop was observed at all times during the experiment. This is probably implies that not only is the pressure drop higher for a dry surface at higher velocities, but frost accumulation at high face velocity is about the same or more severe at the higher face velocity. After some time, about the same amount of time at each face velocity, the pressure gradient becomes almost constant in time, indicating the heat exchanger has probably become fully loaded with frost.

The frost formation on the metal foam fin was different from what is normally observed. As can be seen in Figure 2.6, some portion of metal foam was covered with a frost layer grown on the foam ligament, while about 20 percent of foam volume contained frost grains. The accumulation of flow-path-blocking grains resulted in larger pressure drop; thus, due to non-uniform formation of frost the velocity was also non-uniform.

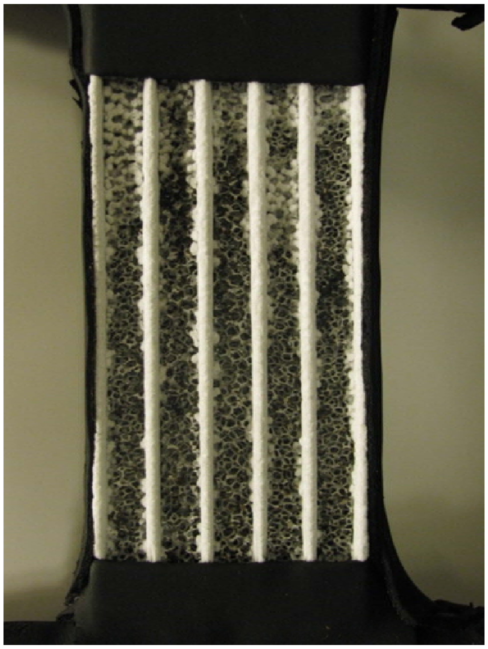

Figure 2.6: Frost formation for 10 PPI foam

2.2.2 Comparison to other porous media-wire mesh and carbon foam

Metal foams are the main focus of the current report, because of two important factors which enhance their performance for heat transfer applications

- Metal foams have high surface area to volume ratio.
- The tortuous structure enhances mixing and increases the heat transfer coefficient.

There are other similar porous media that share these characteristics, and as part of this work, comparisons to those other media have been undertaken. In order to compare the performance of metal foam with other porous media, experiments were conducted with wire mesh samples and carbon foams. The hydraulic data are presented for different type of porous materials and a comparison is made among them for the pressure-drop performance. Further comparisons, in particular heat transfer data, are presented in Chapter 3 to conclude the relative comparison for metal foams and other media.

2.2.2.1 Pressure drop for carbon foams. Geometrically carbon foams have roughly the same structure as metal foams. The tetrakiadecahedran cell geometry has been used to describe both metal foams and carbon foams. One significant difference, however, is the diameter of ligaments. For example, the ligament diameter of the 5 PPI carbon foam is almost half that of an aluminum or copper foam. As there are no data available in the literature for the characteristic lengths of carbon foams, SEM techniques were used to classify them based on the ligament diameter and the pore diameter. Figure 2.7 shows the length scale used. Multiple measurement of same sample gave an average value for pore diameter (red line) and ligament diameter (blue line). These length scales were used to reduce the data. The pressure gradient variation against face velocity for three carbon foams is shown in Figure 2.8. The carbon foam with the smallest pore diameter, the 20 PPI foam, shows the largest pressure drop. As it is for the metal foams, the pressure drop for carbon foams increases quadratically with the face velocity. In order to make a comparison, experiments were conducted with carbon foams and wire mesh with length scales similar to those of the aluminum foams. Carbon foams are similar to aluminum foams in pore diameters, but the ligament diameters are smaller. The wire meshes were selected in a way so that the characteristic "pore sizes" (diagonal length of a mesh) are comparable to different types of foams, such as 5 PPI, 10 PPI and 20 PPI.

Table 2.2: Carbon foam samples

Sample	**Face area, A_{fr} (mm× mm)**	**Ligament diameter, D_f (mm)**	**Pore diameter, D_p (mm)**
5 PPI	102×102	0.25	4.0
10 PPI	102×102	0.20	2.2
20 PPI	102×102	0.14	1.4

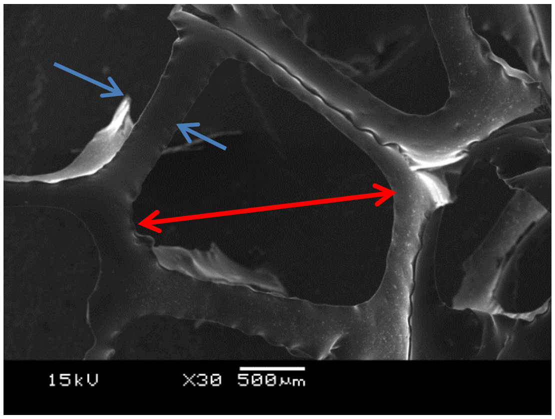

Figure 2.7: SEM image of 5 PPI Carbon foam

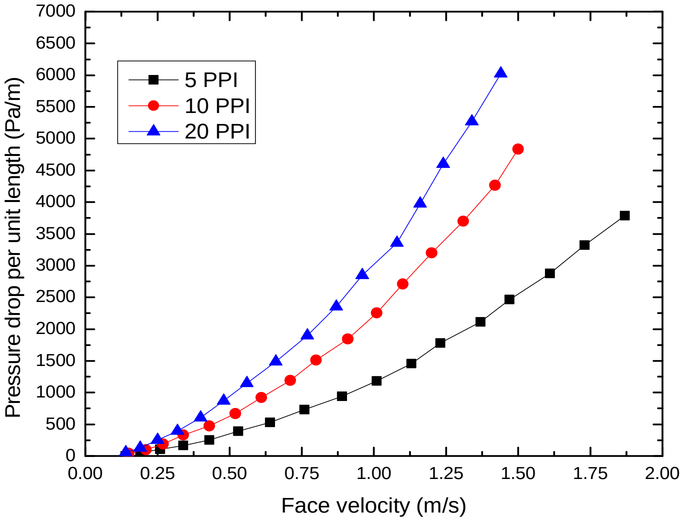

Figure 2.8: Pressured drop per unit length for carbon foams

2.2.2.2 Pressure drop for wire mesh. A porous medium was formed by stacking wire mesh together. Such media can be used as fins in heat exchanger assemblies, in a way similar to how metal foam can be used. The wire-mesh stacks have a surface-area-to-volume ratio comparable to that of metal foams. Perhaps the main difference between the wire mesh stack and the metal foam is that the wire mesh has a more obviously ordered structure than is manifested by the metal foams. In order to make a comparison, several wire mesh samples were stack together and tested under different flow velocities. The pressure drop for several mesh samples is compared in Figure 2.10. It is observed that the mesh with smaller characteristic length (defined in Figure 2.9) had the largest pressure drop. Like the behavior observed for metal and carbon foams the pressure drop increases quadratically for all wire mesh samples.

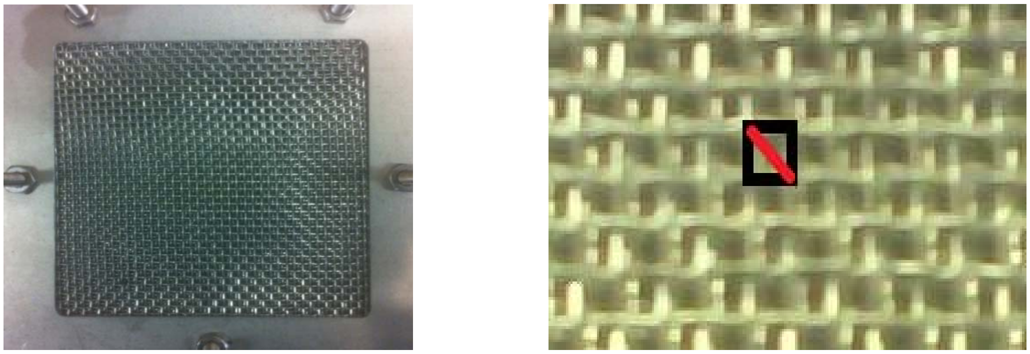

Figure 2.9: Test specimen and characteristic length for wire mesh

Table 2.3: Wire mesh samples

Sample	Face area (mm×mm)	Wire diameter (mm)	Characteristic length (mm)
1	102×102	0.90	1.5
2	102×102	0.50	3.0
3	102×102	0.50	3.0
4	102×102	0.25	1.5

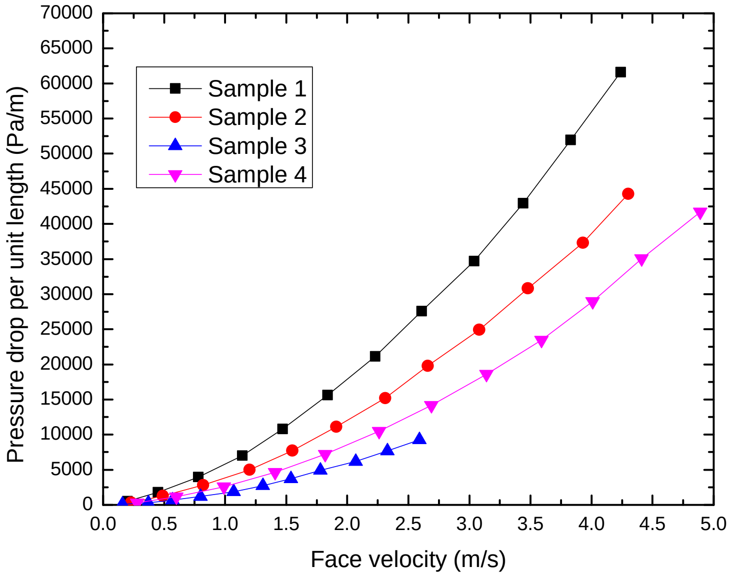

Figure 2.10: Pressured drop per unit length for wire mesh

2.2.2.3 Pressure-drop performance comparison. Different types of porous materials share the characteristic of high surface area to volume, but they show different pressure-drop performance. A relative comparison, presented in Figure 2.11, shows that this difference is significant. For samples having the same characteristic pore size (same PPI for aluminum and carbon foams, and diagonal length for wire mesh), the 5PPI carbon foam shows the smallest pressure drop and hence the least resistance to flow. The wire mesh showed performance between 5 PPI carbon and the 5 PPI aluminum foam samples. The lower pressure drop for the carbon foam is likely due to the smaller ligament diameter. The wire mesh has a pressure drop below that of the aluminum foam, but it has a comparable ligament diameter. In this case, the ordered structure of the wire mesh, and the resulting less tortuous flow path, results in a lower pressure drop.

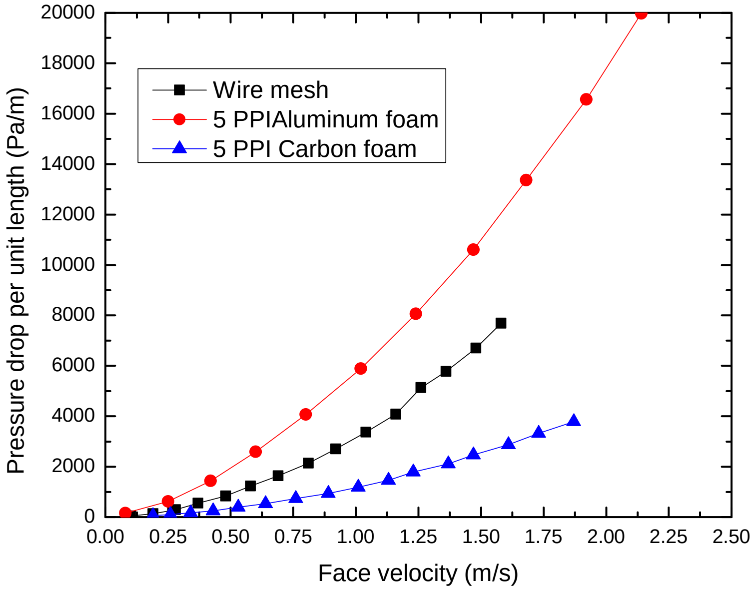

Figure 2.11: Pressured drop per unit length for different porous media

2.2.3 Pressure-drop performance and geometry

Seeking an improvement in the press-drop performance of metal foams, alternate geometric deployments of the metal foam were explored. In undertaking new deployments, face area, volume, and mass can be constraints. In this selection, a relative compassion is presented for two alternate cases, where the deployment geometry affects the performance of the heat exchanger by affecting the pressure drop. Heat transfer behavior is characterized in Chapter 4. In making these comparisons, the metal-foam deployment described earlier, in which the metal foam forms a continuous slab between two flat tubes (essentially, a “drop-in” replacement of a fin) is considered the “conventional deployment.”

<u>2.2.3.1 Folded foam configuration (80 PPI) *vs.* conventional deployment.</u> The complex structure of the metal foams promotes mixing, which enhances heat transfer; however, this structure also results in a relatively high pressure drop for flows passing through the metal foams. If thin fins of very low porosity metal foams are arranged in a folded structure, as shown in Figure 2.12, the resultant pressure drop is anticipated to be reduced. The pressure drop for this 80 PPI "folded foam" deployment is compared to that of 10 PPI foam in the conventional deployment shown earlier. The surface area per unit volume of 80 PPI metal foams is almost five times that of 10 PPI metal foams. The pressure gradient increased in linearly with velocity for the folded foam, while for the conventional 10 PPI metal foam deployment it increased quadratically with velocity. While the pressure drop for the 80 PPI folded foam was almost double that of the 10 PPI conventional deployments, the heat transfer increased three times (as discussed further in Chapter 3).

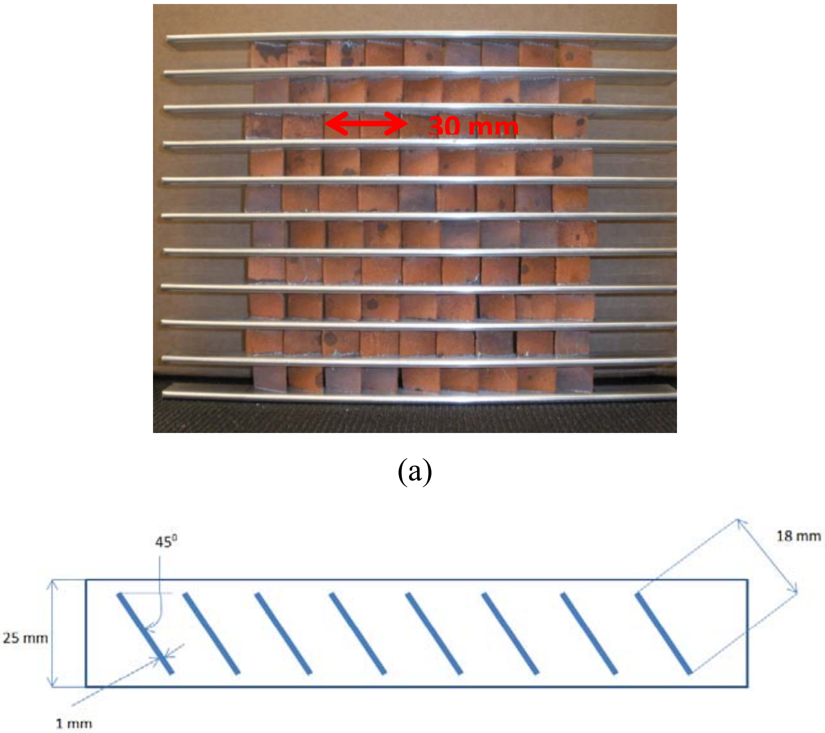

(a)

(b)

Figure 2.12: 80 PPI folded fin structure (a) front view (b) top view

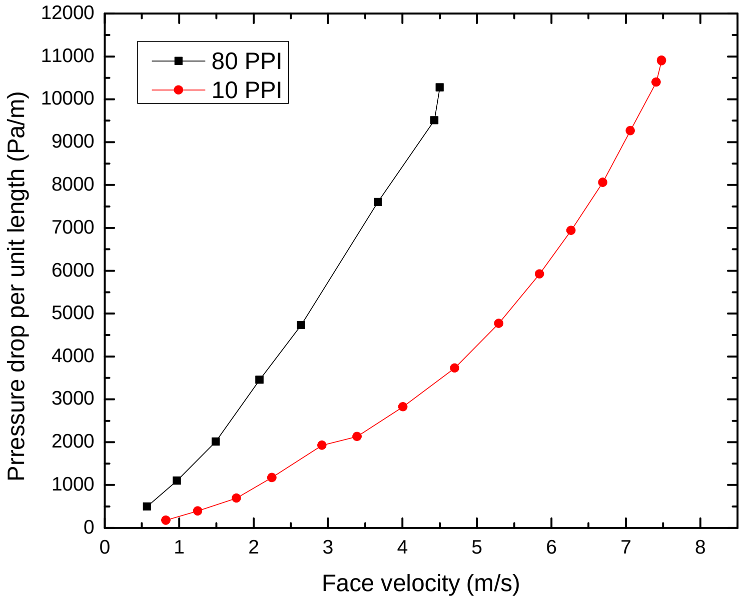

Figure 2.13: Pressured drop per unit length for foams of different geometry

<u>2.2.3.2 Annular foam *vs.* conventional deployment.</u> Another comparison was undertaken for foam deployed as an annulus around round tubes forming a heat exchanger. There were two round-tube heat exchangers used in this comparison, and they had identical face areas and flow depths. *Sample 1* had a continuous block deployment of foam, with round tubes running through the foam block. *Sample 2* had an annular metal foam layer on the round tubes. The thickness of the annulus of metal foam was such that there was no bypass of flow; i.e., the outer surface of the annulus of metal foam on one tube touched the outer surface of the annulus of metal foam on the neighboring tube (see Figure 2.14).

(a) *(b)*

Figure 2.14: Metal foam heat exchangers with different geometry

(a) Sample 1-continuous block structure (b) Sample 2-annulur structure

The pressure drop data for the two round-tube foam heat exchangers are presented in Figure 2.15. It is obvious that the sample with a continuous metal foam block had a higher pressure drop compared to the annular foam configuration. As presented in detail in Chapter 3, there was almost no difference in the heat transfer performance of these heat exchangers.

These comparisons show that the higher pressure drop associated with metal foams can be mitigated by judicious deployment of the metal foam, so that the heat transfer performance remains excellent, and the fan power requirements are reduced.

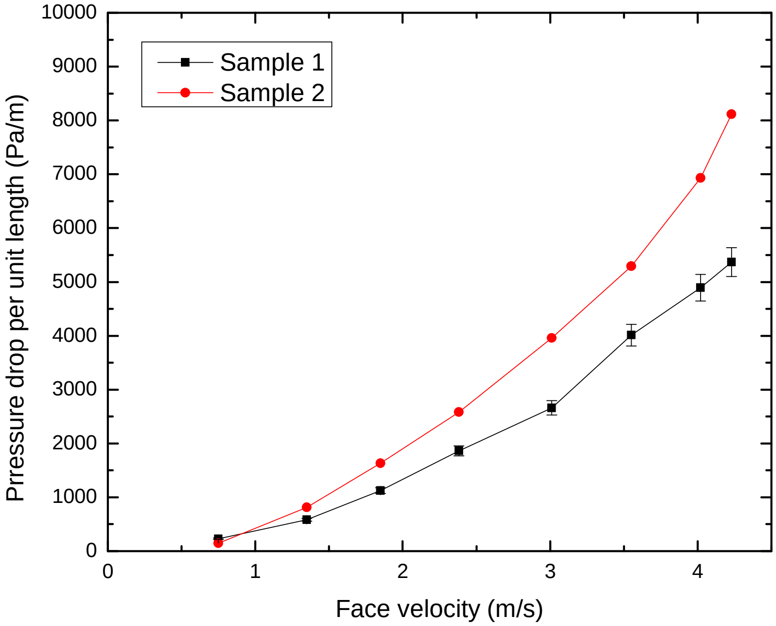

Figure 2.15: Pressured drop per unit length for foams of different geometry

2.2.4 Effect of flow depth

In order to explore the effect of flow depth, or flow development, on the pressure drop, experiments were conducted for varying test specimen thickness. As can be seen from Figure 2.16, pressure drop per unit length is constant for the extremes in pore size, the 5 PPI and 40 PPI metal foams, over the range of flow depths considered. The results ensure that, although the pressure drop per unit length depends on the type of foam, the effect of flow depth can be neglected, as the pressured drop per length is almost constant for these flow depths. The data suggest that the flow essentially reaches a fully developed condition in the aluminum foams.

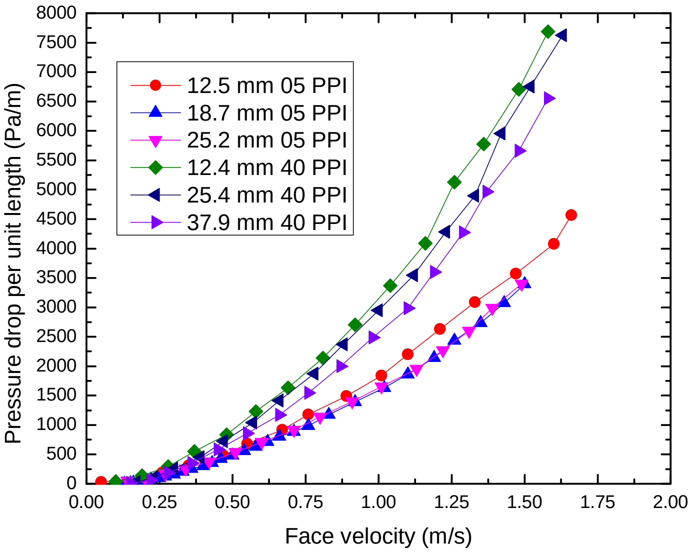

Figure 2.16: Effect of flow depth on pressure drop for aluminum foams

This fully developed behavior was not observed for the carbon foams, as is demonstrated by the results shown in Figure 2.17. The pressure drop per unit length plotted against the face velocity for a 10 PPI sample varies significantly with flow depth. The larger pressure gradient manifested for shorter flow depths is consistent with a flow development effect, strongly suggesting that flow development length depends on ligament diameter, the only significant geometric difference between the aluminum and the carbon foams.

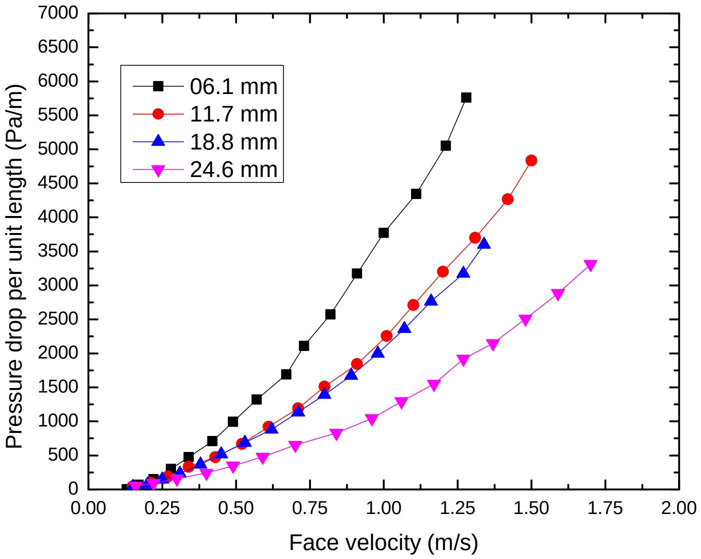

Figure 2.17: Effect of flow depth on pressure drop for carbon foam (10 PPI)

2.3 Modeling the pressure drop performance

As described in Chapter 1, there has been tremendous effort to quantify the pressure-drop behavior of porous media, such as metal foams. In this section both conventional and modified approaches have been used to develop relationships for pressure drop. The conventional approach is based on defining the parameters such as permeability and inertia coefficient by curve fitting the pressure drop data. While this approach is widely adopted, it fails to completely capture the physics reflected in the data. A better approach appears to be to reduce the data based on the pore diameter or the hydraulic diameter of specimen and present the results as curve fits in dimensionless space as explained later.

2.3.1 Comparison to existing models

As discussed earlier, many researchers have tried to generalize and modify the Darcy model for flow through porous media to predict the pressure-drop performance of metal foams. Such models were found to work well for a certain, narrow range of flow conditions but cannot be used to predict the performance over the range of the current experiments. As an example, experimental results are compared to the modified Darcy model of Bhattacharya *et al*. [20] in Figure 2.18. The model of Bhattacharya *et al*. [20] is given as Eq. (2.8):

$$-\frac{dp}{dx}=\frac{\mu V}{K}+\frac{\rho f}{\sqrt{K}}V^2 \tag{2.8}$$

In Eq. (2.8), K is the permeability, and f is a dimensionless inertia coefficient. As shown in Figure 2.17, the model makes reasonable predictions at the lowest velocities, but it under predicts pressure drop by as much as 40% at intermediate velocities.

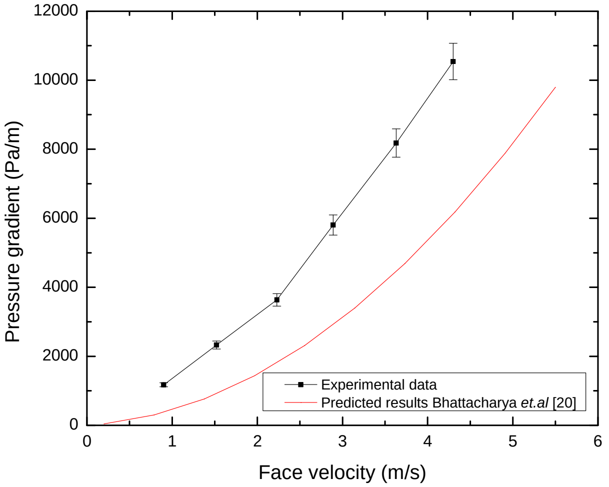

Figure 2.18: comparison of experimental data with pressure drop model for 40PPI sample

2.3.2 Determination of permeability and inertia coefficient

Based on the modified Darcy Flow model, the pressure gradient can be related to the hydraulic characteristic of the foam by the relation involving permeably and inertia coefficient.

$$\frac{\Delta P_f}{L} = \frac{\bar{\mu}}{K} V + \bar{\rho} C V^2 \qquad (2.9)$$

The permeability is K, and C is the inertia coefficient (cf. Eq. 2.9). The average viscosity and density of fluid are $\bar{\mu}$ and $\bar{\rho}$, respectively. The average properties are based on the conditions upstream and downstream of test section. This relation can be rearranged as

$$\frac{\Delta P_f}{LV} = \frac{\bar{\mu}}{K} + \bar{\rho} C V \qquad (2.10)$$

The form of Eq. (2.10) provides a linear relationship in face velocity

$$\frac{\Delta P_f}{LV} = A + BV \qquad (2.11)$$

With

$$A = \frac{\bar{\mu}}{K} \qquad (2.12)$$

and

$$B = \bar{\rho}C \qquad (2.13)$$

These relations for A and B were used to determine the permeability and inertia coefficient for three different types of porous media. The resulting reduced pressure drop (pressure gradient divided by face velocity) was plotted against the face velocity and a linear fit provided *A* and *B*, and thus *K* and *C*. An example of such a plot and the resulting fit is provided in Figure 2.18. The results are summarized and compared to values from the literature in Table 2.4.

The values from experiments are of the same order of magnitude as those from the literature, but there are significant discrepancies. As the pressure gradient for carbon foams depended on the flow depth. So permeability and inertia coefficient are also function of flow depth, for that developing flow. Hence permeability and inertia coefficient cannot be considered physical properties for the hydraulic performance of those porous media—a significant shortcoming in the approach. Nevertheless, not that an excellent fit to the current data is achieved. In the example of Figure 2.19, the final fit to pressure gradient has a correlation coefficient of R^2=0.99792. Thus, the parameters given in Table 2.4 can be used with Eq. (2.9) to obtain good fits to the current data. However, a more general approach is explored in the next section.

Table 2.4: Permeability and inertia coefficient for porous media*

Porous media	K_{exp}	C_{exp}	$K_{Literature}$	$C_{Literature}$
5 PPI Al	$3.792(10^{-7})$	0.132	$2.70(10^{-7})$	0.097
10 PPI Al	$2.722(10^{-7})$	0.095	$1.49(10^{-7})$	0.07
20 PPI Al	$8.369(10^{-8})$	0.082	$1.42(10^{-7})$	0.10
40 PPI Al	$6.906(10^{-8})$	0.086	$5.68(10^{-8})$	0.0899
5 PPI C (12.5 mm)	$1.240(10^{-7})$	0.382	-	-
5 PPI C (18.8 mm)	$5.460(10^{-7})$	0.362	-	-
5 PPI C (24.7 mm)	$1.518(10^{-7})$	0.345	-	-
10 PPI C (06.1 mm)	$2.392(10^{-6})$	0.290	-	-
10 PPI C (11.7 mm)	$1.157(10^{-7})$	0.269	-	-
10 PPI C (18.8 mm)	$1.287(10^{-7})$	0.223	-	-
10 PPI C (24.6 mm)	$9.949(10^{-8})$	0.211	-	-
20 PPI C (06.0 mm)	$4.445(10^{-8})$	0.201	-	-
20 PPI C (12.8 mm)	$5.665(10^{-8})$	0.186	-	-
20 PPI C (19.1 mm)	$6.098(10^{-8})$	0.172	-	-
20 PPI C (24.9 mm)	$1.367(10^{-7})$	0.168	-	-
Sample 1	$5.057(10^{-8})$	0.233	-	-
Sample 2	$2.368(10^{-8})$	0.182	-	-
Sample 3	$2.174(10^{-8})$	0.167	-	-
Sample 4	$1.109(10^{-8})$	0.089	-	-

* $K_{Literature}$ and $C_{Literature}$ are taken from Bhattacharya *et al.* [20].

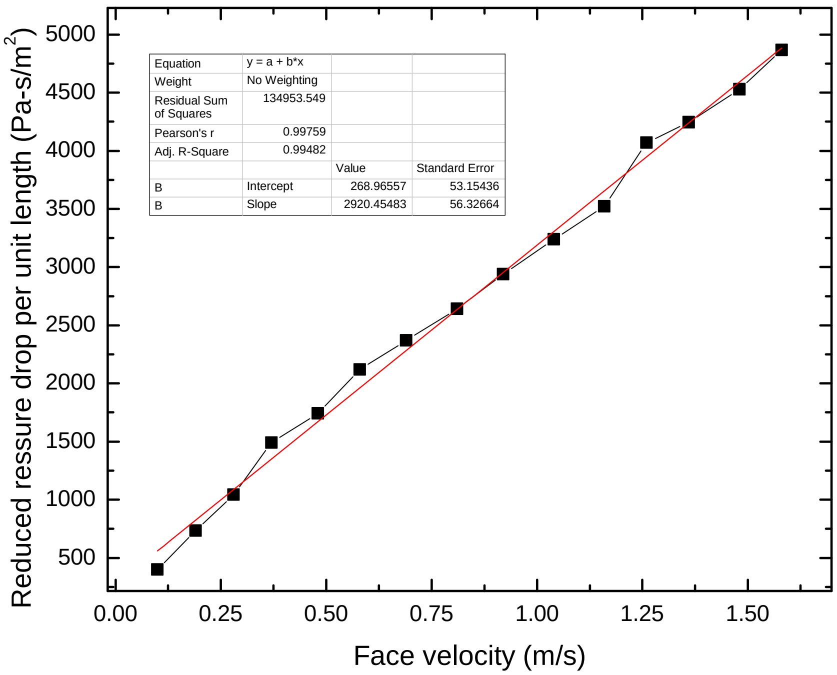

Equation	y = a + b*x		
Weight	No Weighting		
Residual Sum of Squares	134953.549		
Pearson's r	0.99759		
Adj. R-Square	0.99482		
		Value	Standard Error
B	Intercept	268.96557	53.15436
B	Slope	2920.45483	56.32664

(a)

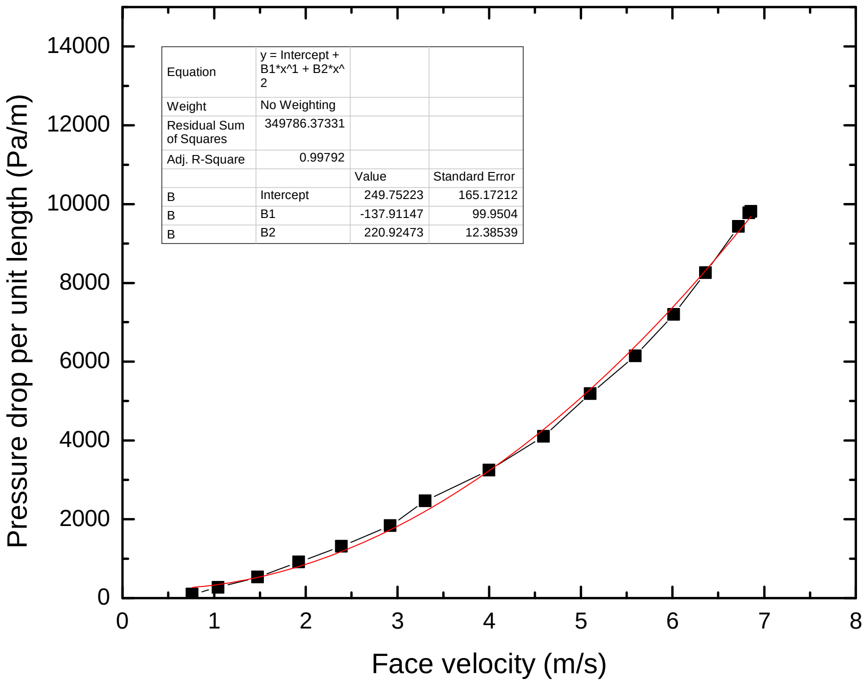

Equation	y = Intercept + B1*x^1 + B2*x^2		
Weight	No Weighting		
Residual Sum of Squares	349786.37331		
Adj. R-Square	0.99792		
		Value	Standard Error
B	Intercept	249.75223	165.17212
B	B1	-137.91147	99.9504
B	B2	220.92473	12.38539

(b)

Figure 2.19: Curve fitting for determining permeability and inertia coefficient: (a) reduced pressure gradient plot for determination of permeability and inertia coefficient; (b) resulting fit to pressure gradient, R^2=0.99792.

2.3.3 Identification of parameters (Buckingham Pi terms)

Experimental data show that geometrical characteristics of foams and test specimen, flow conditions, and the physical properties are related to the pressure-drop performance of metal foam heat exchangers. In this section key parameters are listed, and an application of the Buckingham Pi theorem is undertaken to determine the set of non-dimensional numbers to represent the data. The key parameters are:

- *Physical properties of fluid:* density, viscosity
- *Flow parameters:* pressure, face velocity
- *Geometric parameters:* flow depth, pore diameter, ligament diameter

Thus, for fully developed flow, with negligible entrance, exit, and wall effects, the pressure gradient (pressure drop per unit flow depth) can be related to the other parameters:

$$\frac{\Delta P}{L} = fncn\left(\rho, \mu, D_f, D_p, V\right) \tag{2.14}$$

As a matter of convention, the hydraulic diameter is anticipated to account for geometrical parameters. Under such an assumption, effectively

$$\frac{\Delta P}{L} = fncn(\rho, \mu, D_h, V) \tag{2.15}$$

Eq. (2.15) is written in order to follow convention; however, it must be recognized that the geometric complexity of the metal foams implies at least one additional length scale may appear. Proceeding in an *ad hoc* way, one such characteristic length, L_c, yet to be determined, is introduced back into the Buckingham-Pi analysis. This admittedly *ad hoc* approach then yields:

$$f_{Lc} = \frac{L_c}{2}\frac{\Delta P}{L}\frac{1}{\bar{\rho}V^2} \tag{2.16}$$

and

$$\mathrm{Re}_{Dh} = \frac{\bar{\rho}VD_h}{\bar{\mu}} \tag{2.17}$$

with

$$f_{Lc} = fncn(\mathrm{Re}_{Dh}, L_c / D_h) \tag{2.18}$$

The ‘2’ appears in Eq. (2.16) so that if L_c=D_h the conventional definition of f prevails.

2.3.4 Data reduction for determination of *f* factor

For comparison purposes, the pressure-drop performance of the metal foam heat exchangers is presented following the convention of Kays and London, wherein the friction factor is related to the Reynolds number based on hydraulic diameter. With some as yet determined length scale, L_c, as an additional characteristic length and $\bar{\rho}$ the average density. The relationship of Eq. (2.16) can be modified as

$$f_{Lc} = \frac{\Delta P}{L} \frac{\bar{\rho}}{G^2} \frac{L_c}{2} \qquad (2.19)$$

where G mass flux, $G = \bar{\rho} V_{\max}$, with $V_{\max}$ the velocity at the minimum free-flow area:

$$A_{\min} = \sigma A_{fr} \qquad (2.20)$$

For metal foam, the minimum free flow area, $A_{\min}$, is related to the frontal area directly by the porosity, ε, because $\sigma = \varepsilon$. Thus,

$$A_{\min} = \varepsilon A_{fr} \qquad (2.21)$$

The characteristic length, L_c, can be defined by many ways. Some of the options follow:

- Heat exchanger characteristics: hydraulic diameter, flow depth, tube spacing
- Foam characteristics: pore diameter, ligament diameter, ligament length

The hydraulic diameter follows convention:

$$D_h = \frac{4 A_{\min} L}{A_T} \qquad (2.22)$$

with

$$A_T = A_{base} + A_{foam} \qquad (2.23)$$

The total surface area, A_T, is comprised of the exposed tube area, A_{base}, and the surface area of the metal foam, A_{foam}. Again, if D_h is used as L_c in Eq. (2.19), then the conventional definitions of Kays and London prevail, and we expect f=fncn(Re_{Dh}). In the approach embodied in Eqs (2.19) to (2.23), that convention need not be followed. However, the geometric parameters must be known.

The foam surface area can be obtained from data provided by the manufacturer, as shown in Figure 2.20.

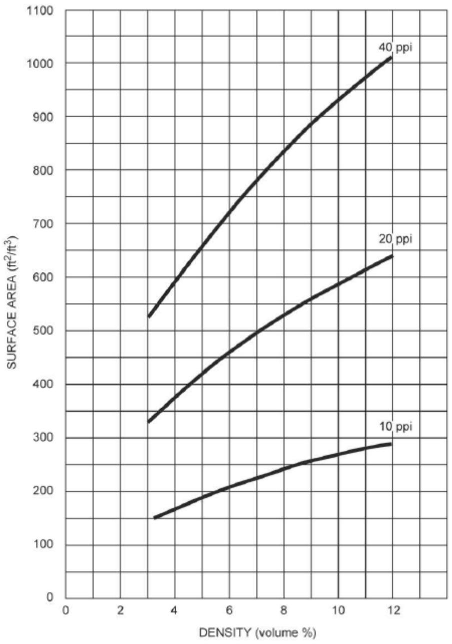

Figure 2.20: Surface area per unit volume for different porosities

In order to determine A_{min}, image processing was used, rather than simply relying on the reported porosities. Images from X-ray tomography were analyzed as suggested in Figure 2.21. In order to identify the metal in the cross sectional view of foam, a pixel threshold value of 100 was set, with pixel values ranging from 0 (black) to 255 (white). The number of pixels exceeding this threshold divided by the total gave $A_{\mathrm{min}}/A_{\mathrm{fr}}$. The process was repeated for five images for each type of foam and the values were averaged. The results are given in Table 2.5, and other geometric properties are reported in Table 2.6.

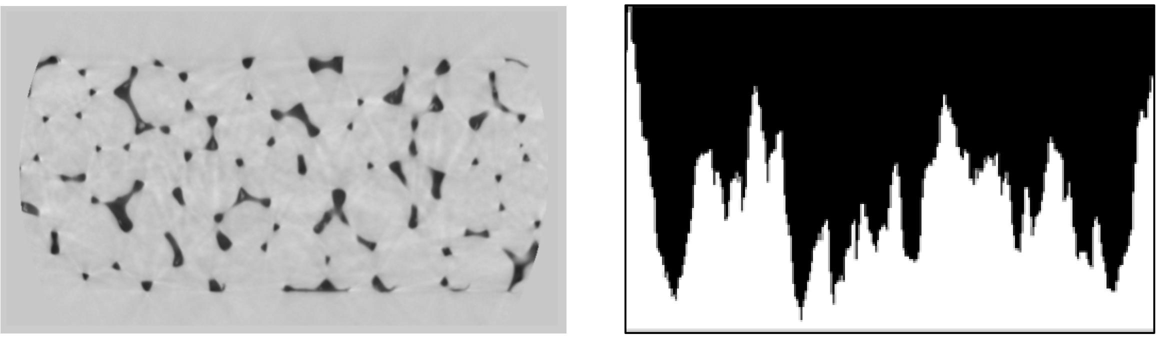

(a) (b)

Figure 2.21: Image processing for cross sectional view of 5 PPI metal foam (a) X-rays image of foam slice (b) intensity distribution of the image.

Table 2.5: Free-flow cross-sectional area of metal foams*

Foam	Measured A_{min}/A_{fr}	Manufacturer's reported porosity
5 PPI	0.988	0.97
10 PPI	0.977	0.96
20 PPI	0.971	0.95
40 PPI	0.957	0.93

Table 2.6: Geometric parameters of metal foams*

Foam designation	Pore diameter, D_p (mm)	Ligament diameter, D_f (mm)	Hydraulic diameter, D_h (mm)
5 PPI	4.02	0.50	6.34
10 PPI	3.28	0.45	4.61
20 PPI	2.58	0.35	2.69
40 PPI	1.80	0.20	1.74

* Note that small variations in geometric data presented in Chapter 1 and those given in Tables 2.5 and 2.6 are due to sample-to-sample variation. The geometric data presented here were obtained from the specimens used for pressure-drop experiments, and these data were used for data reduction of those pressure-drop measurements.

For comparison to other heat exchangers, the friction factor is plotted versus *Re* for various foams, with L_c=D_h, in Figure 2.22. Comparing to the general trends in Kays and London, it is clear that the metal foams have a very high *f*-factor, in the conventional sense. Moreover, because the data do not collapse to a single curve, there is a strong suggestion that another length scale is important (not simply D_h).

Through a trial and error process, it was found that the friction factor data would collapse to a single curve, with a goodness of fit suitable for engineering design, if pore diameter was included as a characteristic length. In this process 2 of 64 data were discarded as outliers; the resulting fit had a relative RMS deviation of ±14.86%, and almost all of the data were predicted to within ±20%. The fit uses pore diameter as L_c, with the Reynolds number based on hydraulic diameter:

$$f_{D_p} = \frac{\Delta P}{L}\frac{\bar{\rho}}{G^2}\frac{D_p}{2} = 1.975\,\mathrm{Re}_{D_h}^{-0.1672}\left(D_p/D_h\right)^{-3.708} \tag{2.24}$$

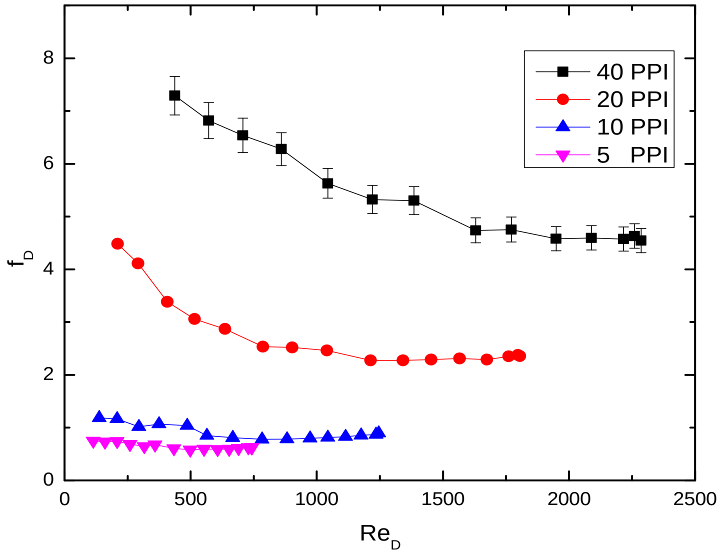

Figure 2.22: Friction factor for different porosities, hydraulic diameter is the characteristic length

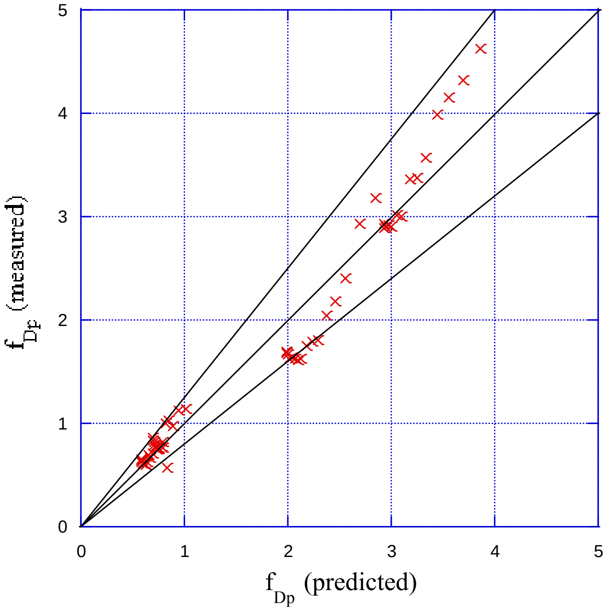

Figure 2.23: Friction factor with pore diameter as a characteristic length, measured versus predicted (Eq. 2.24). The relative RMS deviation is ±14.86%; limits of ±20% are shown in the plot.

2.4 Conclusion

The pressure-drop performance of the metal foams has been analyzed. It is clear that pore diameter is an important parameter in determining the pressure drop. The pressure drop increases quadratically as the face velocity increases, and this trend is observed under both dry- and wet-surface conditions. At a fixed face velocity, the pressure drop increases for wet-surface conditions as compared to dry-surface conditions; however, the increase is not as large as is manifested for many other compact heat exchangers, reinforcing the excellent condensate drainage behavior reported in Chapter 1. When comparing the metal foams with carbon foams and wire meshes, the same general trends in pressure drop with velocity and porosity are observed. However, the carbon foam, with a smaller ligament diameter and the wire mesh due to ordered structure show lower pressure drop than the metal foams. The geometry of metal foam heat exchangers can considerably reduce the pressure drop without compromising the heat transfer performance (as discussed further in the next chapter). While the flow depth is important to overall pressure drop, the pressure gradient was independent of flow depth for the metal foams and wire mesh—the pressure gradient depended on flow depth for the carbon foams. For carbon foams, the pressure gradient was lower for smaller flow depths. Using an *ad hoc* approach with the Buckingham Pi theorem as a basis, it was found that more than one length scale is important to the pressure gradient in metal foams. By using a Reynolds number based on hydraulic diameter, a curve fit for the friction factor based on pore diameter was developed with reasonable engineering accuracy.

2.5 References

[1] Zhou, J., Mercer, C., and Soboyejo, W. O. "An investigation of the microstructure and strength of open-cell 6010 aluminum foam," *Metallurgical and Material Transactions,* Vol. 33A5, pp. 1413–1427, 2002.

[2] Ashby, M. F., Evans, A. G., Fleck, N. A., Gibson, L. J., Hutchinson, J. W., and Wadley, H. N. G., *Metal Foams, a Design Guide*, Butterworth- Heinemann, Woburn, MA, Chap. 1, pp. 181–188, 2000.

[3] Sullines, D., and Daryabeige, K. "Effective thermal conductivity of high porosity open cell nickel foam," *Proceedings of 35th AIAA Thermo-physics Conference*, Anaheim, CA, June 11–14, IAAA Paper No. 2001–2819, 2001.

[4] Vafai, K., and Tien, C. L. "Boundary and inertia effects on convective mass transfer in porous media," *International Journal of Heat and Mass Transfer*, Vol. 25, pp. 1183–1190, 1982.

[5] Crosnier, S., Rivam, R., Bador, B., and Blet, V. "Modeling of gas flow through metallic foams," *Presented at the 1st European Hydrogen Energy Conference*, Sept. 2–5, Alpexpo-Alpes Congrés, Grenobel, France, 2003.

[6] Khayargoli, P., Loya, V., Lefebvre, L. P., and Medraj, M. "The Impact of Microstructure on the Permeability of Metal Foams," Proceedings of the CSME, June 1-4, London, Canada, pp. 220-228, 2004.

[7] Bastawros, A. F. "Effectiveness of Open-Cell Metallic Foams for High Power Electronic Cooling," *Presented at Symposium on the Thermal Management of Electronics*, IMECE, Anaheim, CA, 1998.

[8] Kaviany, M., *Principles of Heat Transfer in Porous Media*, Springer-Verlag, New York, Chapter. 2, 1995.

[9] Lage, J. L. “The fundamental theory of flow through permeable media form Darcy to turbulence,” *Transport Phenomena in Porous Media*, D.B. Ingham and I. Pop, eds., Pergamon, New York, pp. 1–30, 1998.

[10] Nield, D. A. “Modeling fluid flow in saturated porous media and at interfaces,” *Transport Phenomena in Porous Media II*, New York, pp. 1-19, 2002.

[11] Nield, D. A., and Bejan, A., *Convection in Porous Media*, 2nd ed., Springer, New York, Chap. 1, 1999.

[12] Bastawros, A. F., Evans, A. G., and Stone, H. A. “Evaluation of cellular metal heat transfer media,” *MECH 325, Harvard University Report*, Cambridge, MA, 1998.

[13] Lage, J. L., Antohe, B. V., and Nield, D. A., “Two types of nonlinear pressure-drop versus flow-rate relation observed for saturated porous media,” *ASME Journal of Fluids Engineering*, Vol. 119, pp. 700-706, 1997.

[14] Hwang, J. J., Hwang, G. J., Yeh, R. H., and Chao, C. H., “Measurement of interstitial convective heat transfer and frictional drag for flow across metal foams,” *ASME Journal of Heat Transfer*, Vol. 124, pp. 120–129, 2002.

[15] Seguin, D., Montillet, A., and Comiti, J. “Experimental characterization of flow regimes in various porous media-I: Limit of Laminar Flow Regime,” *Chemical Engineering Science*, Vol.53, pp. 3751–3761, 1998.

[16] Decker, S., Mößbauer, S., Nemoda, D. T., and Zapf, T., “Detailed experimental characterization and numerical modeling of heat and mass transport properties of highly

porous media for solar receivers and porous burners," Lehrstuhl für Strömungsmechanik Universität Erlangen-Nürnberg Cauerstr. 4, D-91058 Erlangen, Germany, 2000.

[17] Tadrist, L., Miscevic, M., Rahli, O., and Topin, F. "About the use of fibrous materials in compact heat exchangers," *Experimental Thermal-Fluid Science*, Vol. 28, pp. 193–199, 2004.

[18] Kim, S. Y., Paek, J. W., and Kang, B. H. "Flow and heat transfer correlations for porous fin in a plate-fin heat exchanger," *ASME Journal of Heat Transfer*, Vol. 122, pp. 572–578, 2000.

[19] Paek, J. W., Kang, B. H., Kim, S. Y., and Hyun, J. M. "Effective thermal conductivity and permeability of aluminum foam materials," *International Journal Thermo-physics*, Vol. 21, pp. 453–464, 2000.

[20] Bhattacharya, A., Calmidi, V. V., and Mahajan, R. L. "Thermophysical properties of high porosity metal foams," *International. Journal of Heat and Mass Transfer*, Vol. 45, pp. 1017–1031, 2002.

[21] Du Plessis, J. P., Montillet, A., Comiti, J., and Legrand, J. "Pressure drop prediction for flow through high porosity metallic foams," *Chemical Engineering Science*, Vol. 49, pp. 3545–3553, 1994.

[22] Fourie, J. G., and Du Plessis, J. P. "Pressure drop modeling in cellular metallic foams," *Chemical Engineering Science.*, Vol. 57, pp. 2781–2789, 2002.

[23] Despois, J. F., and Mortensen, A. "Permeability of open-cell microcellular materials," *Acta Material,* Vol. 53, pp. 1381–1388, 2005.

[24] Boomsma, K., Poulikakos, D., and Ventikos, Y. "Simulation of flow through open cell metal foams using an idealized periodic cell structure," *International Journal of Heat and Fluid Flow*, Vol. 24, pp. 825–834, 2003.

[25] Schmierer, E. N., Razani, A., Keating, S., and Melton, T. "Characterization of high porosity open-celled metal foam using computed tomography," *Proceedings of the ASME International Mechanical Engineering Congress*, Nov. 13–20, Anaheim, CA, 2004.

[26] Benouali, A., Froyen, L., Delerue, J. F., and Wevers, M. "Mechanical analysis and microstructure characterization of metal foams," *Material Science Technology*, Vol. 18, pp. 489–494, 2002.

[27] Olurin, O. B., Arnold, M., Körner, C., and Singer, R. F. "The investigation of morphometric parameters of aluminum foams using micro-computed tomography," *Material Science Engineering,* Vol. 328, pp. 334–343, 2002.

[28] Scheffler, F., Herrmann, R., Schwieger, W., and Scheffler, M. "Preparation and properties of an electrically heatable aluminum foam/zeolite composite," *Microporous Mesoporous Material,* Vol. 67, pp. 53–59, 2004.

[29] Boomsma, K., Poulikakos, D., and Zwick, F. "Metal foams as compact high performance heat exchangers," *Mechanics of Materials*, Vol. 35, pp. 1161–1176, 2003.

[30] Boomsma, K., and Poulikakos, D. "The effect of compression and pore size variations on the liquid flow characteristics in metal foams," *ASME Journal of Fluids Engineering*, Vol. 124, pp. 263–272, 2002.

[31] Antohe, B., Lage, J. L., Price, D. C., and Weber, R. M. "Experimental determination of the permeability and inertial coefficients of mechanically compressed aluminum porous matrices," *ASME Journal of Fluids Engineering*, Vol. 119, pp. 404–412, 1997.

[32] Dukhan, N., and Alvarez, A. “Pressure drop measurements for air flow through open-cell aluminum foam,” *Proceedings ASME International Engineering Congress*, Nov. 13–19, Anaheim, CA, 2004.

[33] Noh, J.S., Lee, K.B., and Lee, C.G. “Pressure loss and forced convective heat transfer in an annulus filled with aluminum,” *International Communication of heat and mass Transfer*, pp. 434–444, 2006.

[34] Naakteboren, C., Krueger, P.S., and Lage, J.L. “Limitations of Darcy’s law of inlet and exit pressure-drops,” *International Conference on Porous Media and Applications,* pp. 1–7, 2004.

[35] Naakteboren, C., Krueger, P.S., and Lage, J.L. “The effect of inlet and exit pressure-drop on the determination of porous media permeability and form coefficient,” *ASME Fluids Engineering Division Summer Meeting and Exhibition* Houston, TX, 2004.

[36] Medraj, M., Baril, E., Loya, V., and Lefebvre, L.P. “The effect of microstructure on the permeability of metallic foams,” *Journal of Material Science,* Vol. 42, pp. 4372–4383, 2007.

[37] Innocentini, M.D.M., Lefebvre, L.P., Meloni, R.V., and Baril, E. “Influence of sample thickness and measurement set-up on the experimental evaluation of permeability of metallic foams,” *Journal of Porous Martials,* 2009.

[38] Baril, E., Mostafid, A., Lefebvre, L.P., and Medraj, M. “Experimental demonstration of entrance/exit effects on the permeability measurements of porous materials,” *Advanced Engineering Materials,* Vol. 10, pp.889–894, 2008.

[39] ISO 4638:1984- *Polymeric materials, cellular flexible* Determination of air flow permeability.

[40] ISO 7231:1984- *Polymeric materials, cellular flexible* Method of assessment of air flow value at constant pressure-drop.

[41] ASTM D737 *Standard test method for air permeability of textile fabrics.*

[42] ASTM F 778–88 *Standard methods for gas flow resistance testing of filtration media.*

[43] ASTM D3574-03 *Standard test methods for flexible cellular materials*-slab, bonded, and molded urethane foams

[44] Du Plessis, J.P., and Woudberg, S. "Predicting the permeability of very low porosity sandstones," *Chemical Engineering Science*, Vol. 63, 2008.

[45] Ergun, S. "Fluid flow through packed columns," *Chemical Engineering Progress*, Vol. 48, pp. 89–94, 1952.

[46] Dukhan, N., and Patel, P. "Equivalent particle diameter and length scale for pressure drop in porous metals," *Experimental Thermo-Fluid Science*, Vol. 32, pp. 1059–1067, 2008.

Chapter 3 — Heat transfer performance of metal foams

3.1 Introduction

Metallic and graphitic foams are commercially available. These foams consist of a structure that encloses open cells as described in detail in Chapter 1. Most commercially available metal foams are made of aluminum, copper, nickel, or metal alloys. Metal foams appear to have attractive properties for heat transfer applications and have been used for thermal applications in cryogenics, combustion chambers, geothermal systems, petroleum reservoirs, catalytic beds, compact heat exchangers for airborne equipment, air cooled condensers and compact heat sinks for power electronics. The foam provides an extended surface with high surface area and complex flow paths. That combination is expected to yield excellent convective heat transfer performance. Foams may also be more structurally stable than thin sheet-metal fins and may offer other manufacturing advantages. If metal foams are to be widely used in thermal systems, their pressure-drop and heat transfer characteristics must be available to potential users in terms that fit into current design methods. In the previous chapter, the pressure-drop performance was presented in detail. In this chapter the heat transfer performance will be explore; that includes an evaluation of the bond resistance (thermal contact resistance) between the foam and the primary surface. In the current work, the heat transfer characteristics of different rigid, open cell, aluminum metal foams are examined for HVAC&R applications. Metal foams are characterized by the size of the windows (or pore diameter) which correlates with the nominal pore density (PPI), the strut diameter and length, the porosity ε (volume of void divided by the total volume of the solid matrix and void). Many recent reports on metal-foam heat transfer during single phase flow in foams have been published, but to date there is no general model available for thermal-hydraulic performance of metal foams, and researchers must rely on experimental data. Through the work reported in this chapter, new experimental data for heat transfer with metal foams are provided. This chapter focuses on the experimental analysis of heat transfer during air flow in aluminum foams with different number of pores per inch, different geometry and different base metals.

3.1.1 Literature review

Cellular materials are characterized by cell size, sample porosity or relative density, ligament thickness and length, as shown in Fig. 3.1. Over the past few decades, many different research groups have studied the heat transfer characteristics of these porous media, experimentally and analytically. Calmidi *et al.* [1, 2] characterized the heat transfer behavior of different aluminum foams in a wind tunnel. The measurements were conducted by heating the base of the foam and using air as the coolant. The seven tested aluminum foams were designated to range from 5 PPI to 40 PPI, with a porosity that varied between 0.97 and 0.89, respectively. They found that the experimental Nusselt number increased with the Reynolds number. Furthermore, at a constant frontal velocity, the heat transfer coefficient increased with decreasing porosity.

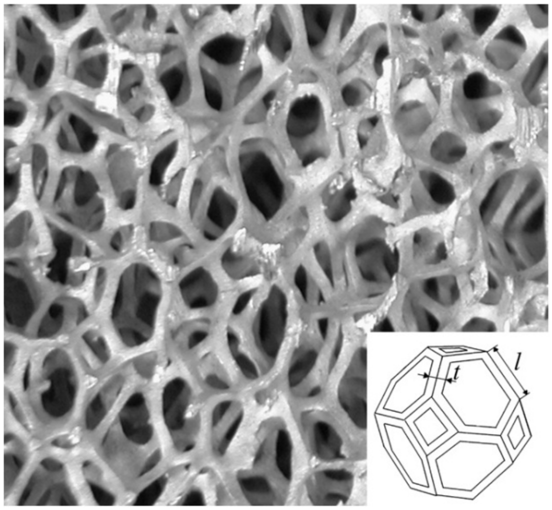

Figure 3.1: Metal foam sample

Hsieh *et al.* [3] carried out an experimental study to characterize the heat transfer behavior of several heat sinks made of aluminum metal foams (height 60 mm) with different porosity (0.87–0.96) and PPI (10–40). They experimentally analyzed the effect of porosity on heat transfer, and as part of their work measured the heat transfer performance of four samples with 20 PPI and differing porosities. The Nusselt number increased with an increase of the porosity. At constant porosity, they found that the heat transfer performance is better at higher PPI. The heat transfer coefficient increased with air velocity, increasing like $h \sim V^n$, with $0.38 \leq n \leq 0.46$. Kim *et al.* [4] measured the heat transfer coefficient in forced convection of air through aluminum foams. The authors reported experiments with six foams: foams with a porosity of ε=0.92 at 10, 20 and 40 PPI were used, and the other three foams had 20 PPI and varying porosity. The heat transfer coefficient was defined with reference to the overall heat transfer area (porous fins plus base area). The product of heat transfer coefficient times the surface efficiency, at constant Reynolds number, decreased as the PPI increased from 10 to 40, and it slightly decreased with decreasing porosity at fixed PPI (20 PPI). The heat transfer coefficient, based on the overall heat transfer area, increased with air velocity, following $h \sim V^n$, with n= 0.51. Kim *et al.* [5] analyzed the heat transfer characteristics of different FeCrAlY foams. The thermal performance of these metal foams was penalized by their low thermal conductivity.

Giani *et al.* [6] presented experimental interstitial heat transfer coefficients, measured for FeCr Alloy and Cu foams with 5.4, 5.6 and 12.8 PPI, by performing transient cooling experiments with air. Expressions to estimate the surface area and equivalent strut diameter and a simple correlation to compute the heat transfer coefficient were also presented. Their heat transfer coefficients, based on the overall heat transfer area, increased with air velocity raised to the power 0.43, for Darcy velocities between 1.2 and 5.7 m/s. Hwang *et al.* [7] measured interstitial convective heat transfer coefficients for air flowing in 10 PPI aluminum foams with porosities of 0.7, 0.8, 0.95, applying a transient single-blow technique. The heat transfer coefficient increased with air velocity ($h \sim V^{0.6}$ at ϵ= 0.95), and it increased with decreasing porosity.

Kim *et al.* [8] measured the heat transfer coefficient with air flowing in three aluminum foams with 10, 20, 40 PPI and a fixed porosity ε=0.92. The height of the specimen was 9.0 mm. The heat transfer coefficient increased with air Reynolds number raised to the power 0.426 and with the PPI. Younis and Viskanta [9] presented an experimental investigation to characterize the volumetric heat transfer coefficient between a heated air stream and ceramic foams (alumina and cordierite), using a transient single-blow technique. The heat transfer coefficient increased with air velocity, following $h \sim V^n$, with $0.42 \leq n \leq 0.96$: the exponent varied with pore diameter and material.

Incerra Garrido *et al.* [10] studied mass transfer with open-cell alumina foams with pore densities between 10 and 45 PPI and porosities between 0.75 and 0.85. The mass transfer coefficient increased with Reynolds number raised to the power 0.47. Dukhan and Chen [11] presented heat transfer measurements inside rectangular blocks of commercially available aluminum foam subjected to constant heat flux at one side, cooled by air. The temperature profile in the foam decayed exponentially with distance from the heated base. Kim *et al.* [12] explored the heat transfer characteristics of three porous copper foams (10 PPI, ϵ= 0.95; 20 PPI, ϵ = 0.95; and 20 PPI, ϵ = 0.92), soldered to a heated wall 10 mm wide and 37 mm long, placed in a 7 mm high channel with flows of water and FC-72. The results for water were in agreement with earlier work, using a dispersion conductivity coefficient of 0.06. However, a significant enhancement was found for FC-72, and for the highest porosity, the two-phase heat transfer coefficient reached 10 kW/(m^{2}K).

Noh *et al.* [13] measured the heat transfer coefficient referenced to the base area for water flowing in an annulus filled with aluminum foams (10 PPI, ϵ = 0.90). The heat transfer coefficient increased with Reynolds number raised to the power 0.4. Boomsma and Poulikakos [14] measured the hydraulic performance of compressed and uncompressed aluminum foams using water flowing with maximum frontal velocity (Darcy velocity) of 1.4 m/s. Boomsma *et al.* [15] also suggested a new numerical approach to model porous media as idealized units of eight cells. Moreover, Boomsma *et al.* [16] tested several different metal foam heat exchangers with liquid flows and they compared the results to the performance of several commercially available units. The porous heat exchangers presented thermal resistances lower than the conventional heat sinks while requiring the same pumping power. Boomsma and Poulikakos [17] investigated the effective thermal conductivity of three-dimensionally structured metal foam saturated with liquid.

Dai *et al.* [18] found that the model of Boomsma and Poulikakos contained errors in its development, but even when corrected, the model failed to provide accurate predictions of the effective thermal conductivity. Dai *et al.* reviewed the mechanistic basis of the Boomsma-Poulikakos model and provided an extension to the approach to account for ligament orientation. The new model provided much more accurate predictions of effective thermal conductivity. In an application study based on their prior work, Dai *et al.* [19] compared the heat transfer and pressure drop performance of metal-foam heat exchangers to another state-of-the-art heat exchanger. In the analysis, two heat exchangers were subjected to identical performance requirements, and the resulting volumes, masses, and costs were compared. The metal-foam heat exchanger could meet the performance of a louvered-fin heat exchanger with a smaller and lighter design; however, the cost of the metal-foam heat exchanger was much higher, owing to the cost of the metal foam.

Nawaz *et al.* [20] considered open-cell aluminum metal foam as a highly compact replacement for conventional fins in brazed aluminum heat exchangers. Heat transfer and pressure drop data were obtained from wind-tunnel experiments in order to make the comparisons. The target application was for air-cooling systems, and the authors demonstrated that metal foams have promise. They pointed out that bonding method can be important and suggested that contact resistance can be significant for constructions that are not brazed.

Mahjoob and Vafai [21] presented a review of correlations for the heat transfer coefficient available in the open literature. Ghosh [22] presented a theoretical analysis in order to compute interstitial heat transfer coefficients and foam-finned surface efficiency. Their approach was fairly simple and accounts for both the interstitial heat transfer coefficient and the foam-finned surface area efficiency. Moffat [23] showed that three parameters must be known to calculate the heat transfer performance of a foam-fin: the convective conductance per unit volume, the effective conductive conductance as a fin, and the effective thermal resistance between the foam and the surface to which it is attached. He developed a new test method, which, in conjunction with an older well established type of test, allows all three parameters to be measured using one specimen. Experimental heat transfer coefficients were measured during air flow for seven different aluminum open-cell foam samples with different pore density (PPI), porosity, and foam core height under a wide range of air velocity. Three imposed heat fluxes were considered for each foam sample: 25.0, 32.5 and 40.0 kW/m^2. The collected heat transfer data were analyzed to obtain the global heat transfer coefficient and normalized mean wall temperature. A model from the open literature was selected and compared to experimental data, and a new model for the global heat transfer coefficient and surface area efficiency was presented.

There are at least three levels of detail used in the design of heat exchangers: (1) Overall methods relying on effectiveness-NTU relations or a log-mean temperature difference (LMTD) approach. (2) Finite-volume modeling, in which the heat exchanger is discretized into smaller parts, often tube by tube or finer, typically with overall, average Nusselt numbers and friction factors adopted throughout the discretized geometry. (3) Full computational modeling of the governing equations in the flow and the solid material of the heat exchanger.

The overall methods are well accepted for heat exchanger design. In both the effectiveness-NTU and LMTD approaches an overall thermal conductance (UA) is used—the inverse of the total thermal resistance between the two streams. While relatively simple and commonly used with success in conventional heat exchangers, the methods neglect axial conduction in the heat exchanger, and when axial conduction becomes comparable to convection, these methods are not appropriate. For both metal and carbon foams, these effects may vitiate the accuracy of overall methods.

Finite volume methods, relying on overall averaged transport coefficients (or local values) can provide more accurate heat exchanger modeling, especially when axial conduction becomes important. The computational overhead can become expensive, and the relevant transport data and conduction models are only now becoming available for metal and carbon foams.

Highly detailed computations require detailed modeling of the geometry and sufficient resolution in the grid to resolve local conduction and convection (potentially including turbulence). The geometrical complexity of the foams, which has only recently been reported in sufficient detail to generate such models, probably makes these highly detailed computations dubious for routine design at the current time. However, this approach may become viable in the future, with an increased understanding of the foam geometry and properties, and further increases in computational power.

3.1.2 Heat transfer models

Calmidi and Mahajan [1] developed a model to compare the thermal performance of metal foam heat sinks. They defined a mean heat transfer coefficient, an average Nusselt number, and a Reynolds number as:

$$\bar{h} = \frac{q}{A_{base}(\bar{T}_{wall} - T_{air,in})} \tag{3.1}$$

$$Nu = \frac{\bar{h}L_h}{k_{eff}} \tag{3.2}$$

$$\mathrm{Re}_K = \frac{\bar{\rho}V\sqrt{K}}{\bar{\mu}} \tag{3.3}$$

with L_h the heated length of the base plate, k_{eff} the effective thermal conductivity of the sample, $\bar{T}_{wall}$ and $T_{air,in}$ the average temperature of the base plate and the inlet air temperature, respectively, and K (the permeability) obtained from pressure-drop data. Basing the heat transfer coefficient on the inlet temperature, rather than the mixing-cup temperature, and the base temperature without accounting for fin effects in the foam, introduces questions regarding the generality of the approach, because the heat transfer rate will affect the local mixing-cup and outlet air temperature and temperature distribution in the metal foam. However, Calmidi and Mahajan [1] state that for their experiments, “In all cases studied, the Nusselt number was found to be nearly independent of the input power.”

Jiang *et al.* [25] used a lumped capacitance approach. During the experiments, the solid matrix experienced a sudden change in thermal environment. The essence of the lumped capacitance method was the assumption that the temperature of the solid is spatially uniform at every instant in time. This assumption implies that temperature gradients within the solid are negligible compared to the temperature gradients in the fluid. The transient temperature response was determined by formulating an overall energy balance on the solid.

$$(\rho c \forall)_s \frac{dT_s}{dt} = -(hA)_{sf}(T_s - T_f) \tag{3.4}$$

By assuming the volume to surface area is related to the pore diameter as $(\forall_s / A_{sf}) = D_p / 6$,

$$h_{sf} = \frac{-(\rho c)_s D_p}{6(T_s - T_f)} \frac{dT_s}{dt} \tag{3.5}$$

Jiang and co-workers asserted that it was appropriate to use T_s and T_f as the inlet and outlet solid temperatures, respectively, and they justified this assumption by noting that the Biot number was very small (Bi < 0.0001 according to Jiang *et al.* [25]). However, this approach is open to questions of generality and perhaps validity, because it is patently inconsistent to assume the solid to be spatially isothermal and then use its inlet and outlet temperature difference as the driving potential for convection.

Using experimental data, Boomsma *et al.* [16] calculated the Nusselt number from

$$Nu = \frac{q}{A_{base}(T_{wall} - T_{coolant,in})} \frac{D_h}{k_{coolant}} \tag{3.6}$$

where A_{base} is the area of the base plate onto which the foam was soldered, D_h, is the conventional hydraulic diameter, $k_{coolant}$ is the thermal conductivity of the fluid flowing through the foam, and T_{wall} and $T_{coolant,in}$ are the base plate temperature and coolant inlet temperature, respectively. Using an energy balance on the coolant stream, Eq. (3.6) was rewritten as

$$Nu = \frac{\left[\dot{m} c_p (T_{out} - T_{in})\right]_{coolant}}{A_{base}(T_{wall} - T_{coolant,in})} \frac{D_h}{k_{coolant}} \tag{3.7}$$

The reference temperatures used by Boomsma *et al.* [16] are subject to questions of generality, but Boomsma *et al.* [16] and Calmidi and Mahajan [1] follow prior work in adopting this temperature difference. Boomsma *et al.* [16] state that this convention was followed to allow comparison to prior work; however, such a comparison is only justified if the experiments are conducted under identical conditions, as clearly mass flow rate, specific heat, and heat transfer rate affect the local mixing-cup temperature (and outlet temperature) of the flow. Obviously, their measured Nusselt numbers were zero for a zero coolant mass flow rate; their Nusselt numbers also increased monotonically with coolant mass flow rate (velocity).

Boomsma *et al.* [16] went on to cast their results in terms of the Colburn j factor and total air-side thermal resistance for comparison to other work. This approach is especially useful in comparing to conventional compact heat exchangers. Following the standard convention of Kays and London [24] (note the Stanton number is $St=Nu/(RePr)$):

$$j=\frac{Nu}{\mathrm{Re}\,\mathrm{Pr}^{1/3}} \tag{3.8}$$

If the same characteristic length is adopted in the Nusselt and Reynolds numbers, then Eq. (3.8) can be written as follows:

$$j=\frac{h}{(\rho c_p V)_{coolant}}\mathrm{Pr}^{2/3} \tag{3.9}$$

However, there may be cases, as in characterizing the pressure drop (see Chapter 2), where the conventional hydraulic diameter is used for the Reynolds number, but a differing length scale is used for the Nusselt number. In such a case, similar to the approach used in Chapter 2, an additional, as yet unspecified, length scale is introduced into the Colburn j factor:

$$j_{Lc}=\frac{h}{(\rho c_p V)_{coolant}}\frac{L_c}{D_h}\mathrm{Pr}^{2/3} \tag{3.10}$$

In the current work, heat transfer modeling is undertaken to account for fin-efficiency and local mixing-cup temperature effects. The total rate of heat transfer, q, is determined from an energy balance on each stream, and the modeling relies on an overall approach, as does all the prior work cited. Namely, for a metal foam heat exchanger operating under dry-surface conditions:

$$q=UA\cdot LTMD \tag{3.11}$$

where

$$LMTD=F\,\frac{(T_{air,in}-T_{coolant,out})-(T_{air,out}-T_{coolant,in})}{\ln\left(\dfrac{T_{air,in}-T_{coolant,out}}{T_{air,out}-T_{coolant,in}}\right)} \tag{3.12}$$

is determined from the measured temperatures, with the flow configuration factor, *F*, from Incropera and Dewitt [26]. The overall thermal conductance of the heat exchanger, *UA*, is formulated by neglecting the conduction resistance of the tube wall:

$$\frac{1}{UA}=\left(\frac{1}{\eta_o Ah}\right)_{air}+\left(\frac{1}{Ah}\right)_{coolant}+R_{bond} \tag{3.13}$$

The coolant-side convection coefficient is determined for the in-tube single-phase flow during the experiments, based on the geometry and flow, and there are no coolant-side fins (see Appendix C for details). The thermal contact resistance due to bonding the foam to the tubes, R_{bond}, was determined from ancillary experiments described later. The air-side fins are accounted for using the surface efficiency

$$\eta_o=1-\frac{A_{foam}\left(1-\eta_f\right)}{A_{foam}+\varepsilon A_{base}} \tag{3.14}$$

The surface area of the foam for air-side convection, A_{foam}, is determined from manufacturer's data for foam surface area per unit volume (see Chapter 2), using a volume of the base area, A_{base} times a fin height, L_f. The fin height, L_f, is taken as half the tube spacing. The fin efficiency is then calculated assuming a straight fin with an adiabatic tip, following Dai *et al.* [19]:

$$\eta_f=\frac{\tanh(m_{foam}L_f)}{m_{foam}L_f} \tag{3.15}$$

where the fin parameter accounts for the ligament and pore diameters, D_f and D_p, respectively

$$m_{foam}=\sqrt{3\pi D_f h/(D_p^2 k_{eff})} \tag{3.16}$$

and the effective thermal conductivity of the foam is taken as the solid-only effective thermal conductivity (see [18]):

$$k_{eff}=(1-\varepsilon)k_{solid}/2 \tag{3.17}$$

The data reduction scheme outlined in Eqs. (3.11)-(3.17) is described in more detailed in Appendix C, where the procedure for wet-surface conditions is also described. Accounting for the fin efficiency requires an iterative solution to the equation set.

3.2 Experimental results

Pressure drop and heat transfer rate are used to characterize the heat exchanger performance. These parameters determine the fan power required and size of the heat exchanger. Both pressure drop and thermal performances are affected by a number of parameters such as the geometry of heat exchanger, metal foam characteristics and flow conditions. Parametric analysis for the pressure drop is presented in Chapter 2. The results of the experiments conducted to analyze the thermal performance of metal foam heat exchangers are presented in this section. Total air side heat transfer rate, air side heat transfer coefficient and air side thermal resistance are presented against the face velocity for comparison purposes. The test conditions are specified in Table 3.1.

Table 3.1: Test conditions

Test condition	Coolant flow rate (kg/sec)	Inlet coolant temperature (^{0}C)	Inlet air temperature (^{0}C)	Inlet humidity (%)
Dry	0.082 ± 0.001	20 ± 3	34 ± 3	50
Wet	0.082 ± 0.001	8 ± 3	33 ± 5	60-90
Frost	0.132 ± 0.001	-12± 3	4 ± 2	70

The range is specified for each parameter in table. The associated uncertainties are specified in Appendix D.

3.2.1 Effect of porosity

Porosity is most important characteristic of metal foams. Larger porosity means smaller hindrance to the flow, so the pressure drop will be small, but the same time surface area per unit volume will be small. This results in smaller heat transfer rate as well. The effect of porosity is discussed for dry and wet conditions.

3.2.1.1 Dry condition experiments Heat transfer rate depends on the surface area of the metal foam. Larger heat transfer is possible if the surface area per unit volume is high. The effect of porosity (pore density in PPI) on the air-side heat transfer is presented in Figure 3.2. The 40 PPI foam showed the largest heat transfer rate under all face velocities due to having the highest surface area to volume ratio, while the 5 PPI foam had the smallest heat transfer rate. It is not only surface area which contributes to larger heat transfer rate. Small pore diameters imply more ligaments per unit volume, and more ligaments promote flow mixing.

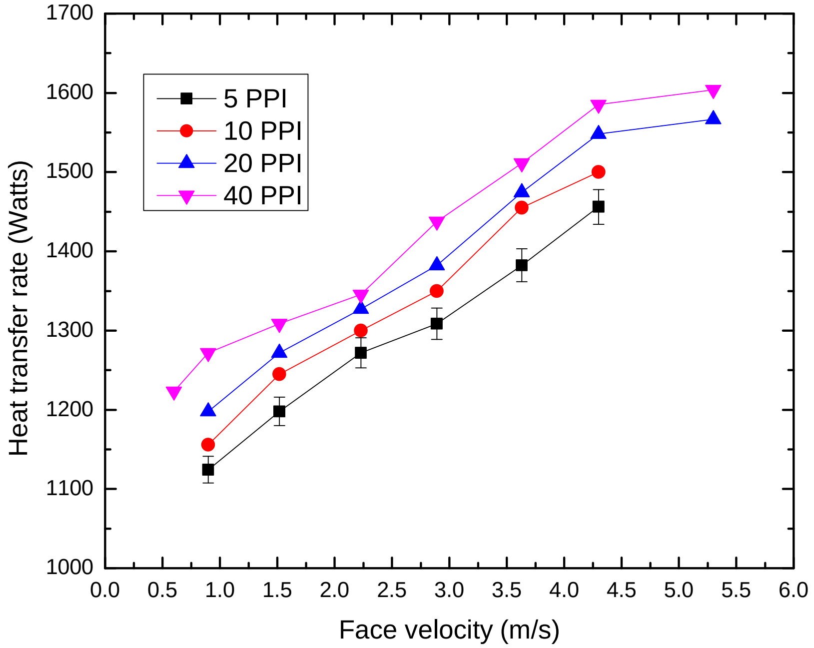

Figure 3.2: Air side heat transfer for foams of different porosities under dry conditions

The heat transfer coefficient based on the total surface area (base area and foam surface area) is presented in Figure 3.3. As the data were normalized based on the total air-side surface area, the effect of surface area per unit volume is accounted for. The heat transfer coefficient depends on the flow conditions. The heat transfer coefficient increases velocity with for all PPI foams at almost same rate. Heat transfer coefficient as high as 400 W/(m^{2}·K) can be achieved with a 40 PPI metal foam heat exchanger when the face velocity is about 6 m/s. This number is about twice the heat transfer coefficient achieved by compact louver-fin heat exchangers under same flow conditions.

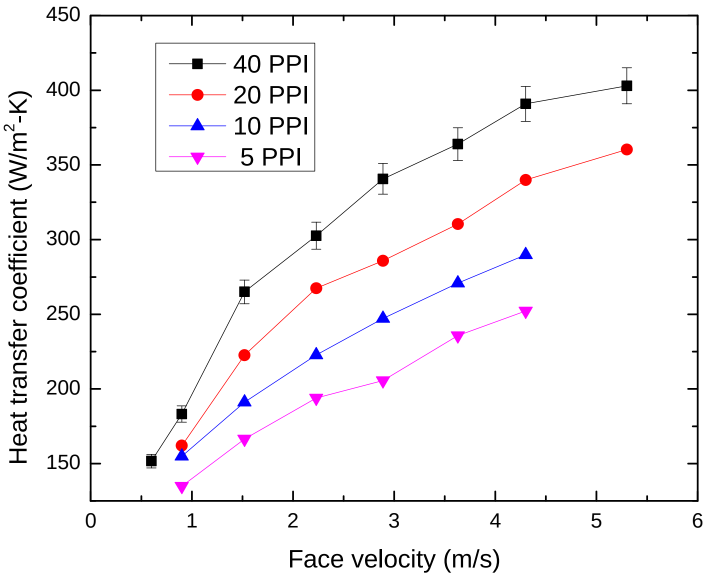

Figure 3.3: Air side heat transfer coefficient for foams of different porosities under dry conditions

3.2.1.2 Wet condition experiments When metal foam heat exchangers are tested under wet-surface conditions, both latent and sensible heat transfer are involved. Due to the low foam temperature moisture was continuously removed from the air flow. The resulting air-side heat transfer coefficients when the metal foam heat exchangers were tested conducted under wet conditions are presented in Figure 3.4. As in the dry-surface case, the foam with smaller pores (larger PPI) showed a heat transfer rate higher than the foam with larger pores. As the face velocity increased the heat transfer coefficient also increased. The rate of increase with face velocity for specific type of foam heat exchanger was relatively higher compared to the increase under dry conditions.

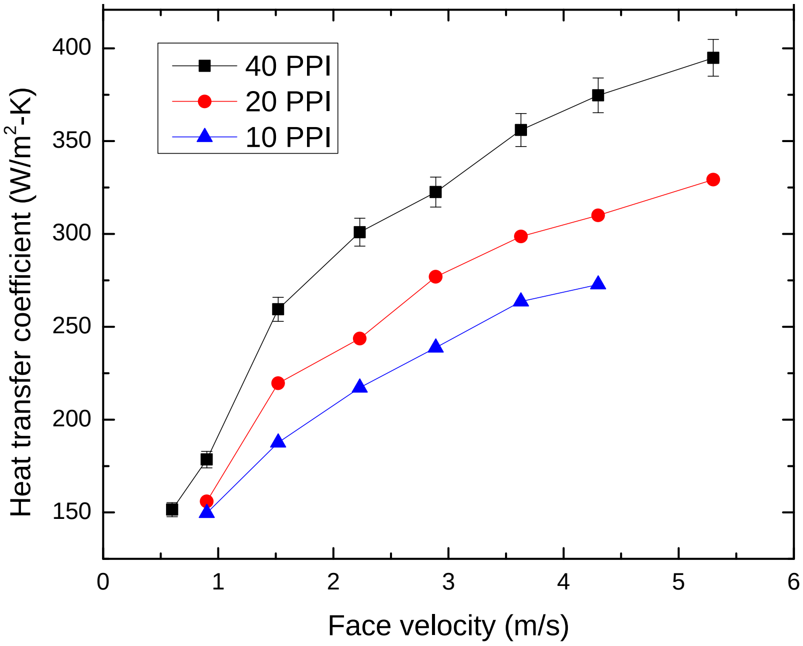

Figure 3.4: Air-side heat transfer coefficient for foams of different porosities under wet conditions

3.2.2 Effect of bonding method

Thermal performance of metal foam depends on the contact resistance between the base surface (flat tube or micro-channel tube) and the metal foam fins. The bonding technique can greatly affect the heat transfer rate. Generally, in order to avoid thermal contact resistance, fins are brazed to the tube surface. Brazing the metal foam to the base surface may be more difficult for foams compared that for other fins such as louvers, because the interface between the foam and the tube is not exactly planar. Three different bonding methods were used to join the metal foam between flat tubes or micro-channel tubes. Experiments were conducted with samples having same geometry but different joining methods. A comparison based on the total air side resistance is presented in Figure 3.5. Artic silver epoxy and thermal compound have thermal conductivity of 5 W/(m$^{2}\cdot$K) and 3.5 W/(m$^{2}\cdot$K), respectively. These results were used with Eq. (3.13) to determine R_{bond} for the Arctic silver epoxy and thermal compound. In this way, with R_{bond} from these ancillary experiments, and the tube-side resistance taken from well-established correlations, it was possible to isolate the air-side convective resistance.

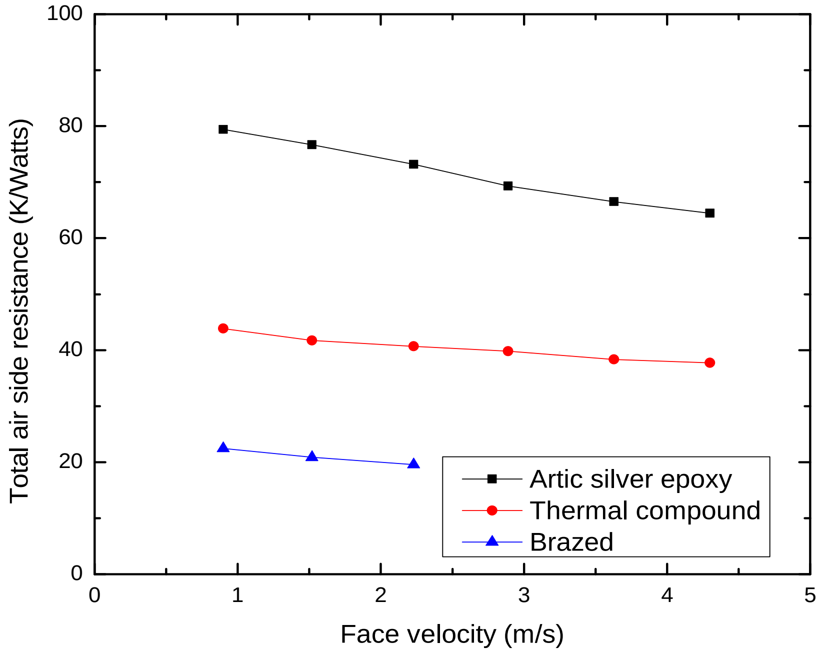

Figure 3.5: Total air-side resistance for different bonding methods

3.2.3 Effect of geometry

The geometry of the heat exchangers greatly affects the thermal performance. Frontal area, flow depth, and fin arrangement are important. The resulting pressure drop can be considerably reduced by proper design (Chapter 2).

In order to explore the effects of geometry on heat transfer, experiments were conducted using metal foam heat exchangers having same porosity. Sample 1 consisted of a continuous 10 PPI aluminum foam block through which round aluminum tubes passed, while sample 2 had round metal foam layers around the same number of round tubes. Both samples have same face area and flow depth as shown in Figure 3.6. The total air side heat transfer for both configurations is shown in Figure 3.7. Although sample 1 had a slightly larger heat transfer rate, the values do not differ much. In Chapter 2, it was shown that the pressure gradient for sample 1 was considerably larger than that for sample 2, under same operating conditions. Furthermore the weight of sample 2 was almost half of sample 1.

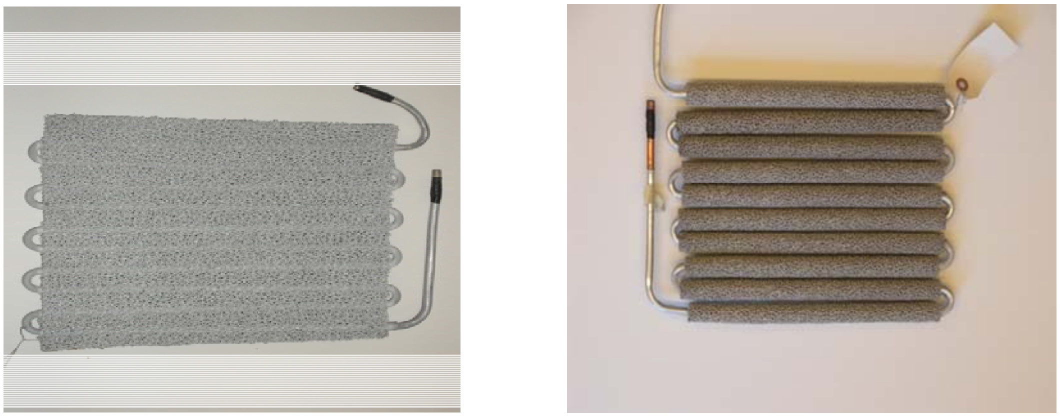

(a) (b)

Figure 3.6: Metal foam heat exchangers with different geometry

(a)Sample 1-continuous block structure (b) Sample 2-Annulur structure

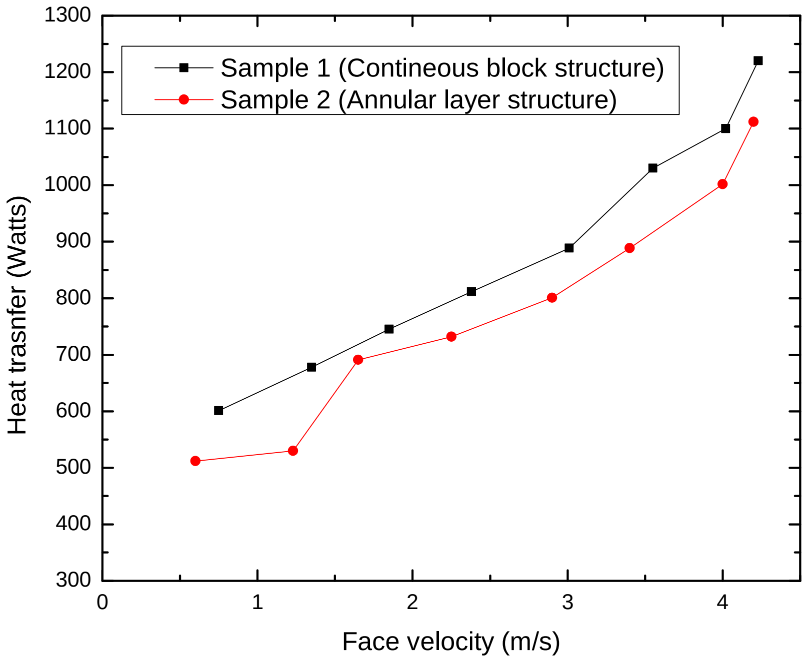

Figure 3.7: Heat transfer for samples with different geometry

3.2.4 Effect of base metal

The thermal conductivity of copper is larger than that of aluminum. If the base metal used to manufacture metal foam has larger thermal conductivity, the resulting heat transfer rate will be larger. In order to explore this effect, two samples of the same geometry with differing base metals were constructed (frontal area, flow depth, number of tubes, *etc*; see Figure 3.8). The thermal performance of two heat exchangers is compared in Fig. 3.9.

(Copper) *(Aluminum)*

Figure 3.8: Metal foam heat exchangers with different base material

Sample 1 had copper as the base metal for the metal foam, with copper tubes passing through annular fins. Sample 2 was manufactured from an aluminum alloy. Sample 1 showed much better performance, as the heat transfer rate was increased by almost 50%. For both samples the heat transfer rate increased as the face velocity increased, and the rate of increase was almost same. This behavior confirms that the only difference between the performances of two samples is due to the differences in thermal conductivity. The thermal hydraulic performance of copper foam heat exchanger is affected by the porosity and geometry in exactly the same way as for the aluminum foam.

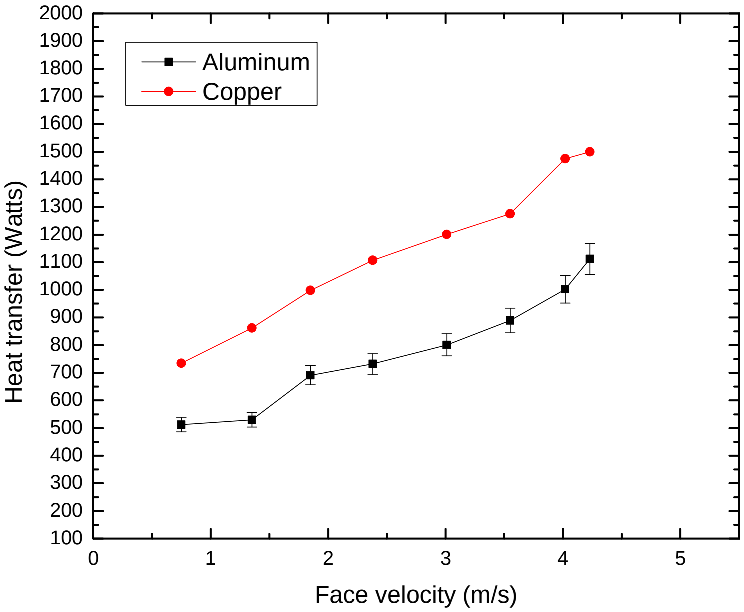

Figure 3.9: Heat transfer for samples with different base metal

3.2.5 Comparison to louver fins

The ultimate goal of designing a heat exchanger is to minimize cost, and thermal hydraulic performance is directly related to operating cost. A good heat exchanger should give the maximum heat transfer rate with the minimum pressure drop. Geometry, base metal and fin configuration all affect the performance. In order to evaluate metal foam heat exchanger performance for HVAC applications, a comparison to louvered-fin performance was undertaken. A state-of-the-art louvered fin design was adopted for the comparison; its characteristics are described in Table 3.2 (Park and Jacobi, Sample 1 [27]). The comparison considers a10 PPI aluminum metal foam as a “drop-in” replacement for the louvered fins. Obviously, this deployment of metal foam is not expected to be optimal; however, this approach allows a comparison with as few other design changes as possible. The performance of the metal foam heat exchanger is compared to the louver fin heat exchanger in Figure 3.11. Under all flow conditions the metal foam heat exchangers performed much better than did the louver-fin configuration. Such a comparison confirms that metal foam can replace conventional materials for HVAC&R heat transfer applications, if the cost of the metal foam is acceptable. Further comparisons are provided in Appendix G.

Table 3.2: Characteristics of louver fin

L_p (mm)	F_p (mm)	F_l (mm)	L_l (mm)	α (deg)	F_d (mm)	T_p (mm)	δ_f (mm)
1.38	1.4	12.43	11.15	44	25.4	14.26	0.24

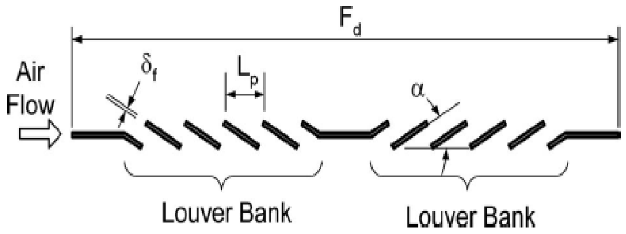

Figure 3.10: Comparison of metal foam and louver-fin heat exchangers

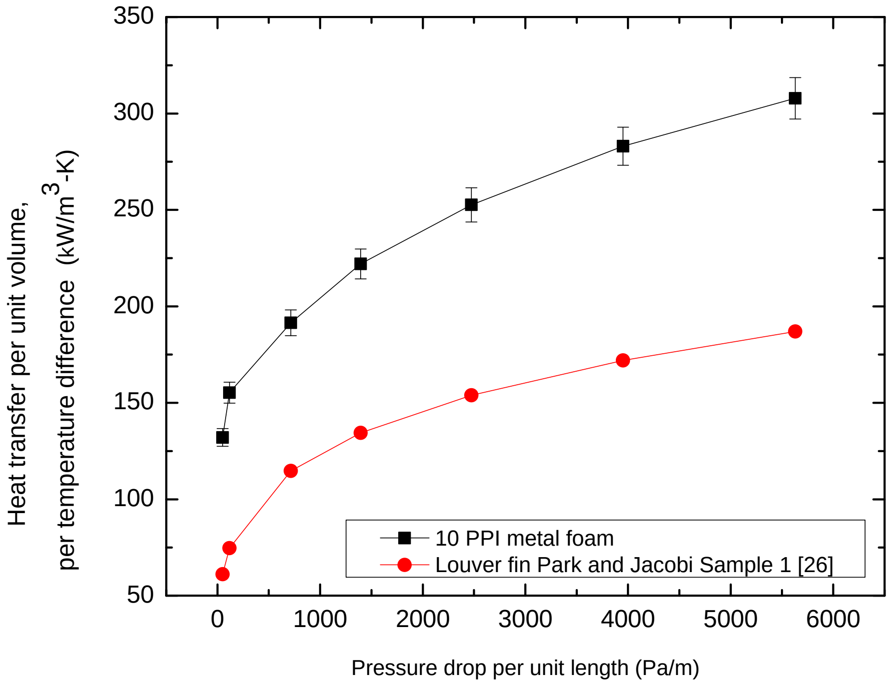

Figure 3.11: Thermal-hydraulic performance comparison of metal foam and louver-fin heat exchangers

3.2.6 Comparison to wire mesh

As described in Chapter 2, wire meshes are regular porous media with a well-organized structure. In comparison to wire mesh, metal foams have a more complex porous structure. Although both media have large surface area per unit volume, which is good for larger heat transfer performance, the more complex structure in metal foams enhances the heat transfer by more effectively promoting mixing. However, metal foams also have a larger pressure drop (Chapter 2). The heat transfer coefficient based on surface area for a metal foam heat exchanger (10 PPI aluminum) is compared to that of a wire mesh sample (steel, L_c=3 mm) in Figure 3.12. Both samples had the same frontal area and flow depth (Figure 3.13). The metal foam heat exchanger performed better compared to the wire mesh sample. It can be contributed partially, to the larger thermal conductivity of aluminum compared to steel, but the larger increase in heat transfer performance was also due to the tortuous structure of metal foam, resulting in a higher heat transfer coefficient.

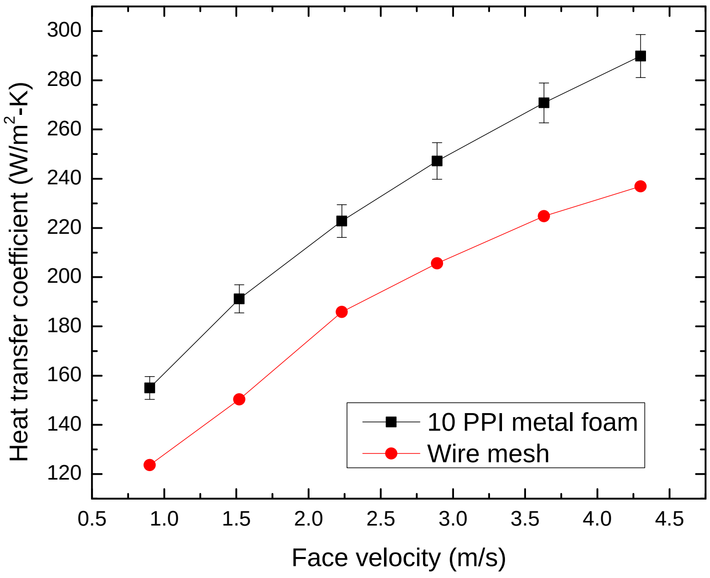

Figure 3.12: Heat transfer performance regular vs. irregular media

(a) *(b)*

Figure 3.13: Regular vs. irregular porous media (a) wire mesh (b) 10 PPI metal foam

3.2.7 Heat transfer performance under frosted conditions

When the flow conditions are humid and the coolant flowing through the tubes is below freezing, frost can grow on the air-side of heat exchanger. In order to analyze the performance of metal foam heat exchangers under such conditions, experiments were conducted under frosting conditions. The total heat transfer rate as a function of time for two face velocity conditions is presented in Figure 3.14. Under both flow conditions, the heat transfer rate decreased initially, due to growth of frost on fin surface. After some time the frost growth rate decreased and the heat transfer rate became almost constant. A larger face velocity resulted in larger pressure drop (Chapter 2), but the steady-state heat transfer performance was almost the same. Images of frost formation after 60 minutes at a face velocity of 0.8 m/s are presented in Figure 3.15.

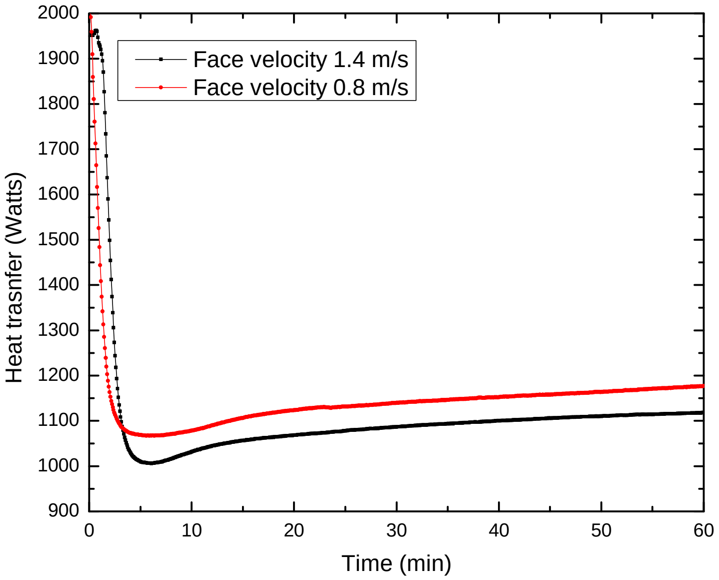

Figure 3.14: Heat transfer performance under frosted conditions

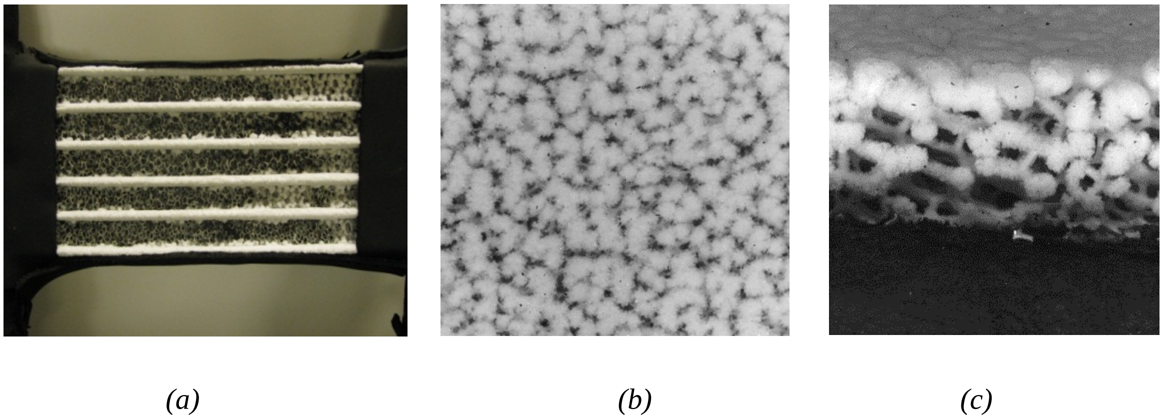
(a) (b) (c)

Figure 3.15: Frost growth on 10 PPI metal foam heat exchanger: (a) 0.8 m/s face velocity, (b) under natural convection – top view, (c) under natural convection – side view

A visual study of the frost formation was conducted for natural convection for comparison, and sample results are also presented in Figure 3.15. The frost structure appeared granular and no ligament layering was observed. The structure of the frost varied somewhat for different porosities, and further images are provided in Appendix H.

3.3 Modeling the heat transfer performance

Many researchers have tried to quantitatively describe thermal performance for metal foams. The conventional approach is based on a model developed by considering the flow through metal foam as a flow through an array of cylinders. An alternative approach is to analyze the results empirically. In this approach, the data are reduced based on the hydraulic diameter of the specimen.

3.3.1 Comparison to heat transfer model

There are numerous models available in literature to predict the heat transfer performance for flow through porous media. Equation (3.12) was developed by Calmidi [1] to predict the heat transfer coefficient based on the foam properties such as permeability, ligament diameter, *etc*.

$$h = \left(\frac{k_{fluid}}{D_f} \right) 0.52 \, \mathrm{Re}_{Df}^{0.5} \, \mathrm{Pr}^{0.37} \tag{3.18}$$

The ligament diameter, D_f, is considered as the characteristic length, and k_{fluid} is the fluid thermal conductivity. Experimental results are compared to values predicted by this relationship for a 40 PPI metal foam sample in Figure 3.16. Although the model is widely used to predict the heat transfer coefficient for foams, it does not provide accurate predictions of the current data. A possible source of error is a flaw in the assumed geometry: the model considered metal foam ligaments as stack of small cylinders, either in cross-flow or parallel-flow orientation. This is not the case in reality (see Figure 3.17).

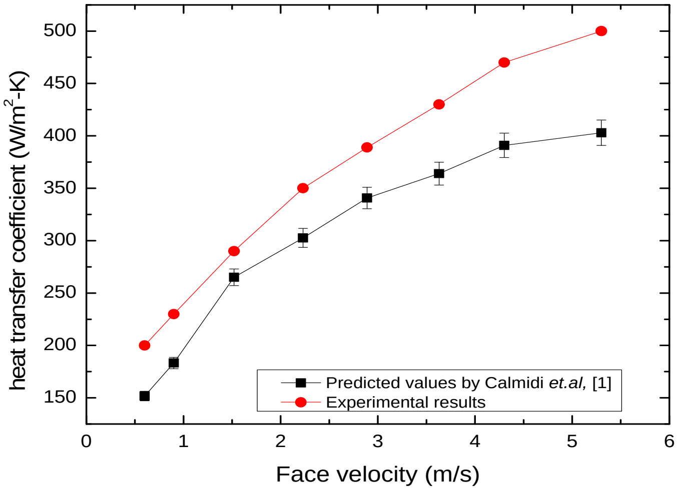

Figure 3.16: Comparison of experimental and predicted results

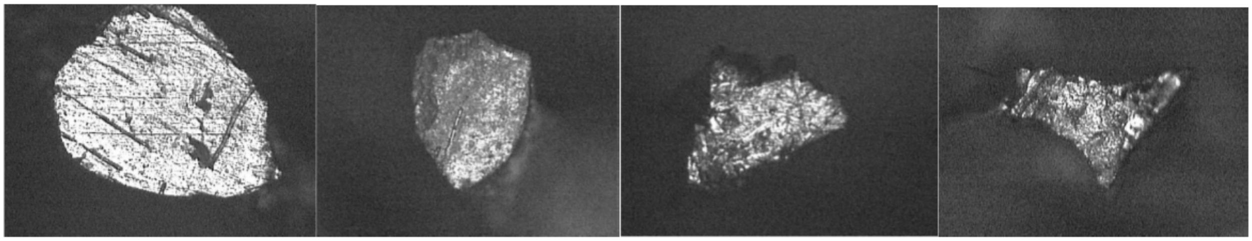

(a) $\varepsilon = 90.95$ % *(b)*$\varepsilon = 92.01$ % *(c)* $\varepsilon = 93.48$ % *(d)* $\varepsilon = 97.85$ %

Figure 3.17: Metal foam ligament cross sectional view for different porosities [28]

3.3.2 Identification of parameters (Buckingham Pi terms)

Experimental data show that geometrical characteristics of foams and test specimen, flow conditions, and the physical properties are related to the pressure-drop performance of metal foam heat exchangers. In this section key parameters are listed, and an application of the Buckingham Pi theorem is undertaken to determine the set of non-dimensional numbers to represent the data. The key parameters are:

- *Physical properties of fluid:* density, viscosity
- *Flow parameters:* pressure, face velocity
- *Geometric parameters:* flow depth, pore diameter, ligament diameter

For a fully developed flow, with fluid properties related to temperature and pressure in an appropriate way, we expect

$$h = fncn(\rho, \mu, k, c_p, D_f, D_p, V) \tag{3.19}$$

As a matter of convention, the hydraulic diameter is anticipated to account for geometrical parameters. Under such an assumption, effectively

$$h = fncn(\rho, \mu, k, c_p, D_h, V) \tag{3.20}$$

Eq. (3.20) is written in order to follow convention; however, it must be recognized that the geometric complexity of the metal foams implies at least one additional length scale may appear. Proceeding in an *ad hoc* way, one such characteristic length, L_c, yet to be determined, is introduced back into the Buckingham-Pi analysis. This admittedly *ad hoc* approach then yields:

$$Nu_{Lc} = \frac{hL_c}{\bar{k}} \tag{3.21}$$

and

$$\mathrm{Re}_{Dh} = \frac{\bar{\rho} V D_h}{\bar{\mu}}; \qquad \mathrm{Pr} = \frac{\bar{c}_p \bar{\mu}}{\bar{k}} \tag{3.22}$$

with

$$Nu = fncn(\mathrm{Re}_{Dh}, \mathrm{Pr}, L_c / D_h) \tag{3.23}$$

Following Kays and London, this result is written in terms of the Colburn *j* factor,

$$j_{Lc} = \frac{Nu_{Lc}}{\mathrm{Re}_{Dh}\,\mathrm{Pr}^{1/3}} = \frac{h}{\overline{\rho c}_p V}\frac{L_c}{D_h}\mathrm{Pr}^{2/3} \tag{3.24}$$

with

$$\mathrm{Re}_{Dh} = \frac{\overline{\rho} V D_h}{\overline{\mu}}; \qquad \mathrm{Pr} = \frac{\overline{c}_p \overline{\mu}}{\overline{k}} \tag{3.25}$$

Since only one fluid is used (air), but with an expectation of generality, except for $Pr \ll 1$.

$$j_{Lc} = fncn(\mathrm{Re}_{Dh}, L_c / D_h) \tag{3.26}$$

Note that if $L_c=D_h$, Eqs (3.24)-(3.26) take the conventional form, and $j=fncn(\mathrm{Re})$ alone.

3.3.3 Data reduction for determination of *j* factor

In order to facilitate comparison to conventional compact heat exchangers, the Colburn *j* factor, with $L_c=D_h$, is presented in Figure 3.18. As shown in the figure, foams with higher pore density (PPI) had higher *j* factors. In comparison to most convention heat exchangers (e.g., louvers), metal foams have a high Colburn *j* factor. Attempting to fit the data in this format only to Re_{Dh} results in fits with a relative RMS deviation of more than ±10%; however, when pore diameter, D_p, is used as an additional characteristic length, the following fit predicts all dry-foam heat transfer data with a relative RMS deviation of 4%:

$$j_{Dp} = \frac{h}{\overline{\rho c}_p V}\frac{D_p}{D_h}\mathrm{Pr}^{2/3} = 2\,\mathrm{Re}_{Dh}^{-0.5611}\left(D_p/D_h\right)^{0.3213} \tag{3.27}$$

The predicted and measured Colburn *j* factors are presented in Figure 3.19.

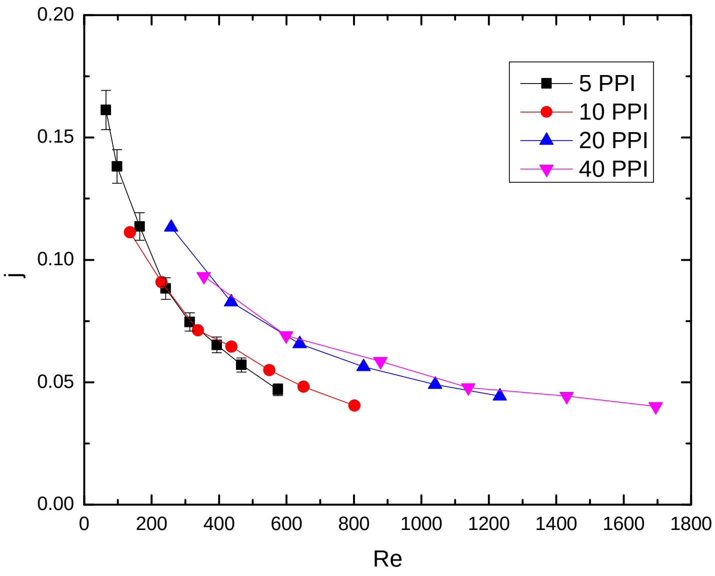

Figure 3. 18: Colburn j factor for metal foam plotted against Reynolds number (all based on hydraulic diameter).

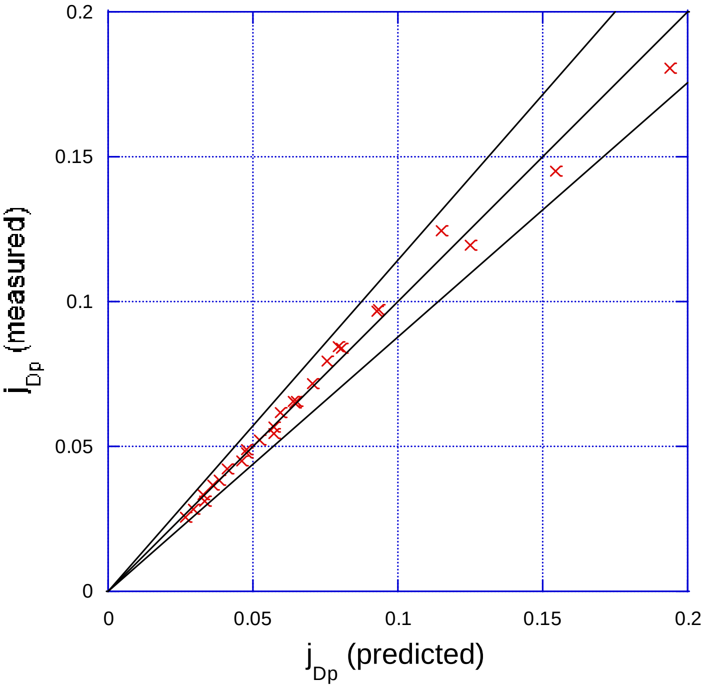

Figure 3.19: Colburn j factor with pore diameter as a characteristic length, measured versus predicted (Eq. 3.27). The relative RMS deviation is ±4%; limits of ±12.5% are shown in the plot.

3.4 Conclusions

Metal foam heat exchangers were tested for the thermal performance. The metal foams had higher heat transfer rates than did conventional louvered-fin heat exchangers. The results were explained in terms of the complex structure of the metal foams. Porosity is an important parameter, directly affecting the heat transfer rate under both dry and wet conditions. Geometry and the base material of metal foam also played important roles. Under frosting conditions, the heat transfer rate decreased initially, and then it became almost constant. A larger heat transfer for metal foams compared to wire mesh emphasized the importance of the complex structure of metal foams. The thermal-hydraulic performance of metal foam heat exchangers was better than the louver-fin heat exchanger for geometrically similar samples. There are various models available to predict the heat transfer coefficient, but they are based on non-realistic geometries, and they failed to predict the performance accurately. Using the hydraulic diameter of the heat exchanger as a length scale, the Colburn j factor was presented as a function of the Reynolds number.

3.5 References

[1] Calmidi, V.V., and Mahajan, R.L. “Forced convection in high porosity metal foams,” *ASME Journal of Heat Transfer,* Vol. 122, pp. 557–565, 2000.

[2] Calmidi, V.V. “Transport phenomena in high porosity fibrous metal foams,” *Ph.D. Thesis*, University of Colorado, Boulder, Colorado, USA, 1998.

[3] Hsieh, W.H., Wu, J.Y., Shih, W.H., and Chiu, W.C. “Experimental investigation of heat transfer characteristics of aluminum-foam heat sink,” *International Journal of Heat and Mass Transfer,* Vol. 47, pp. 5149–5157, 2004.

[4] Kim, S.Y., Paek, J.W., and Kang, B.H. ”Flow and heat transfer correlations for porous fin in plate-fin heat exchanger,” *ASME Journal of Heat Transfer,* Vol. 122, pp. 572–578, 2000.

[5] Kim, T., Fuller, A.J., Hodson, H.P., and Lu, T.J. “An experimental study on thermal transport in lightweight metal foams at high Reynolds numbers,” *Proceedings of International Symposium of Compact Heat Exchangers, Grenoble, France,* pp. 227–232, 2002.

[6] Giani, L., Groppi, G., and Tronconi, E. “Heat transfer characterization of metallic foams,” *Industrial Chemical Engineering,* Vol. 44, pp. 9078–9085, 2005.

[7] Hwang, J.J., Hwang, J.G., Yeh, R.H., and Chao, C.H. “Measurement of interstitial convective heat transfer and frictional drag for flow across metal foams,” *ASME Journal of Heat Transfer,* Vol. 124, pp. 120–129, 2002.

[8] Kim, S.Y., Kang, B.H., and Kim, J.H. “Forced convection from aluminum foam materials in an asymmetrically heated channel,” *International Journal of Heat and Mass Transfer,* Vol. 44, pp. 1451–1454, 2001.

[9] Younis, L.B., and Viskanta, R. "Experimental determination of the volumetric heat transfer coefficient between stream of air and ceramic foam," *International Journal of Heat and Mass Transfer,* Vol. 36, pp. 1425–1434, 1993.

[10] Incerra Garrido, G., Patcas, F.C., Lang, S., and Kraushaar-Czarnetzki, B. "Mass transfer and pressure drop in ceramic foams: a description for different pore sizes and porosities," *Chemical Engineering Science,* Vol. 63, pp. 5202–5217. 2008.

[11] Dukhan, N., and Chen, K.C. "Heat transfer measurements in metal foam subjected to constant heat flux," *Experimental Thermal Fluid Science,* Vol. 32, pp. 624–631, 2007.

[12] Kim, D.W., Bar-Cohen, A., and Han, B. "Forced convection and flow boiling of dielectric liquid in a foam-filled channel," *Thermal and Thermomechanical Phenomena in Electronic Systems, 2008, ITHERM 2008,* Orlando, FL, pp. 86-94, 2008.

[13] Noh, J.S., Lee, K.B., and Lee, C.G. "Pressure loss and forced convective heat transfer in an annulus filled with aluminum foam," *International Communications in Heat Mass Transfer,* Vol. 33, pp. 434–444, 2006.

[14] Boomsma, K., and Poulikakos, D. "The effects of compression and pore size variations on the liquid flow characteristics of metal foams," *ASME Journal of Fluids Engineering,* Vol.124 pp. 263–272, 2002.

[15] Boomsma, K., Poulikakos, D., and Ventikos, Y. "Simulations of flow through open cell metal foams using an idealized periodic cell structure," *International Journal of Heat and Fluid Flow,* Vol. 24, pp. 825–834, 2003.

[16] Boomsma, K., Poulikakos, D., and Zwick, F. "Metal foams as compact high performance heat exchangers," *Mechanics of Materials,* Vol. 35, pp. 1161–1176. 2003.

[17] Boomsma, K., and Poulikakos, D. "On the effective thermal conductivity of a three dimensionally structured fluid-saturated metal foam," *International Journal of Heat and Mass Transfer,* Vol. 44, pp. 827–836, 2001.

[18] Dai, Z., Nawaz, K., Bock, J., and Jacobi, A.M. "Correcting and extending the Boomsma-Poulikakos effective thermal conductivity model for three-dimensional, fluid-saturated metal foams," *International Communications in Heat and Mass Transfer*, 37(6): 575-580, 2010.

[19] Dai, Z., Nawaz, K., Park, Y., Qi, C. and Jacobi, A.M. "A comparison of metal-foam heat exchangers to compact multi-louver designs for air-side heat transfer applications," *Heat Transfer Engineering,* Vol. 33, pp. 21-30*,* 2012.

[20] Nawaz, K., Bock, J., and Jacobi, A.M. "Experimental studies to evaluate the use of metal foams in highly compact air-cooling heat exchangers," *13th International Refrigeration and Air Conditioning Conference, July 12th- 16th, Purdue University Lafayette, IN, 2010.*

[21] Mahjoob, S., and Vafai, K. "A synthesis of fluid and thermal transport models for metal foam heat exchangers," *International Journal of Heat and Mass Transfer,* Vol. 51, pp. 3701–3711, 2008.

[22] Ghosh,I. "Heat transfer correlation for high porosity open-cell foam," *International Journal of Heat and Mass Transfer,* Vol. 52*,* pp. 1488–1494, 2009.

[23] Moofat, R.J. Eaton, J.K., and Onstad, A. "A method for determining the heat transfer properties of foam-fins," *ASME Journal of Heat Transfer*, Vol. 13.1, 2009.

[24] Kays, W.M., and London, A.L. *Compact Heat Exchangers*, *2nd ed.*, McGraw-Hill, New York, 1964.

[25] Jiang, P., Xu, R., and Gong, W. "Particle-to-fluid heat transfer coefficients in miniporous media,*"* *Chemical Engineering Science,* Vol. 61, pp. 7213-7222, 2006.

[26] Incropera, F.P., and DeWitt, D. P., *Fundamentals of heat and mass transfer, 4th ed*., John Wiley & Sons, Inc, 1996

[27] Park, Y. and Jacobi, A.M. “Air-side heat transfer and friction correlations for flat-tube, louver-fin heat exchangers,” *ASME Journal of Heat Transfer,* Vol. 131(2), 2009.

[28] Bhattacharya, A., Calmidi, V.V., and Mahajan, R.L. “Thermophysical properties of high porosity metal foams,” *International Journal of Heat and Mass Transfer*, Vol. 45, pp. 1017–1031, 2002.

Chapter 4 — Summary and conclusions

4.1 Overview

Heat exchangers are critical components in heating and cooling systems for human comfort, electronics cooling, food preservation, pharmaceuticals, and other applications, and because these systems represent a significant part of our end-use energy consumption, improvements in heat exchanger performance can result in significant energy savings. The fin-and-tube construction, using copper and aluminum, is the most common design used in these cooling and heating applications. Through earlier work on this project (*Phase I*), we submitted a report providing a comprehensive literature review and analysis, through which we identified new materials that hold promise for use in heat exchangers. We assessed the potential benefits and feasibility of using a wide range of materials, in order to identify those with promise for heat exchanger designs. Our critical evaluation produced a compilation of performance data, physical/chemical properties, and other characteristics. The report also identified current gaps in our knowledge and impediments to using these materials for heat exchangers. Two main outcomes of that earlier work were: (1) porous materials, in particular metal and carbonaceous foams, were identified as materials with potential for use in heat exchangers; (2) the primary technical barrier to the application of these new materials was identified as a lack of heat transfer and pressure drop performance data. The current study, (*Phase II*), was undertaken in order to provide performance data necessary for a more complete design and analysis of metal and carbonaceous foams as heat exchanger materials.

Although an exhaustive review of the literature was completed in *Phase I*, new information is constantly becoming available. In this *Phase II* report, we have updated the literature review with a special focus on the structure of metal foams in Chapter 1, an updated review of pressure-drop performance is presented in Chapter 2, and an updated review of heat transfer performance in presented in Chapter 3. Ancillary reviews of the thermal conductivity of metal foams and their performance as compared to conventional fins are provided in Appendix F and G, respectively.

4.2 Foam structure and water retention

An effort to understand and quantify the geometry of metal foams is presented in Chapter 1. A literature review shows that the Kelvin tetrakaidecahedron unit-cell geometry was almost universally adopted for metal foam modeling; however, the Weaire-Phelan (WP) unit cell geometry is known to possess a lower Gibbs energy. Both the Kelvin model and the WP unit cell are developed by assuming the foam reaches its equilibrium geometry, but metal foams are not equilibrium structures. X-ray micro-computed tomography (μCT) results show that neither the Kelvin cell nor the WP cell is in excellent agreement with the real foam geometry, but the WP cell is a more realist representation of the metal foam geometry.

The experimental results from μCT are also used to give basic geometric information such as ligament length, orientation, and diameter. For the 5 PPI aluminum foam, the average ligament length was about 1.9 mm, and the average diameter was 0.60 mm. For the 10 PPI foam, the average length and diameter were 1.5 mm and 0.46 mm, respectively; for the 20 PPI foam the average length and diameter were 1.1 mm and 0.42 mm, respectively. More comprehensive data from a larger set of metal foams used in water retention studies are provided in Table 4.1. Geometric data such as these were used to better understand water retention in the foam and in developing pressure-drop and heat transfer correlations.

Table 4.1: Characteristics of metal foam samples

PPI	Porosity	d_f *(mm)*	d_P *(mm)*
5	0.953	0.50	4.02
10	0.942	0.40	3.13
20	0.933	0.30	2.70
40	0.927	0.25	2.02
45	0.913	0.20	2.00

The 45 PPI foam shows almost no water drainage in a dynamic dip test, but the 10 PPI foam shows significant drainage, holding less than half the water held by the 45 PPI specimens. Foam porosity has a very significant effect on drainage behavior. Foam surface condition has much

less effect on drainage, and the effect is counter intuitive. After Boehmite treatment to increase wettability, the 10 PPI foam held about 20% more water than without treatment.

Strategies to improve water drainage were explored, and it was found that creating a composite structure, with foams of differing porosity could be very effective. Composite foam with 40 PPI and 10 PPI manifested a drainage behavior typical to that of 10 PPI foam alone. Moreover, a screening comparison of drainage behavior showed the 10 PPI sample to hold less water than a typical louvered fin.

4.3 Heat transfer and pressure drop

Heat transfer and pressure drop behavior are key to the design of heat exchangers, and one of the most important contributions of the current work is a set of fairly general, accurate curve fits for predicting the friction factor and Colburn *j* factor for metal foams. The curve fits are based on data from wind tunnel experiments with foams of 5, 10, 20, and 40 PPI. The experiments were conducted with an air flow, for inlet temperatures ranging from about 4^{o}C to 35^{o}C, inlet relative humidity from about 50% to 90%, and face velocities ranging from 0.5 m/s to 6 m/s.

The friction factor fit is repeated here as Eq. (4.1). The data had a relative RMS deviation of ±14.86% from the fit, and the experimental uncertainty in *f* was estimated to be about ±7%. The uncertainty in Re was about ±4%.

$$f_{D_p} = \frac{\Delta P}{L}\frac{\bar{\rho}}{G^2}\frac{D_p}{2} = 1.975\,\mathrm{Re}_{D_h}^{-0.1672}\left(D_p/D_h\right)^{-3.708} \tag{4.1}$$

In Eq. (4.1), ΔP is the pressure drop across the foam (P_i-P_o), L is the flow length (from inlet to exit face of the metal foam), and G is the mass flux, $G=\bar{\rho}V_{\max}$, where V_{max} is frontal velocity divided by the porosity, V_{fr}/ε, and $\bar{\rho}$ is the mean of the inlet and exit density. D_p is the pore diameter of the foam. The Reynolds number, Re_{D_h}, is based on the average of the viscosity at the inlet and exit face, the maximum velocity, V_{max}, and the conventional hydraulic diameter for a compact heat exchanger; *i.e.*, $\mathrm{Re}_{D_h} = \bar{\rho} V_{\max} D_h / \bar{\mu}$, and $D_h=4\varepsilon A_{fr}/A_T$. The total wetted area A_T includes the foam surface area and the exposed area of the tubes.

The Colburn *j* factor data were also fit to a curve using multiple length scales. The fit is repeated as Eq. (4.2), and it predicts all dry-foam heat transfer data with a relative RMS deviation of 4%. The uncertainty in the *j* factor was estimated to be about ±8% for all the data, and the uncertainty in Re was about ±4%,

$$j_{Dp} = \frac{h}{\bar{\rho} \bar{c}_p V_{\max}} \frac{D_p}{D_h} \mathrm{Pr}^{2/3} = 2\,\mathrm{Re}_{Dh}^{-0.5611} \left(D_p / D_h \right)^{0.3213} \tag{4.2}$$

In Eq (4.2), all thermophysical properties were evaluated as the mean of the inlet and exit values. The heat transfer coefficient, *h*, was calculated by determining the thermal resistance due to air-side convection alone, and accounting for fin efficiency as detailed in Chapter 3. In general, the fin efficiency ranged from 0.85 to 0.90; thus, for designs similar to those of the current work, reasonable estimates of performance can be obtained by estimating the fin efficiency to be 0.88.

Under wet-surface conditions, the pressure drop for the 10 PPI foam increased from 0 to about 25% and the heat transfer coefficient increases by roughly 100%. Under frosted-surface conditions, foam heat transfer performance drops precipitously and rapidly. These findings, along with the enhanced drainage compared to a louvered fin, imply that metal-foam heat exchangers might be particularly attractive for dehumidifying applications. However, even under dry-surface conditions the heat transfer per unit volume, per unit temperature difference for the 10 PPI foam is almost twice that of a state-of-the-art louver fin, with the same pressure gradient.

Appendix A: Sample manufacturing

Metal foam heat exchanger were build in different confrigurations. In total 16 heat exchnagers were tested in a closed loop-wind tunnels for the thermal-hydraulic performacne analysis. The design of samples along with the detailed specifications are described in this section.

Figure A.1: Flat tube configuration

Table A.1: Design specifications

Sample	1-3
Base metal	Al 6061 alloy
Porosity	10 PP
Tube side configuration	Flat tube
Number of fins	10
Fin depth	15 mm
Fin thickness	15 mm
Bonding method	Artic silver, thermal compound
Face area	200 mm×174 mm
Tube width	25.4 mm
Tube wall thickness	0.5 mm

Figure A.2: Flat micro channel tube configuration

Table A.2: Design specification

Sample	4-7
Base metal	Al 6061 alloy
Porosity	5 PPI,10 PPI,20 PPI, 40 PPI
Tube side configuration	Flat tube micro channel
Number of fins	10
Fin depth	15 mm
Fin thickness	15 mm
Face area	200 mm×174 mm
Bonding method	Artic silver, thermal compound
Tube width	25.4
Channel area	14.96 mm^2
Number of channel	8

Figure A.3: Round copper tube annular configuration

Table A.3: Design specification

Sample	8
Porosity	10 PPI
Base metal	Copper alloy
Tube side configuration	Round tube
Bonding method	brazed
Face area	200 mm×150 mm
Tube diameter	10 mm
Tube thickness	0.5 mm
Fin thickness	10 mm
Number of tubes passes	10

Figure A.4: Round aluminum tube annular configuration

Table A.4: Design specification

Sample	9
Porosity	10 PPI
Base metal	Aluminum
Tube side configuration	Round tube
Bonding method	brazed
Face area	200 mm×150 mm
Tube diameter	10 mm
Tube thickness	0.5 mm
Fin thickness	10 mm
Number of tubes passes	10

Figure A.5: Round copper tube continuous block configuration

Table A.5: Design specification

Sample	10
Porosity	10 PPI
Base metal	Aluminum
Tube side configuration	Round tube
Bonding method	brazed
Face area	200 mm×150 mm (continuous block)
Tube diameter	10 mm
Tube thickness	0.5 mm
Number of tubes passes	10

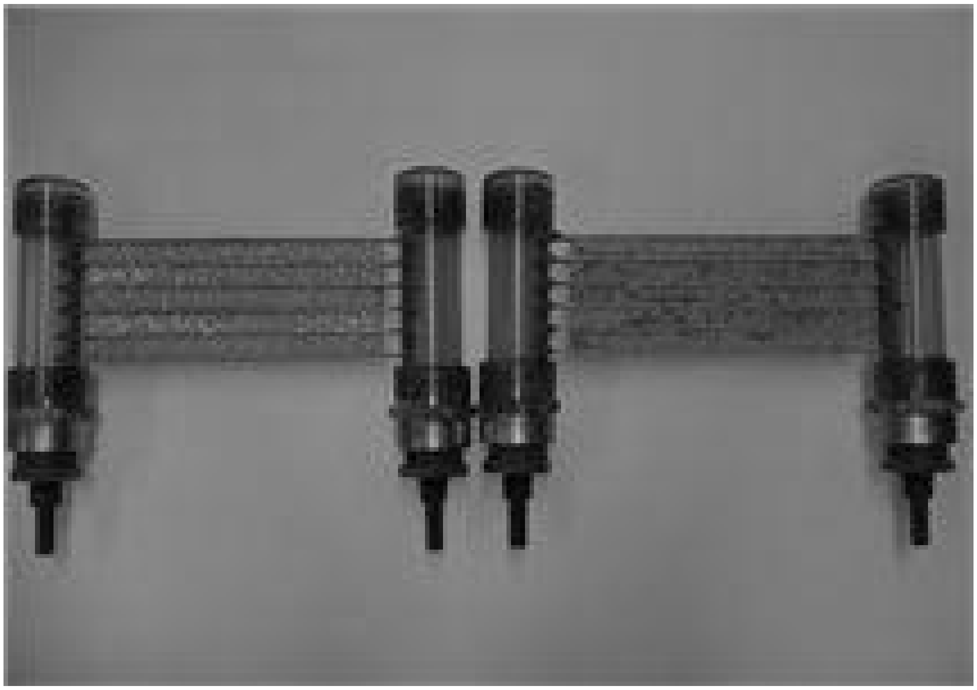

Figure A.6: Flat micro channel tube configuration

Table A.6: Design specification

Sample	11-12
Porosity	10 PPI
Base metal	Al 6061 alloy
Tube side configuration	Flat tube micro channel
Bonding method	Brazed, Artic silver
Number of fins	5
Face area	200 mm×85 mm
Tube width	25.4
Fin depth	15 mm
Fin thickness	15 mm
Channel area	14.96 mm^2
Number of channel	8

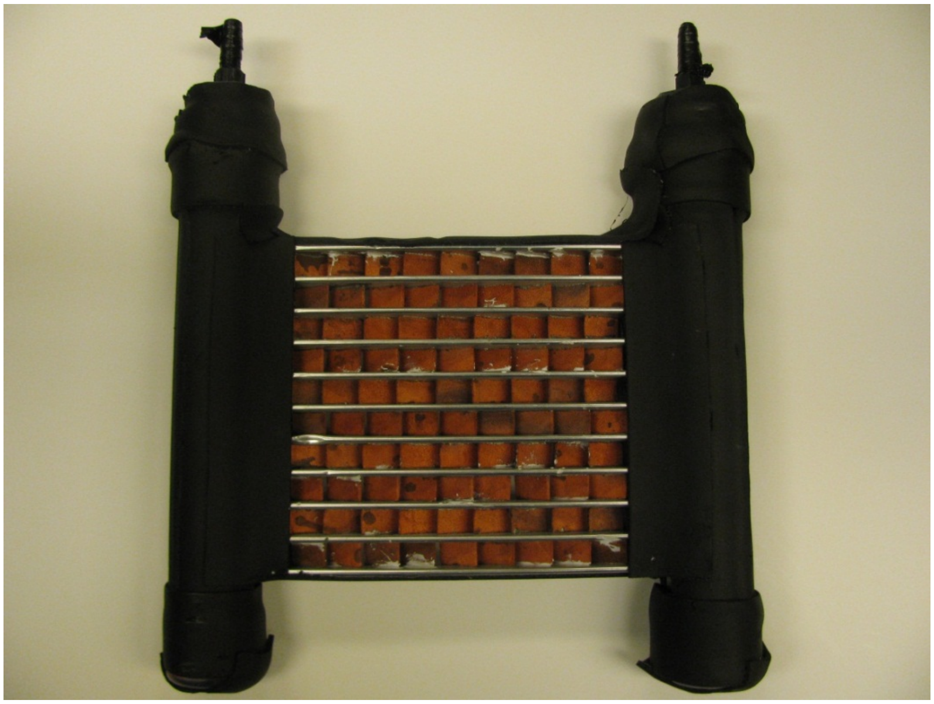

Figure A.7: Folded copper foam configuration

Table A.7: Design specification

Sample	13
Base metal	Copper alloy
Porosity	80 PPI
Tube side configuration	Flat tube
Number of fins	10
Bonding method	Artic silver
Face area	200 mm×180 mm
Tube width	25.4 mm
Fin structure	Folded
Flow depth	15 mm
Fin height	15 mm
Tube wall thickness	0.5 mm

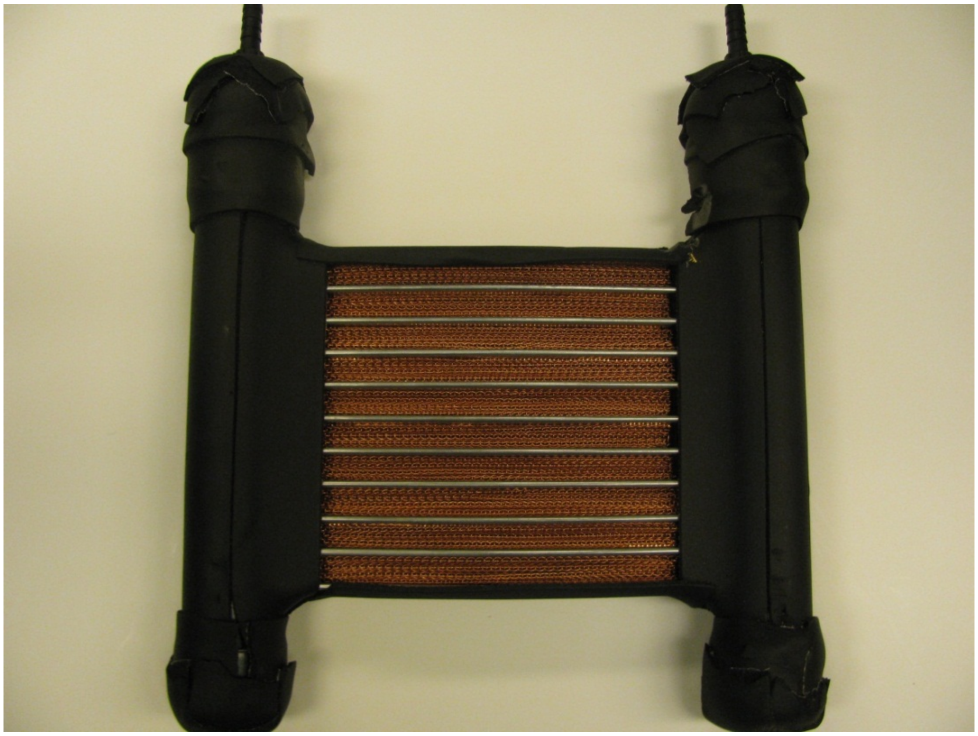

Figure A.8: Flat plate copper mesh configuration

Table A.8: Design specification

Sample	14
Base metal	Copper wire mesh
Porosity	2 mm
Tube side configuration	Flat tube
Number of fins	10
Bonding method	Thermal compound
Face area	200 mm×180 mm
Fin depth	15 mm
Fin thickness	15 mm
Tube width	25.4 mm
Tube wall thickness	0.5 mm

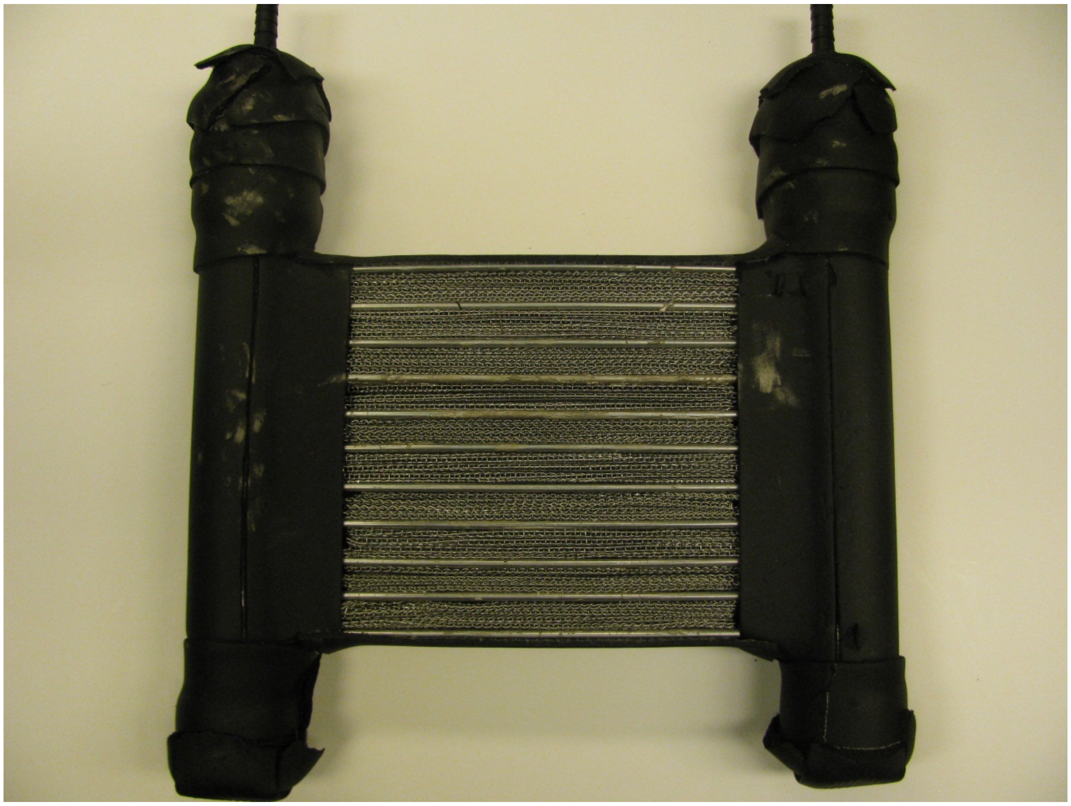

Figure A.9: Flat plate steel mesh configuration

Table A.9: Design specification

Sample	15
Base metal	Stainless steel wire mesh
Porosity	2 mm
Tube side configuration	Flat tube
Number of fins	10
Bonding method	Thermal compound
Face area	200 mm×180 mm
Fin depth	15 mm
Fin thickness	15 mm
Tube width	25.4 mm
Tube wall thickness	0.5 mm

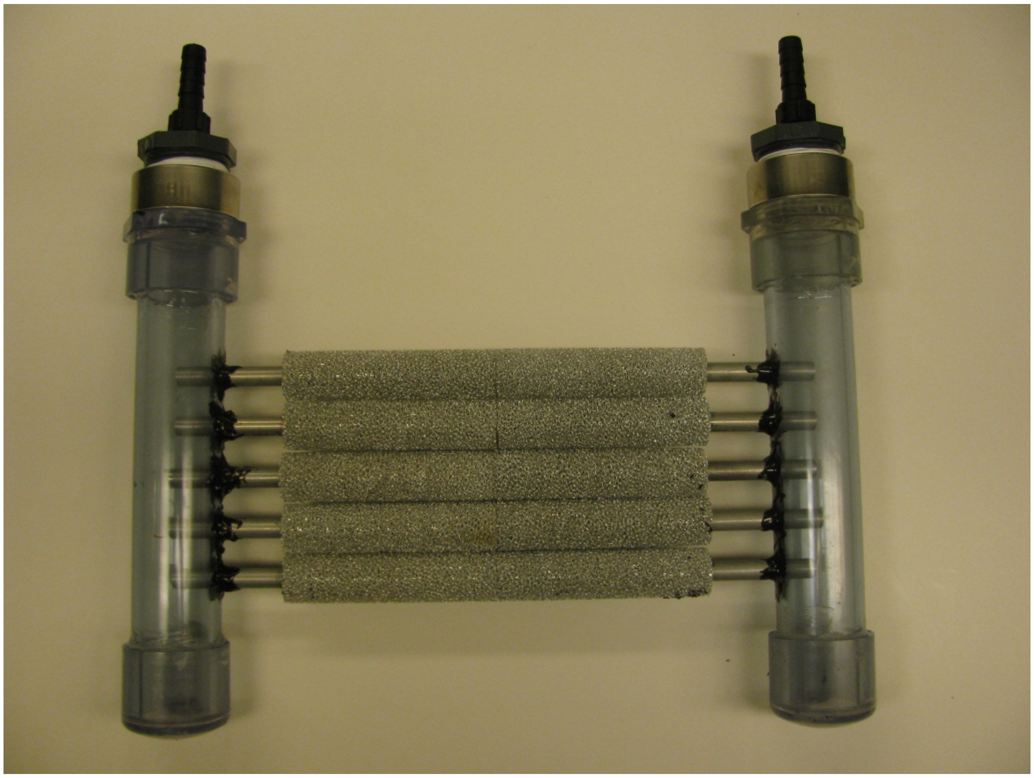

Figure A.10: Round tube annular configuration

Table A.10: Design specification

Sample	16
Porosity	10 PPI
Base metal	Aluminum
Tube side configuration	Round tube
Bonding method	brazed
Face area	180 mm×78 mm
Tube diameter	10 mm
Tube thickness	0.5 mm
Number of tubes	5

Appendix B: Correlations for thermal and hydraulic performance

Investigator	Porous material	PPI	Correlation(Nu)	Notation and definition
Tzeng and Jeng	Al foam	10-40	$Nu_H = 21.1Re_H^{0.457}$	
Leong and Jin	Al foam	40	$Nu_H = 12.3A_0^{0.95}Re_H^{0.31}$	A_o is maximum flow displacement
Hseih et al	Al foam	10-20-40	$Nu = 0.51Re_{D_p}^{0.38} \quad for\ 10PPI$ $Nu = 0.44Re_{D_p}^{0.44} \quad for\ 20PPI$ $Nu = 0.63Re_{D_p}^{0.46} \quad for\ 40PPI$	D_p is equivalent spherical diameter of porous media
Tzeng	Al foam	10	$Nu_H = 4.835Re_H^{0.52}$	
Noh et al	Al foam	10	$Nu = 23.1Re_{Dh}^{0.4}Pr^{-0.1}Da^{0.09}$	
Calmidi and Mahajan	Al foam	5-10-20-40	$Nu = 0.52\left(\frac{Re_H}{\varepsilon H}\right)^{0.5} Pr^{0.37}$	ε is the porosity
Zukauskas	Copper and Steel Alloy	10-20-30-60	$Nu = 0.76Re_D^{0.4}Pr^{0.37} \quad 1 \le Re_D \le 4$ $Nu = 0.52Re_D^{0.5}Pr^{0.37} \quad 4 \le Re_D \le 10^3$ $Nu = 0.26Re_D^{0.6}Pr^{0.37} \quad 10^3 \le Re_D \le 2 \times 10^5$	Re_D is the local Reynolds number $D = (1 - e^{(1-\varepsilon)/0.04})d_f$
Ichimia	Ceramic foam	20	$Nu = 2.43Re_{Dp}^{0.4} \quad 65 \le Re_{Dp} \le 457$	
Hwang	Al foam	10	$Nu = 0.32Re_{Dp}^{0.6} \quad 1900 \le Re_{Dp} \le 7800$	
Hwang	Sintered bronze beads	None	$Nu = 0.081(1-\varepsilon)\varepsilon^2 Re_d^{1.35}Pr^{0.33}\left({}^{D_p}/_{d}\right)^{0.35} \quad Re_d \le 75$ $Nu = 21.65(1-\varepsilon)\varepsilon^2 Re_d^{0.59}Pr^{0.33}\left({}^{D_p}/_{d}\right)^{0.35} \quad Re_d \le 350$	d is the diameter of fiber or sphere of porous heat sink

Investigator	Correlation(Nu)	Notation and definition
Giani et al	$f = 0.87 + \frac{13.56}{Re}$ $\frac{\Delta P}{L} = 13.56\,\frac{a^3}{2(a-d_s)^4 d_s}\,\mu u + 0.87\,\frac{a^3}{2(a-d_s)^4 d_s}\,\rho u^2$	$d_s = a\left[\frac{4}{3\pi}(1-\varepsilon)\right]^{1/2}$ $Re = \frac{\rho d_s u}{\mu}$
Lu et al	$f = \left[0.044 + \frac{0.008(a/d_s)}{(a/d_s - 1)^{0.43+1.13(a/d_s)}}\right] Re^{0.15}$	$d_s = a\,\frac{2}{\sqrt{3\pi}}[1-\varepsilon]^{1/2}$ $Re = \frac{\rho d_s(u - d/a)}{\mu}$
Lu et al	$f = 22 + \frac{(1-\varepsilon)}{Re} + 0.22$ $\frac{\Delta P}{L} = 22\,\frac{(1-\varepsilon)^2}{\varepsilon^2 d_p^2}\,\mu u + 0.22\,\frac{(1-\varepsilon)}{\varepsilon^2 d_p}\,\rho u^2$	$d_p = 1.5a\,\frac{(1-\varepsilon)}{\varepsilon}$ $Re = \frac{\rho d_p u}{\mu}$
Innocentini et al	$f = 150\,\frac{(1-\varepsilon)}{Re} + 1.75$ $\frac{\Delta P}{L} = 150\,\frac{(1-\varepsilon)^2}{\varepsilon^2 d_p^2}\,\mu u + 1.75\,\frac{(1-\varepsilon)}{\varepsilon^2 d_p}\,\rho u^2$	$d_p = 1.5a\,\frac{(1-\varepsilon)}{\varepsilon}$ $Re = \frac{\rho d_p u}{\mu}$
Khayargoli	$\frac{\Delta P}{L} = 100\,\frac{(1-\varepsilon)^2}{\varepsilon^2 d_p^2}\,\mu u + \frac{(1-\varepsilon)}{\varepsilon^2 d_p}\,\rho u^2$	$d_p = 1.5a\,\frac{(1-\varepsilon)}{\varepsilon}$
Lacroix et al	$f = 150\,\frac{(1-\varepsilon)}{Re} + 1.75$ $\frac{\Delta P}{L} = 150\,\frac{(1-\varepsilon)^2}{\varepsilon^2 d_p^2}\,\mu u + 1.75\,\frac{(1-\varepsilon)}{\varepsilon^2 d_p}\,\rho u^2$	$d_p = 1.5 d_s$ $Re = \frac{\rho d_s u}{\mu}$ $d_s = \frac{a[4/3\pi(1-\varepsilon)]^{1/2}}{1 - a[4/3\pi(1-\varepsilon)]^{1/2}}$

Moreira et al	$\frac{\Delta P}{L} = 1.275 \times 10^{9} \frac{(1-\varepsilon)^2}{\varepsilon^2 a^{-0.05}} \mu u + 1.89 \times 10^{4} \frac{(1-\varepsilon)}{\varepsilon^2 a^{-0.25}} \rho u^2$	
Tadrist et al	$\frac{\Delta P}{L} = c_1 \frac{(1-\varepsilon)^2}{\varepsilon^2 d_s^2} \mu u + c_2 \frac{(1-\varepsilon)}{\varepsilon^2 d_s} \rho u^2$	$100 \leq c_1 \leq 865$ $0.65 \leq c_2 \leq 2.6$
Topin	$\frac{\Delta P}{L} = \frac{1}{1.391 \times 10^{-4}} \frac{(1-\varepsilon)^2}{\varepsilon^2 d_s^2} \mu u + 1.37 a \rho u^2$	
Battachariya	$-\frac{dp}{dx} = \frac{\mu u}{K} + \frac{\rho f}{\sqrt{K}} u^2$	

Many researchers have tried to develop models to predict the thermal-hydraulic performance of porous media. The above two tables summarize the relationships available in literature to predict the thermal performance (Nusselt number) and the hydraulic performance (Pressure gradient or friction factor).

Appendix C: Data reduction

After determining the heat transfer rate under varying flow conditions, data were reduced to determine the heat transfer coefficient. The heat transfer coefficient is a good measure of performance; it can be made dimensionless using the Nusselt number or Colburn j factor. The energy balance for the experiments varied between 8 and 17 % for the dry test conditions and reached as high as 25 % for the wet test conditions. The uncertainty in the heat transfer rate to the coolant on tube side was small compared to that from the air side. So for the data reduction Q_c was used, because the following condition suggested by Young-Gil Park *et al*[1]. was satisfied:

$$\frac{\delta Q_a}{\delta Q_c} < \sqrt{3} \qquad (C.1)$$

For the data reduction purposes, the metal foam was consider as a porous fin with an adiabatic tip condition was used to determine the fin efficiency. A relation developed by Calmidi and Majahan[2] was used. LMTD (Log mean temperature difference) was used to reduce the data for dry condition test, while LMED (Log mean enthalpy difference) was used for wet conditions as both sensible and latent heat transfer were involved.

1- Park, Y., Liu, L., and Jacobi, A. M., 2010 “A rational approach for combining redundant, independent measurements to minimize combined experimental uncertainty” *Experimental Thermal and Fluid Science.*

2- Calmidi, V.V and Mahajan,R.L., 2000 “Forced Convection in High Porosity Metal Foams” J. Heat Transfer.

C.1 LMTD for data reduction under dry conditions

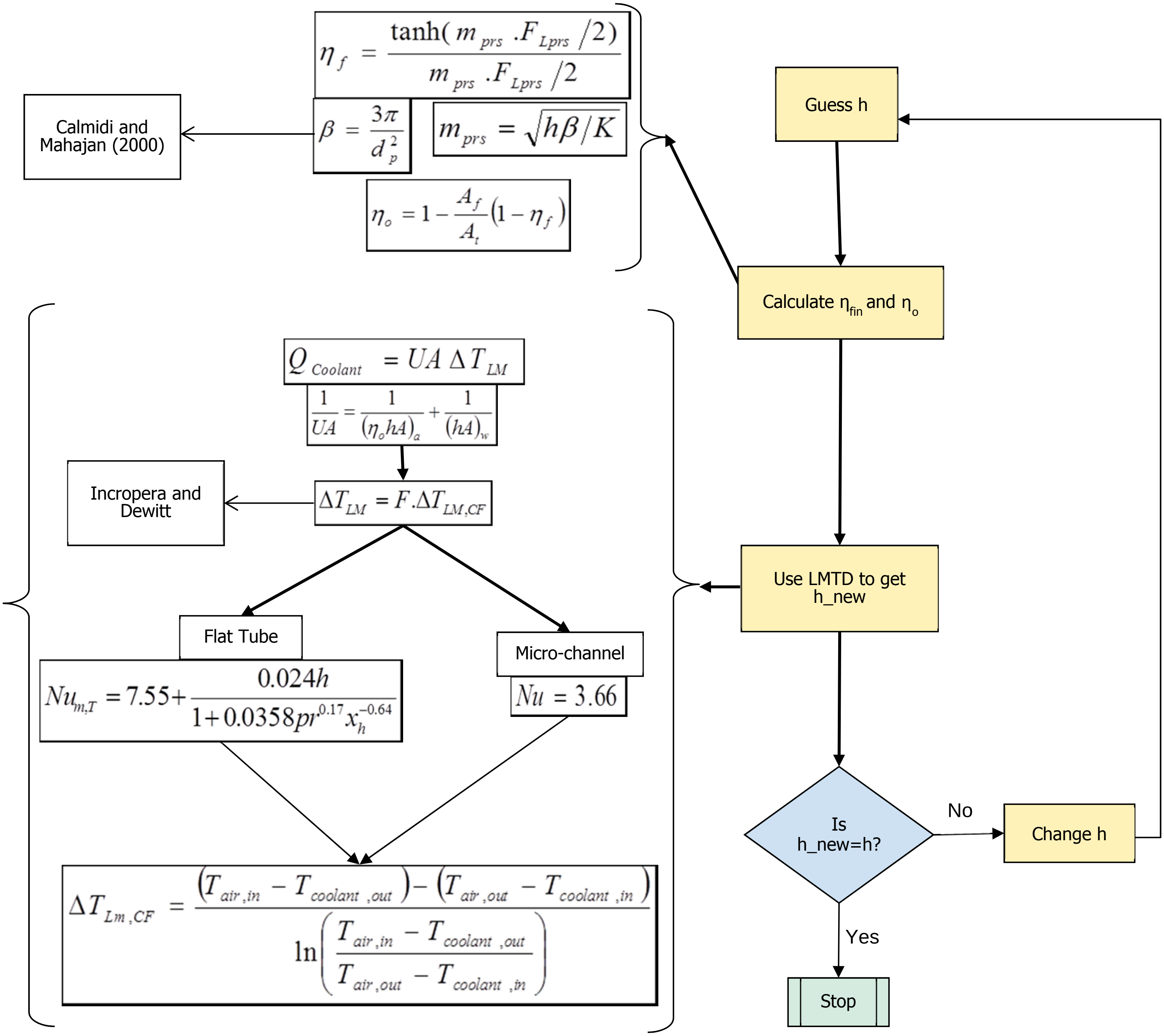

C.2 LMED for data reduction under wet conditions

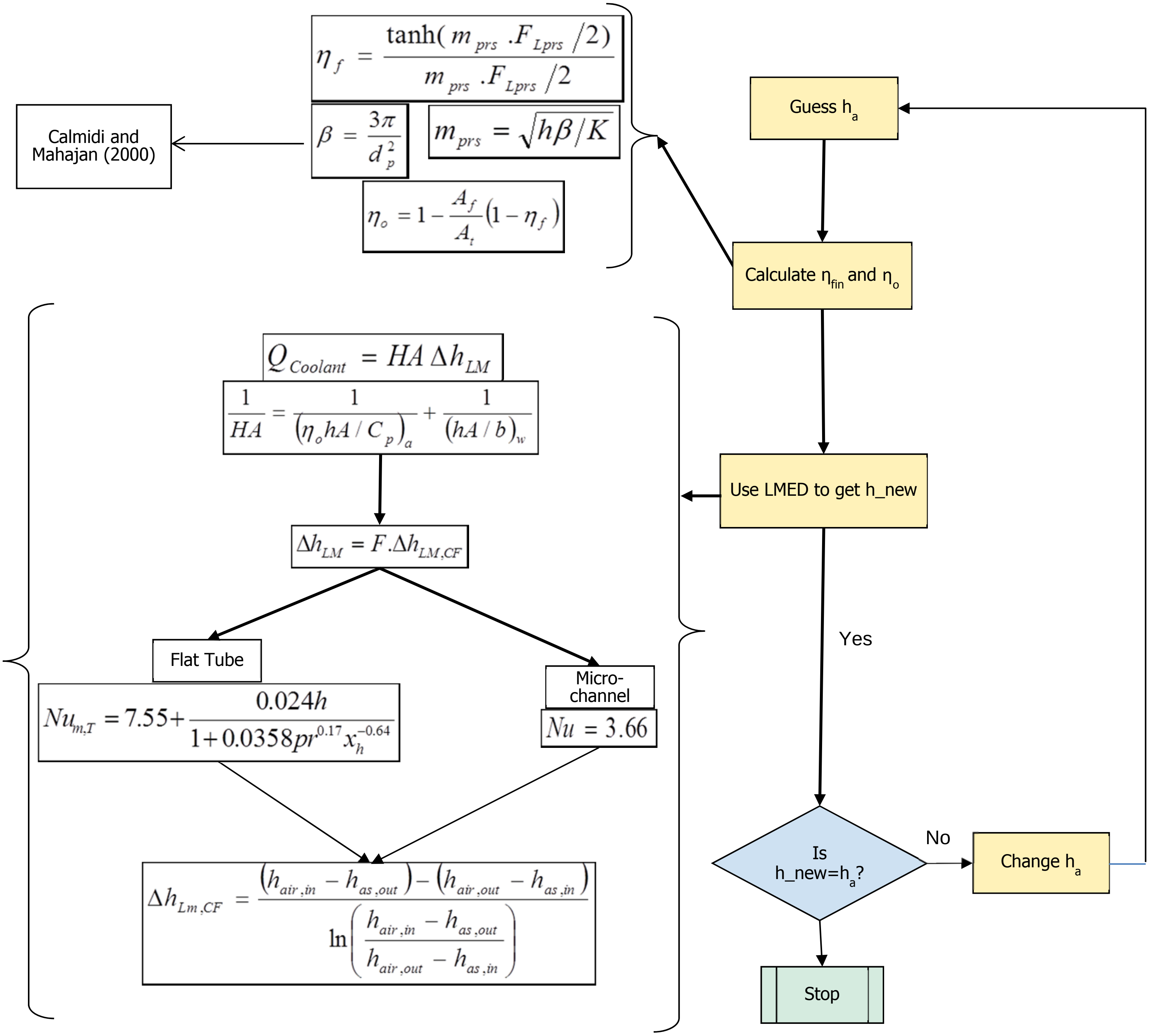

Appendix D: Experimental apparatus

D.1 Dynamic dip test apparatus

The dip testing apparatus consisted of a large water reservoir, a smaller submerged air reservoir to control the submersion of coils by displacement of water using compressed air, and a structure to suspend and weigh the heat exchanger.

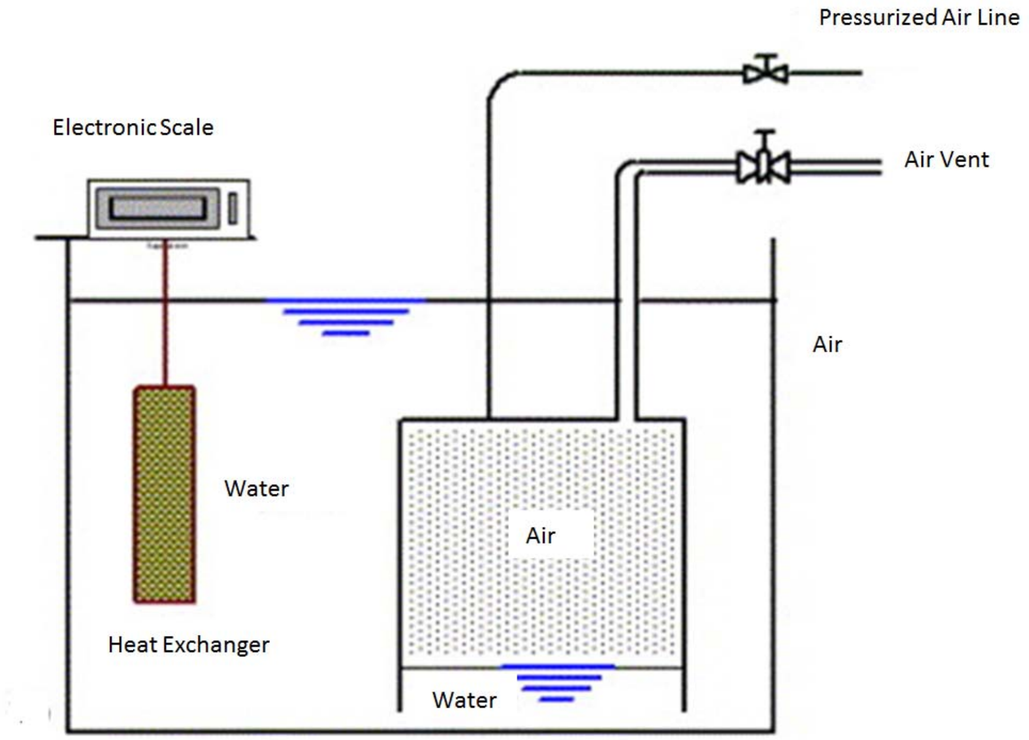

Figure D.1: Dynamic dip test apparatus

The sample was suspended from a balance using a fixed acrylic frame and simple mounting hardware. Before an experiment, the balance was turned on and zeroed after the test coil was suspended over the reservoir. At this point, the displacement tank was filled with water, and a final heat exchanger alignment check was performed. In order to initialize a test, the air vent was then closed, and the air supply was used to fill the displacement tank, causing the water level to rise and submerge the test specimen. Once the specimen was submerged, the air supply was closed. The water in the tank was agitated, and a fine brush was used to remove bubbles from the heat exchanger surface. While recording weight data, the air vent was suddenly opened to allow water into the displacement tank. The water level in the main reservoir dropped faster than 0.2 m/s.

A computer-based data acquisition system with a minimum recording interval of 0.1 s was used for the mass measurements, and the instrument uncertainty is adopted as the mass measurement uncertainty for these computer-timed data.

D.2 Closed-loop wind tunnel

Dry and wet wind tunnel testing is conducted using a closed-loop wind tunnel for thermal hydraulic performance tests. As shown in Figure 2, air downstream of test section passes through a set of electric strip heaters, past a steam injection pipe, through an axial blower and another set of strip heaters, a flow nozzle, a mixing chamber, a flow conditioning section, a flow contraction, and the test section, completing the loop. Heater-controllers are used to maintain the desired upstream air temperature and dew point at steady state. Steam is generated by an electric humidifier. The air temperature is measured using thermopile grids, constructed using T-type thermocouples (2 channels upstream; 4 channels downstream), and chilled-mirror hygrometers are used to measure the upstream and downstream dew points. The cross-sectional flow area in the test section is in rectangular 30 cm wide and 20 cm high. An axial blower provides an air flow with face velocities at the test section from 0.3 to 7 m/s. An ASME flow nozzle, with a differential pressure transducer, is used to measure air mass flow rate. Another pressure transducer is used to measure air-side pressure drop across the test section. In order to be accurate pressure at both points is measured by two micro-manometers. For the determination of mas flow rate and face velocity a hot-wire anemometer is used along with ASME nozzle. A single-phase liquid, an aqueous solution of Ethylene Glycol (DOWTHERM 4000), is used as the tube-side heat transfer fluid. A chiller system with a commercial heat pump, two large coolant reservoirs, a PID-controlled electric heater, and a gear pump supplies the flow. The chiller system provides a coolant flow with a steady inlet temperature (within 0.1°C) at a capacity up to 20 kW. Coolant inlet and outlet temperatures are measured using RTDs with an uncertainty less than 0.05°C.

Coolant flow mixing devices are installed immediately upstream of the RTDs to provide a well-mixed flow and a uniform coolant temperature. A Coriolis-effect flow meter located in the downstream coolant pipe is used to measure mass flow rate. A PC-based data acquisition system (National Instruments) is used to record and monitor the experimental data. The significant experimental uncertainties involved in the dry and wet wind-tunnel experiments are listed in Table D.1.

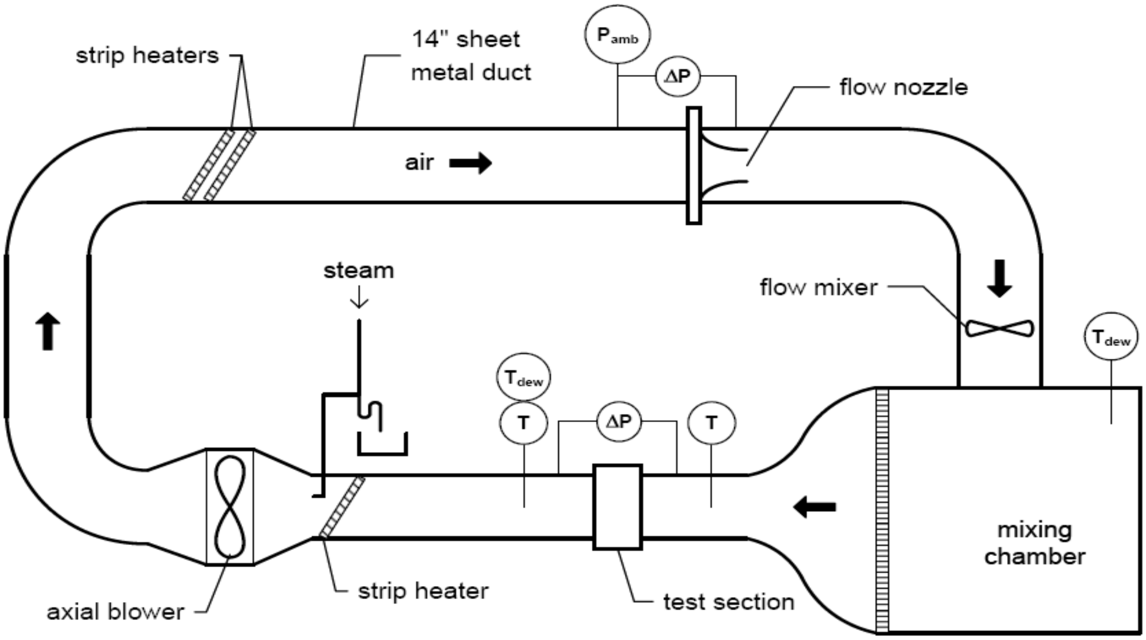

Figure D.2: Closed loop wind tunnel

Table D.1: Uncertainty of different parameters

Parameter	Uncertainty
Air temperature	$\pm 0.1\ C$
Coolant temperature	$\pm 0.03\ C$
Nozzle discharge coefficient	$\pm 2\ \%$
Core pressure drop	$\pm 0.17\ Pa$
Nozzle pressure	$\pm 0.087\ Pa$
Coolant mass flow rate	$\pm 0.1\%\ of\ reading$
Dew point	$\pm 0.2\ C$
Face velocity	$\pm 0.1\ m/s$
Pressure drop(micro manometer)	$\pm 0.2\ Pa$

Before beginning wind-tunnel tests, the heat exchanger specimens are insulated using foam insulation tape. If specimens have face dimensions different from those of the test section, it will be necessary to either cover a part of the heat exchanger face or install within the tunnel an additional flow contraction upstream and a diffuser downstream of the test specimen. The specimens will be mounted in the test section, the coolant hoses connected, and the gaps between the specimen and the test section sealed with adhesive tape. The entire wind tunnel, the test specimen, steam pipes, and coolant pipes will all be insulated to isolate the system as much as possible from the environment. Once the installation is complete, the components of the test apparatus are started and set to the desired test point temperatures, dew point, and flow rates. Steady-state conditions are considered to prevail when all individual variables measured are maintained constant within instrument uncertainty. For wet tests, however, an initial condensation period of at least 40 min is maintained. The recorded parameters include upstream and downstream air temperature, upstream and downstream dew point, coolant inlet and outlet temperature, nozzle pressure drop, core pressure drop, coolant mass flow rate, nozzle upstream pressure, ambient barometric pressure, and ambient air temperature. The data stream is sampled for a period long enough to ensure that the averaged readings were independent from temporal fluctuations (i.e., independent form random instrument errors). All experiments under dry conditions had an energy balance within 10%, while for wet condition energy balance was within 15 %.

Appendix E: Energy balance and uncertainty analysis

E.1 Energy balance

All the experiments were conducted under adiabatic condition. The test section was well insulated to prevent any heat leak. An acceptable energy balance is essential for accurate performance analysis. The relative difference between the heat rates on coolant and air side resulted due to the air heat leak which is unavoidable. The problems become rather sever at high face velocities. The energy balance is defined by equation E.1.

$$Q_{balance} = \left|\frac{Q_{air} - Q_{coolant}}{Q_{avg}}\right| \qquad \text{(E. 1)}$$

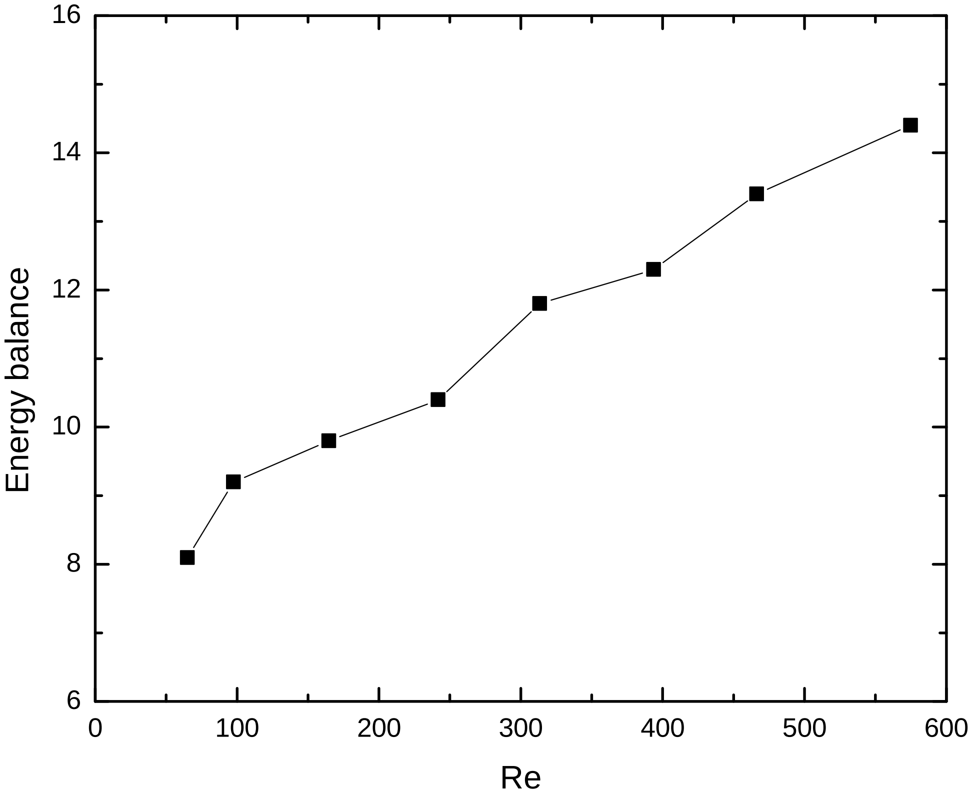

Figure E.1: Energy balance (as a percentage) at different flow conditions

Table E.1 specifies the energy balance under different test conditions. The larger number corresponds to the maximum flow rates.

Table E.1: Energy balance under different test condition

Test condition	Energy balance
Dry	8-15 %
Wet	10-25 %
Frost	10-25 %

E.2 Uncertainty analysis

Under different test conditions the energy balance. The uncertainty of different parameters involved in the analysis was calculated. Table E.1 presents the values of uncertainty of different parameters.

$$Re = \frac{\rho U D_h}{\mu} \tag{E.2}$$

$$\left(\frac{\partial Re}{Re}\right)^2 = \left(\frac{\partial \rho}{\rho}\right)^2 + \left(\frac{\partial U}{U}\right)^2 + \left(\frac{\partial D_h}{D_h}\right)^2 - \left(\frac{\partial \mu}{\mu}\right)^2 \tag{E.3}$$

$$f = \frac{\frac{\Delta P}{L} D_h}{\frac{1}{2}\rho U^2} \tag{E.4}$$

$$\left(\frac{\partial f}{f}\right)^2 = \left(\frac{\partial grad\ P}{grad\ P}\right)^2 + \left(\frac{\partial D_h}{D_h}\right)^2 - \left(\frac{\partial \rho}{\rho}\right)^2 - \left(\frac{2\partial U}{U}\right)^2 \tag{E.5}$$

$$Nu = \frac{h D_h}{k_f} \tag{E.6}$$

$$\left(\frac{\partial Nu}{Nu}\right)^2 = \left(\frac{\partial h}{h}\right)^2 + \left(\frac{\partial D_h}{D_h}\right)^2 - \left(\frac{\partial k_f}{k_f}\right)^2 \tag{E.7}$$

$$j = \frac{Nu}{Re Pr^{1/3}} \tag{E.8}$$

$$\left(\frac{\partial j}{j}\right)^2 = \left(\frac{\partial Nu}{Nu}\right)^2 - \left(\frac{\partial Re}{Re}\right)^2 - \left(\frac{1}{3}\frac{\partial Pr}{Pr}\right)^2 \tag{E.9}$$

Table E.2: Uncertainty of performance parameters

Parameter	Uncertainty
Re	± 4 %
f	± 7 %
Nu	± 12 %
j	± 8 %

Appendix F: Effective thermal conductivity model for metal foams

Authors: Zengshu Dai, Kashif Nawaz, Young-Gil Park, Jessica Bock, Anthony Jacobi

Abstract

Metal foams have emerged as promising materials for use in heat sink and heat exchanger applications. Boomsma and Poulikakos put forward an important and widely adopted model for the effective thermal conductivity of metal foams; however, the model contains errors in its development and presentation. Whether partially or fully corrected, the model does not provide accurate predictions of the effective thermal conductivity of metal foams. Because the model fails even when corrected, its mechanistic basis is reviewed, and an extension to the approach is put forward to account for ligament orientation in calculating effective thermal conductivity. This modification provides predictions of k_{eff} that are much more accurate than the original Boomsma-Poulikakos model.

Nomenclature

A	area (m^2)
a	foam ligament radius (m)
d	dimensionless foam ligament radius, $d = a/L$
e	dimensionless cubic node edge length, $e = r/L$
k	thermal conductivity ($W\ m^{-1}\ K^{-1}$)
L	node-to-node length (m)
q	heat transfer rate (W)
R	thermal resistance on a flux basis ($m^2\ K\ W^{-1}$)
r	cubic node edge length (m)
T	temperature (^{o}C)
V	volume (m^3)

Greek symbols

ε	porosity
Φ	angle between ligament axis and vertical (see Fig. F.4).
χ	multiplier applied to porosity (see § F.4)

Subscripts

A	unit cell subsection	(see Fig. F.2)
B	unit cell subsection	(see Fig. F.2)
C	unit cell subsection	(see Fig. F.2)
D	unit cell subsection	(see Fig. F.2)
eff	effective	
exp	from an experiment	
f	fluid	
n	index representing A, B, C, D	
s	solid	

F.1 Introduction

Open-cell metal foams are considered promising materials for heat sinks and compact heat exchangers, due to the properties of the foams, such as high heat transfer surface area per unit volume, and high convective heat transfer coefficients due to good fluid mixing. A recent review of the promise of metal foams for heat exchanger applications was provided by Han *et al.* [1], and a comparison of metal-foam heat exchangers to louver-fin heat exchangers was presented by Dai *et al.* [2]. The effective thermal conductivity is a very important characteristic of high porosity metal foams in heat transfer applications, and modeling the effective thermal conductivity of metal foams has attracted a lot of attention.

Calmidi and Mahajan [3] investigated the effective thermal conductivity of highly porous metal foams experimentally with both water and air as the fluid phase. An empirical correlation was developed and a theoretical model was derived based on a hexagonal structure of the metal foam. Calmidi and Mahajan showed that the results predicted by their model matched the experimental results very well—within 10%—when the "area ratio" ($2a/r$) was set at 0.09. Bhattacharya *et al.* [4] modified the model of Calmidi and Mahajan [3] by replacing the cubic nodes (the location where ligaments or fibers join) with circular ones. They stated that by using an appropriate value of the ratio of fiber radius to the node radius the model was generally successful for high-porosity media. A simple empirical correlation was also developed for estimating the effective thermal conductivity in terms of the porosity, and the solid and fluid conductivities.

On the basis of available experimental data and results from numerical simulation, Singh and Kasana [5] presented a simple resistor-based model for estimating the effective thermal conductivity of highly porous metal foams. The model showed that the effective thermal conductivity strongly depends on porosity and the ratio of thermal conductivity of the constituents. The results matched the experimental data very well, with an average relative error of less than about 3%.

Boomsma and Poulikakos [6] developed a one-dimensional heat conduction model for use with open-cell metal foams, based on idealized three-dimensional unit cell geometry. The model showed that the thermal conductivity of solid phase plays an important role in the overall effective thermal conductivity, and their predictions with the model were reported to accurately match the experimental data of Calmidi and Mahajan [3]. However, a careful review of the Boomsma-Poulikakos model reveals errors in its development and presentation; in particular:

- There is a geometrical error in how the solid volume for layer 'C' is determined (see [6], Eq. 13).
- There is a mathematical error in reference [6]; namely, the solution for Eq. (15) of [6] is not as given in Eq. (16) of [6]
- There is a presentation error, because using the equations as given (see [6], Eqs. 19-23) with *e*=0.339 as specified in the paper, does not produce the published curve (for example, see [6], Figs. 2-4).

In this paper, these problems will be explored in detail, with a focus on understanding their origin and their impact on the model accuracy. The model will be corrected, and predictions from the corrected model will be compared to extant experimental data [3]. Finally, it will be shown that the porosity-weighted approach for calculating the effective thermal conductivity adopted in the Boomsma-Poulikakos model does not account for ligament orientation, and an extension to account for such effects will be developed.

F.2 Correcting the Boomsma-Poulikakos Model

F.2.1 Porosity

The tetradecahedron (also called a tetrakaidecahedron) selected by Boomsma and Poulikakos to describe the ligament and node arrangement in open-cell metal foams is shown in Fig. F.1; it consists of six square faces and eight hexagonal faces. The selection of a tetradecahedron is an idealization of the metal-foam geometry, with recognition that the ligament-node arrangement in real metal foams is not always uniform, nor is each cell identical. Nevertheless, this idealization has precedent in the literature and is a reasonable representation of the geometrical features of the metal foam. The geometry was further idealized, with the nodes (the intersection of ligaments) modeled as cubes, and the ligaments modeled as right-circular cylinders. The length of the edge of a node is denoted as *r*, while the node-to-node length is *L* (from node center to node center), and the ligament radius is *a*. For the purpose of geometric clarity, four layers of lengths L_A, L_B, L_C, and L_D were defined in reference [6], as shown in Fig. F.2, together comprising a unit cell.

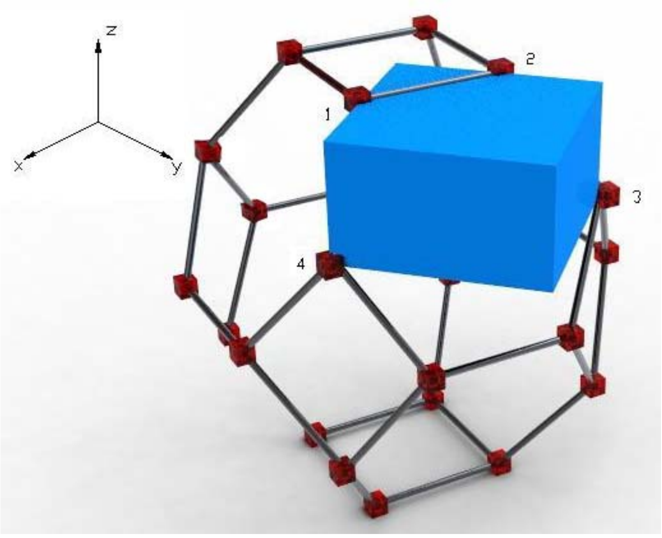

Figure F.1: Tetradecahedron with an inserted rectangular unit following Boomsma and Poulikakos [6]

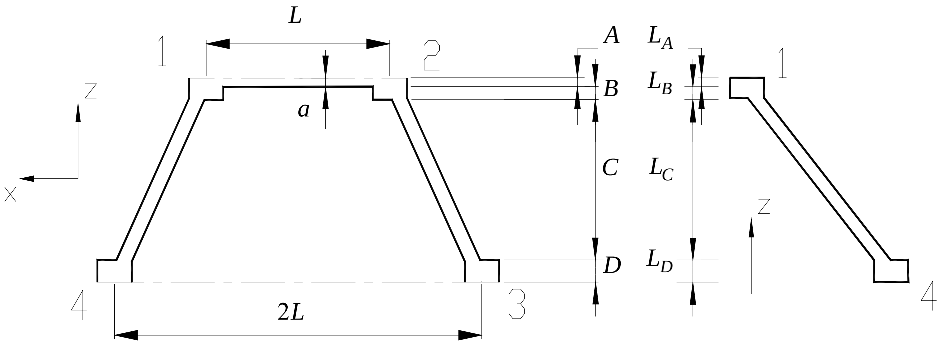

Figure F.2: Four discrete layers are defined based on distinct geometrical features, following Boomsma and Poulikakos [6]

In calculating the foam porosity, Eqs. (F.1)-(F.6) follow the work of Boomsma and Poulikakos [6], except for Eq. (F.6c). However, for the sake of brevity not every equation in the original paper is repeated in this paper, and for the sake of clarity some additional equations are provided. Thus, the equation numbers in the current work differ from those in reference [6]. The equation numbers from the original article will be given as needed for comparison.

The height of the rectangular unit cell in the z direction is (see Fig. F.2)

$$L_A + L_B + L_C + L_D = L\sqrt{2}/2 \tag{F.1}$$

The heights of the four layers are

$$L_A = a \tag{F.2a}$$

$$L_B = r/2 - a \tag{F.2b}$$

$$L_C = \left(L\sqrt{2}/2\right) - r \tag{F.2c}$$

and

$$L_D = r/2 \tag{F.2d}$$

The total volume (solid and void) of each rectangular section is calculated as follows

$$V_A = 2aL^2 \tag{F.3a}$$

$$V_B = (r - 2a)L^2 \tag{F.3b}$$

$$V_C = \left(L\sqrt{2} - 2r\right)L^2 \tag{F.3c}$$

$$V_D = rL^2 \tag{F.3d}$$

Reference [6] then introduced non-dimensional relationships as follow:

$$d = a/L \tag{F.4}$$

$$e = r/L \tag{F.5}$$

Using the definitions for *d* and *e*, the volume of solid for each layer is

$$V_{A,s} = \left[e^2 + \pi d(1-e)/2\right]dL^3 \tag{F.6a}$$

$$V_{B,s} = \left[(e/2) - d\right]e^2L^3 \tag{F.6b}$$

$$V_{C,s} = (1 - e\sqrt{2})\pi d^2 L^3 \tag{F.6c}$$

$$V_{D,s} = \left(e^3 L^3\right)/4 \tag{F.6d}$$

Note that Eq. (F.6c) differs from the corresponding equation of reference [6] (see [6], Eq. 13). The volume of solid in layer 'C' as given above in Eq. (F.6c) is correct: the expression given in reference [6] is incorrect. In order to see that Eq. (F.6c) given above is correct, recognize that the volume of solid in the layer, as can be seen in Fig. F.3, is half the volume of ligament 1-4 plus half the volume of ligament 2-3, because each of these ligaments is half inside the unit cell. The ligament length is $L - r\sqrt{2}$, and half the cross-sectional area is $\pi a^2/2$. Accounting for both ligaments, the solid volume is $(L - r\sqrt{2})\pi a^2$, which is equivalent to the expression given above as Eq. (F.6c).

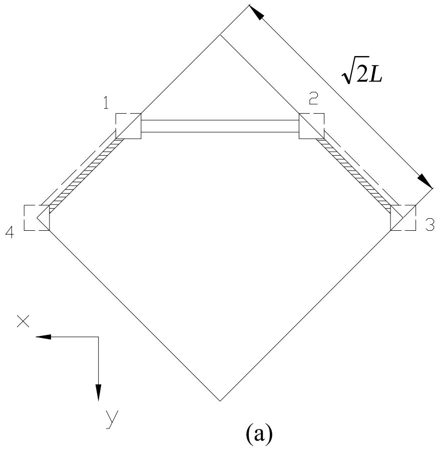

(a)

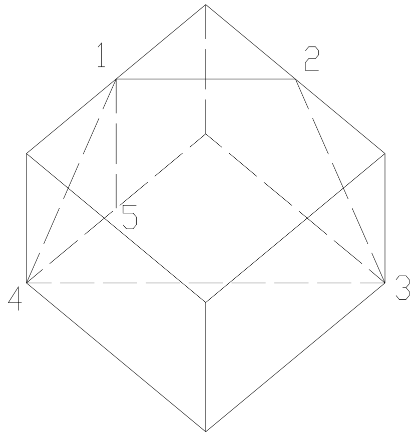

(b)

Figure F.3: (a) The top view of the rectangular unit (b) The schematic of rectangular unit

Porosity, which is defined as the ratio of void volume to the total volume, is calculated based on *d* and *e* as follows,

$$\varepsilon = 1 - \frac{\sqrt{2}}{2}\left[de^2 + \frac{\pi d^2}{2}(1-e) + \left(\frac{e}{2} - d\right)e^2 + \pi d^2\left(1 - e\sqrt{2}\right) + \frac{e^3}{4}\right] \qquad \text{(F.7a)}$$

Equation (F.7a) differs from that given for porosity in reference [6] (see [6], Eq. 15), because of the error in formulating $V_{C,s}$ in reference [6]. The correct positive root for *d* from Eq. (F.7a) is

$$d = \left[\frac{\sqrt{2}(2 - 2\varepsilon - \frac{3\sqrt{2}}{4}e^3)}{\pi(3 - e - 2e\sqrt{2})}\right]^{1/2} \qquad \text{(F.7b)}$$

This result differs from the solution given in reference [6] (see [6], Eq. 16), again because of the error in formulating $V_{C,s}$ in reference [6].

In addition to the geometric error identified in how reference [6] formulates $V_{C,s}$, there is a mathematical error in reference [6]. Even if the geometric error in formulating $V_{C,s}$ is accepted, the solution for *d* given as Eq. (16) in reference [6] does not follow from the expression for porosity given as Eq. (15) in reference [6]. The correct solution to the geometrically incorrect expression for porosity (i.e., the correct version of Eq. (16) in reference [6]) is:

$$d = \left[\frac{\sqrt{2}\left(2 - 2\varepsilon - \frac{3\sqrt{2}}{4}e^3\right)}{\pi\left(3 - e - 4e\sqrt{2}\right)}\right]^{1/2} \qquad \text{(F.8)}$$

F.2.2 Effective thermal conductivity

Following the prior work of Boomsma and Poulikakos [6], the effective thermal conductivity is formulated by a porosity weighting of the thermal conductivity of the solid and the fluid as follows:

$$k_{eff} = \varepsilon k_f + (1-\varepsilon)k_s \qquad \text{(F.9)}$$

For each of the four layers, n=A, B, C, and D, the conductivity of the layer from Eq. (F.9) follows

$$k_n = \frac{V_{n,s}k_s + (V_n - V_{n,s})k_f}{V_n} \tag{F.10}$$

Thus, for each layer,

$$k_A = \frac{k_s}{2}\left(e^2 + \pi d(1-e)/2\right) + \frac{k_f}{2}\left(2 - e^2 - \pi d(1-e)/2\right) \tag{F.11a}$$

$$k_B = \frac{e^2 k_s}{2} + (1 - e^2/2)k_f \tag{F.11b}$$

$$k_C = \pi d^2 k_s \sqrt{2}/2 + \left(1 - \pi d^2 \sqrt{2}/2\right)k_f \tag{F.11c}$$

and

$$k_D = e^2 k_s/4 + \left(1 - e^2/4\right)k_f \tag{F.11d}$$

The thermal resistance (on a flux basis) of each layer is

$$R_A = \frac{L_A}{k_A} = \frac{4dL}{\left[2e^2 + \pi d(1-e)\right]k_s + \left\{4 - \left[2e^2 + \pi d(1-e)\right]\right\}k_f} \tag{F.12a}$$

$$R_B = \frac{L_B}{k_B} = \frac{(e-2d)L}{e^2 k_s + (2-e^2)k_f} \tag{F.12b}$$

$$R_C = \frac{L_C}{k_C} = \frac{\left(\sqrt{2} - 2e\right)L}{\pi d^2 k_s \sqrt{2} + \left(2 - \pi d^2 \sqrt{2}\right)k_f} \tag{F.12c}$$

$$R_D = \frac{L_D}{k_D} = \frac{2eL}{e^2 k_s + \left(4 - e^2\right)k_f} \tag{F.12d}$$

Finally, by assuming that each layer provides a resistance in series with the others, the combined resistance is taken as the effective thermal conductivity

$$k_{eff} = \frac{L_A + L_B + L_C + L_D}{R_A + R_B + R_C + R_D} \tag{F.13}$$

F.3 Extending the Boomsma-Poulikakos Model

The results presented in the next section will demonstrate that predictions of k_{eff} from the Boomsma-Poulikakos model do not match the data of reference [3], whether the equations are used as presented in reference [6], whether they are corrected to properly formulate $V_{C,s}$, or whether they are modified to correct the algebraic error in finding d. Also presented in the next section is conjecture as to how the published findings of reference [6] showing good agreement might have been obtained. In any case, the failure of the approach outlined in reference [6] suggests that there is a flaw in the physical arguments forming its basis.

The fundamental approach adopted in reference [6] is to assume a tetradecahedral metal foam geometry, and that the effective thermal conductivity is the volume-fraction-weighted thermal conductivity. Fully corrected, this approach does not make predictions of the effective thermal conductivity consistent with measured results. There are reasons to call the assumed foam geometry into question (see [7-10]), and the failure of the approach may be due to the foam geometry departing significantly from that assumed. However, what is perhaps more important is that the weighting used in Eq. (F.9) is not true in a general sense—it does not properly account for the ligament orientation in layer 'C'. When the thermal conductivity of the solid phase (i.e. ligament) is much larger than that in the fluid phase, heat conduction within the solid essentially follows the ligament, and the ligament may not be aligned with the direction of heat conduction in the fluid phase. The expression in Eq. (F.9) implies parallel heat conduction in the solid and fluid phases, but that does not occur in the current geometrical model. In this section, the Boomsma-Poulikakos model will be extended to account for this effect.

Consider a layer of composite fluid and solid of thickness L_C, as shown in Fig. F.4a. Assuming heat conduction along the axis of the solid and in the z-direction in the fluid, with no inter-phase heat transfer, we may write the heat transfer from surface '2' to surface '1' as follows:

$$q = k_f A_f \frac{T_2 - T_1}{L_C} + k_s A_s \frac{T_2 - T_1}{L_C} \tag{F.14}$$

where, A_f is the fluid surface area at z=0 and A_s is the solid surface area at z=0. Defining the effective thermal conductivity, k_{eff} with

$$q = k_{eff} (A_f + A_s) \frac{T_2 - T_1}{L_C} \tag{F.15}$$

Combining Eqs. (F.14) and (F.15), yields

$$k_{eff} = \frac{A_f}{(A_f + A_s)} k_f + \frac{A_s}{(A_f + A_s)} k_s \tag{F.16}$$

Noting $\varepsilon = A_f/(A_s + A_f)$, the effective thermal conductivity given by Eq. (F.16) is identical to the model used in reference [6] and given in Eq. (F.9). However, in layer 'C' the ligament is not aligned with the z-axis.

Consider a layer of composite fluid and solid of thickness L_C, as shown in Fig. F.4b, where the solid ligament is inclined from the z-axis by angle Φ. Assuming heat conduction along the axis of the solid and in the z-direction in the fluid, with no inter-phase heat transfer, we may write the heat transfer from surface '2' to surface '1' as follows:

$$q = k_f A_f \frac{T_2 - T_1}{L_C} + k_s \left(A_s \cos\Phi\right) \frac{T_2 - T_1}{\left(L_C / \cos\Phi\right)} \tag{F.17}$$

Equation (F.17) is based on recognition that the cross-sectional area for heat conduction along the ligament axis is $A_s \cos\Phi$, and the distance along the ligament from surface '2' to surface '1' is $L_C/\cos\Phi$. Using the definition of k_{eff} as given in Eq. (F.15), and rearranging

$$k_{eff} = \frac{A_f}{(A_f + A_s)} k_f + \frac{A_s}{(A_f + A_s)} k_s \cos^2 \Phi \tag{F.18}$$

Recognizing that in this case as in the case of Fig. F.4a, $\varepsilon = A_f/(A_s + A_f)$, the final result accounting for fiber orientation is

$$k_{eff} = \varepsilon k_f + (1 - \varepsilon) k_s \cos^2 \Phi \tag{F.19}$$

This result differs from the approach of reference [6] and Eq. (F.9). Using Eq. (F.19) to reformulate the resistance of layer 'C', with $\Phi = 45^{\circ}$:

$$R_C = \frac{L_C}{k_C} = \frac{2\left(\sqrt{2}-2e\right)L}{\pi d^2 k_s \sqrt{2} + 2\left(2-\pi d^2\sqrt{2}\right)k_f} \tag{F.20}$$

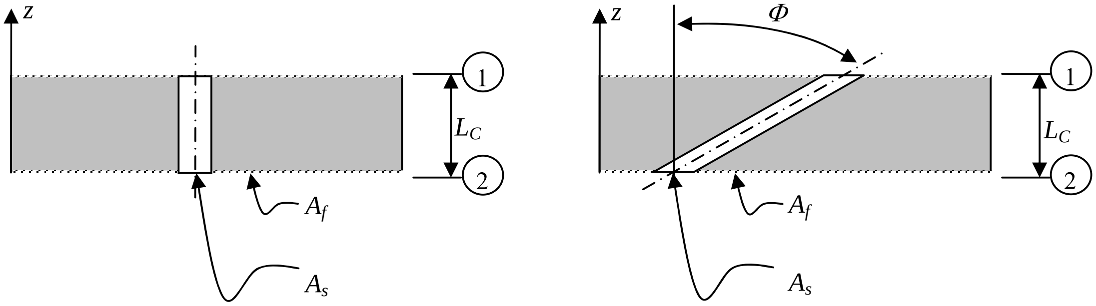

(a)

(b)

Figure F.4: Geometric systems for conduction analysis accounting for ligament orientation: (a) conduction in the fluid aligned with conduction in the ligament, and (b) conduction in the fluid not aligned with conduction in the ligament.

F.4 Results and Discussion

The equations as presented in this paper, and those presented by Boomsma and Poulikakos [6] were solved using Newton-Raphson iteration implemented in a commercial software package[†]. Iteration continued until the relative residuals were less than 10^{-6}, and the maximum change in any variable was less than 10^{-9}.

Implementing the effective thermal conductivity model exactly as given in reference [6], and using *e*=0.339 as required, fails to produce the published results. A comparison of model results to measurements is shown in Fig. F.5. In order to try to understand how the previously published results (Fig. F.2a of [6]) might have been obtained, the value of *e* was adjusted to minimize the RMS deviation of predictions from the measurements of reference [3]. The results are also provided in Fig. F.5, where it can be seen that such an approach does not provide good predictions or explain the discrepancy. Finally, with *e*=0.339 and the porosity $\varepsilon=\chi\varepsilon_{\text{exp}}$, χ was adjusted to minimize the RMS deviation of predictions from experiments, and the results in reference [6] were replicated with χ=0.98 (see Fig. F.5). Because the plots of

---

[†] *EES - Engineering Equation Solver*, F-Chart Software, Madison, WI 53744

reference [6] have an upper limit of ε=0.98, it seems plausible that there was an error in the implementation of the equations generating Fig. F.2a of reference [6]. Whether the equations are implemented exactly as presented in reference [6], or repaired with the geometric correction (*i.e.*, using Eq. F.7b), or repaired with the geometric error but an algebraic correction (*i.e.*, using Eq. F.8), the results presented in reference [6] are not replicated, and the predictions do not agree well with the data.

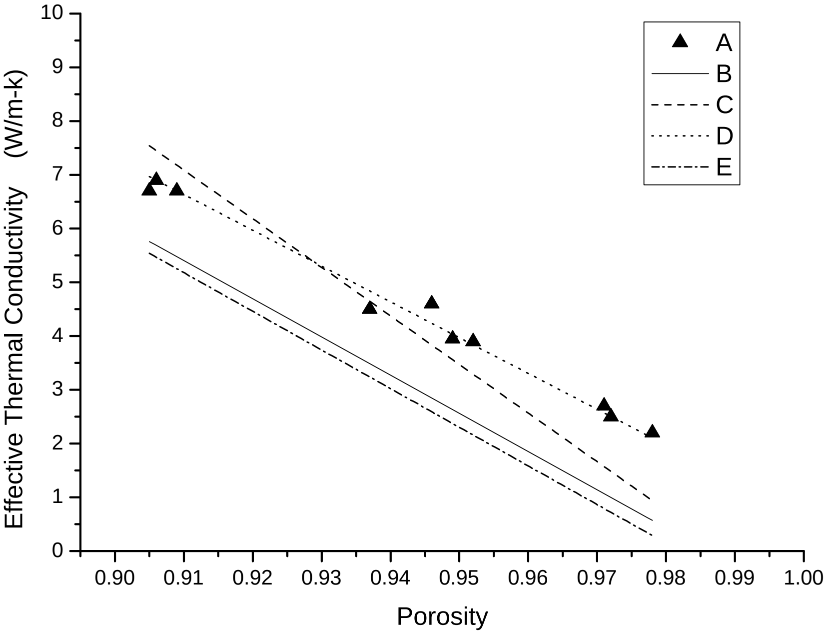

Figure F.5: Comparison of the predicted effective thermal conductivity and experimental data [3]. A-Experimental data from Calmidi and Mahajan [3]; B-Boomsma and Poulikakos model as given in reference [6] (e=0.339); C-Boomsma and Poulikakos model with e=0.331; D-Boomsma and Poulikakos model with e=0.339,□and χ=0.98; E-Boomsma and Poulikakos model with the geometric error but the algebraic expression for '*d*' corrected (e=0.339, χ=1)

With the fully corrected Boomsma-Poulikakos model (i.e., using *d* from Eq. F.7b, but not accounting for ligament orientation), using the data of Calmidi and Mahajan [3], a value of e=0.198 was found to minimize the RMS deviations of predictions from the data. The results, provided in Table F.1, show that the corrected model does not provide adequate predictions, with relative errors in k_{eff} ranging from about 61% to 88% for air, and 37% to 81% for water.

Even if the value of e minimizing RMS deviations is determined separately for air and water (note, e is a geometric parameter) the results are not much better. The over-prediction of k_{eff} in the table can be due the neglect of ligament orientation effects. The ratio of the node length to the radius of ligament was also calculated, and the results are provided in Table F.2 for the original equations (with e=0.339). The length of the edge of a node should be larger than the diameter of a ligament; thus, it should be true that $r/a>2$. The results in Table F.2 show this is not always the case for the original model. Moreover, using the corrected model, this geometric constraint is met even less often than by the original equations. Thus, when the model—corrected or original—is tuned to data by adjusting e, a geometrically impossible result manifests.

Table F.1: Fully corrected Boomsma-Poulikakos model predictions compared to data from reference [3], with e=0.198 to minimize RMS error

Porosity	k_{eff} ($Wm^{-1}K^{-1}$)		Relative Error	k_{eff} ($Wm^{-1}K^{-1}$)		Relative Error
	Experiment (Air)	Prediction (Air)		Experiment (Water)	Prediction (Water)	
0.905	6.7	11.9	0.778	7.65	13.8	0.803
0.906	6.9	11.8	0.710	7.65	13.7	0.786
0.909	6.7	11.5	0.710	7.6	13.3	0.743
0.937	4.5	8.47	0.883	5.35	9.67	0.808
0.946	4.6	7.51	0.632	5.4	8.55	0.584
0.949	3.95	7.18	0.817	4.875	8.17	0.677
0.952	3.9	6.84	0.755	4.75	7.79	0.641
0.971	2.7	4.54	0.681	3.7	5.24	0.416
0.972	2.5	4.40	0.761	3.3	5.10	0.544
0.978	2.2	3.54	0.609	3.05	4.19	0.372

Table F.2 Ratio of the node length to the radius of the ligament

Porosity	Using equations from [6] (*e*=0.339)	
	d	*e/d=r/a*
0.905	0.307	1.10
0.906	0.305	1.11
0.909	0.299	1.13
0.937	0.236	1.44
0.946	0.211	1.61
0.949	0.202	1.68
0.952	0.193	1.76
0.971	0.120	2.84
0.972	0.114	2.97
0.978	0.0761	4.45

Extending the model to account for ligament orientation dramatically improves the prediction. The original equations from reference [6] predict the measured data of reference [3] with relative RMS errors of about 43% for air, 31% for water and 38% for all the data. When the geometric and algebraic errors in those equations are corrected (i.e., using d from Eq. F.7b, but not accounting for ligament orientation), the predictions are even worse, with a relative RMS error of about 70%. The new model accounting for ligament orientation provides predictions with a relative RMS deviation of less than 12.2% for all the data. The extended version of the Boomsma-Poulikakos model, adopting Eq. (F.20) which accounts for ligament orientation is an improvement over the original model (corrected or not). In spite of the improved predictions of k_{eff}, the ratio of node length to ligament radius was also less than 2 for the extended model. This result may be caused by the use of the tetradecahedron unit cell. Variations in foam geometry have been discussed [7-10], and Gabbrielle [7] developed a polyhedral model that combines ten 14-hedra and four 13-hedra to closely match real foams found experimentally. The extension proposed in the current paper to account for ligament orientation could be applied to any of those alternative geometrical models.

F.4 Conclusions

As originally presented [6], the Boomsma-Poulikakos model of the effective thermal conductivity of fluid-saturated metal foam contains errors. However, even when those errors are corrected, the approach fails to provide predictions consistent with reported data. It is reasonable to conjecture that the volume-fraction-weighting of thermal conductivities is the root cause of the failure of this approach. Correcting that approach to account for ligament orientation provides improved predictions of effective thermal conductivity.

F.5 References

[1] X. Han, Q. Wang, Y. Park, C. T'Joen, A. Sommers, A. M. Jacobi, A review of metal foam and metal matrix composites for heat exchangers and heat sinks, International Journal of Refrigeration, 2009. (sub judice)

[2] Z. Dai, K. Nawaz, Y. Park, Q. Chen, A. M. Jacobi, A comparison of metal-foam heat exchangers to compact multi-louver designs for air-side heat transfer applications, Proceedings of the Seventh International Conference on Enhanced, Compact and Ultra-Compact Heat Exchangers: From Microscale Phenomena to Industrial Applications, San Jose, Costa Rica, 2009, pp.49-57.

[3] V.V. Calmidi, R.L. Mahajan, The effective thermal conductivity of high porosity fibrous metal foams, Journal of Heat Transfer 121(1999) 466-471.

[4] A. Bhattacharya, V.V. Calmidi, R.L. Mahajan, Thermophysical properties of high porosity metal foams, International Journal of Heat and Mass Transfer 45(2002)1017-1031.

[5] Ramvir Singh, H.S. Kasana, Computational aspects of effective thermal conductivity of highly porous metal foams, Applied Thermal Engineering 24(2004) 1841-1849.

[6] K. Boomsma, D. Poulikakos, On the effective thermal conductivity of a three-dimensionally structured fluid-saturated metal foam, International Journal of Heat and Mass Transfer 44(2001)827-836.

[7] R. Gabbrielli, A new counter-example to Kelvin's conjecture on minimal surfaces,

Philosophical Magazine Letters 89(2009) 483-491.

[8] R.M. Sullivan, L.J. Ghosn, B.A. Lerch, A general tetrakaidecahedron model for open-celled foams, International Journal of Solids and Structures 45(2008) 1754-1765.

[9] S. Ross, H.F. Prest, On the morphology of bubble clusters and polyhedral foams, Colloids and Surfaces 21 (1986) 179-192.

[10] R.E. Williams, Space-filling polyhedron: Its relation to aggregates of soap bubbles, plant cells, and metal crystallites, Science 161 (1968) 276-277.

Appendix G: A comparison of metal-foam heat exchangers to louver-fin designs

Authors: Zhengshu Dai, Kashif Nawaz, Young-Gil Park, Qi Chen, Anthony Jacobi

Abstract

High porosity metal foams, with novel thermal, mechanical, electrical, and acoustic properties are being more widely used in various industrial applications. In this paper, open-cell aluminum foam is considered as a highly compact replacement for conventional louver fins in brazed aluminum heat exchangers. A model, based on the ε-N_{TU} method, is developed to compare the flat-tube, serpentine louver-fin heat exchanger to the flat-tube metal-foam heat exchanger. The two heat exchangers are subjected to identical thermal-hydraulic requirements, and volume, mass, and cost of the metal-foam and louver-fin designs are compared. The results show that the same performance is achieved using the metal-foam heat exchanger but a lighter and smaller heat exchanger is required. However, the cost of the metal-foam heat exchanger is currently much higher than that of the louver-fin heat exchanger, because of the high price of metal foams. If the price of metal foam falls to equal that of louver-fin stock (per unit mass), then the metal-foam heat exchanger will be less expensive, smaller and lighter than the louver-fin heat exchanger with identical thermal performance.

Nomenclature

A	total heat-transfer surface area (m^2)
A_c	flow cross-sectional area of the tube (m^2)
$A_\mathrm{c}^{'}$	cross-sectional fin area (m^2)
A_f	fin surface area (m^2)
A_min	minimum cross-sectional area for air flow (m^2)
C	heat capacity rate (W K^{-1})
C_r	heat capacity ratio
c_p	fluid specific heat at constant pressure (J kg^{-1} K^{-1})
D_h	hydraulic diameter (m)
d_f	fiber diameter (m)
d_p	pore diameter (m)
F_d	fin depth (m)
F_l	fin length (m)
F_p	fin spacing (m)
f	Fanning friction factor
ff	inertial coefficient
f_app	apparent Fanning friction factor
f_cor	Fanning friction factor correlation
f_{Re}	correlation factor for Reynolds number
G_c	air mass flux at A_min (kg m^{-1} s^{-1})
H	heat exchanger height (m)

h	convective heat transfer coefficient (W m^{-2} K^{-1})
j	Colburn j -factor
j_{cor}	Colburn- j factor correlation
j_{louver}	correlation factor for louver geometry effect
j_{low}	correlation factor for low-Reynolds-number effect
j_{Re}	correlation factor for Reynolds-number effect
K	permeability (m^2)
K_{c}	entrance pressure-loss coefficient
K_{e}	exit pressure-loss coefficient
k_{a}	air thermal conductivity (W m^{-1} K^{-1})
k_{f}	thermal conductivity of the fin (W m^{-1} K^{-1})
k_{se}	solid-phase effective thermal conductivity (W m^{-1} K^{-1})
L	the length of a straight fin (m)
L_{l}	louver length (m)
L_{p}	louver spacing (m)
M	mass of heat exchangers (kg)
m	fin parameter (m^{-1})
$\dot{m}$	mass flow rate (kg s^{-1})
N_{LB}	number of louver banks
N_{TU}	number of transfer units
Nu	Nusselt number
P	fan power (W)
$P^{'}$	fin perimeter (m)
Pr	Prandtl number
ΔP	air-side pressure drop across heat exchanger (Pa)

ΔP_f	fluid static pressure drop in the flow direction between two cross sections of interest (Pa)
ΔP^*	dimensionless fluid static pressure drop
q	heat transfer rate (W)
q_{max}	the maximum possible heat transfer rate (W)
Re_D	Reynolds number based on hydraulic diameter
Re_{Lp}	Reynolds number based on louver pitch
Re_{df}	Reynolds number based on fiber diameter
R_{wall}	tube wall conduction resistance (K W^{-1})
T	fluid temperature (C)
T_{p}	tube spacing (m)
UA	overall heat transfer conductance (W K^{-1})
u	velocity (m s^{-1})
u_{m}	mean fluid velocity over the tube cross section (m s^{-1})
V	volume of heat exchangers (m^3)
W	wetted perimeter (m)
X	heat exchanger width (m)
$x_{\mathrm{fd,\,h}}$	hydrodynamic entry length (m)
$x_{\mathrm{fd,t}}$	thermal entry length (m)
x^*	dimensionless axial coordinate for the thermal entrance region
x^+	dimensionless axial coordinate for the hydrodynamic entrance region
Y	air-side flow depth (m)

Greek symbols

α	louver angle, rad in Eqs.(G.14a) and (G.17a)
β	air-side surface-area-to-volume ratio (m^{-1})
δ_f	fin thickness (m)
ε	heat exchanger effectiveness
η_0	the overall surface efficiency
η_f	the efficiency of a single fin
μ	dynamic viscosity (kg m^{-1} s^{-1})
ρ	density (kg $\mathrm{m}^{-3-)}$
σ	area contraction ratio

Subscripts

a	air
foam	metal-foam
lam	laminar flow
louv	louvered-fin
m	mean
prs	porous
ratio	ratio of metal-foam to louvered-fin design
w	water
1	inlet
2	outlet

G.1 Introduction

Metal foams are porous media with low density and novel thermal, mechanical, electrical, and acoustic properties [1]. They can be categorized as open-cell or closed-cell foams, but only open-cell metal foams appear to have promise for constructing heat exchangers. Open-cell metal foams have high specific surface area, relatively high thermal conductivity, and a tortuous flow path to promote mixing. A number of researchers have studied metal foams for thermal applications; some were focused on metal-foam heat exchangers (and heat sinks), and many others investigated the basic thermal transport properties of metal foams.

The basic properties of the metal foams include the effective thermal conductivity, permeability, and inertial coefficient. Calmidi and Mahajan [2] investigated the effective thermal conductivity of high-porosity fibrous metal foams experimentally and developed an empirical correlation and a theoretical model. The model predictions agreed closely with the experimental data and were used for the evaluation of metal foams as possible candidates for heat sinks in electronics cooling applications. Boomsma and Poulikakos [3] (see also [4]) developed a one-dimensional heat conduction model for use with open-cell metal foams, based on an idealized three-dimensional cell geometry of the foam. Their model showed that the fluid-phase conductivity has a relatively small effect on the effective thermal conductivity and the overall effective thermal conductivity of the metal foam is controlled by the solid-phase conductivity to a large extent. Bhattacharya *et al.* [5] conducted research on the determination of the effective thermal conductivity, permeability, and inertial coefficient of highly porous metal foams. A theoretical model was formulated and the analysis showed that the effective thermal conductivity depends strongly on the porosity and the ratio of the cross-sections of the fiber and the intersection, but no systematic dependence on pore density was found. Fluid flow experiments were conducted and the results showed that permeability increases with pore diameter and porosity of the medium, and the inertial coefficient depends only on porosity. They proposed a theoretical model for predicting inertial coefficient and a modified permeability model. The models were shown to agree with experimental results. Tadrist *et al.* [6] discussed the characteristics of randomly stacked fibers and metallic foams and analyzed the transport properties for both materials.

Convection in porous media has been widely investigated, but most studies focused on packed beds and granular materials with porosities in the range 0.3-0.6. The porosity of open-cell metal foams is much higher (ε >0.90), and only during the past decade has convection in high-porosity metal foams started to receive attention. Calmidi and Mahajan [7] investigated forced convection in high-porosity metal foams experimentally and numerically. Experimental results showed that the transport enhancing effect of thermal dispersion is extremely low with foam-air combinations, but for foam-water combinations it can be very high. In the numerical study, a thermal non-equilibrium model was used and a Nusselt number correlation was determined. Zhao *et al.* [8] studied natural convection and its effect on overall heat transfer in highly porous open-cell FeCrAlY foams experimentally and numerically. Experimental results showed that natural convection is significant in metal foams due to the high porosity and inter-connected open cells. Numerical calculations showed that the so-called non-equilibrium effect (the metal and fluid being at different temperatures) can not be neglected and hence a two-equation energy model should be used instead of one-equation model for convection in metal foams. Hetsroni *et al.* [9] studied natural convection heat transfer in metal foam strips with internal heat generation by experiments. Infrared images on both the surface and the inner region of the metal foam were analyzed, and the non-equilibrium temperature distribution was estimated. The result indicated that the non-equilibrium effect is significant.

Some studies have focused on metal-foam convective heat transfer devices. Boomsma *et al.* [10] studied an open-cell aluminum foam heat sink for electronics cooling applications. They found that compressed aluminum foams performed well, offering a significant improvement in the efficiency over several commercially available heat exchangers. They also found the metal foam can decrease the thermal resistance to nearly half that of currently used heat exchangers in the same application. Zhao *et al.* [11] and Lu *et al.* [12] analyzed forced convection heat transfer performance in high-porosity, open-cell, metal-foam-filled heat exchanger tubes and metal-foam-filled pipes using the Brinkman-extended Darcy momentum model and the two-equation heat transfer model for porous media. The results showed that, compared to conventional, finned-tube heat exchangers, the heat exchangers with metal-foam-filled tubes have better heat transfer performance, and the metal-foam-filled pipes have much better thermal performance than a plain tube, but at the expense of higher pressure drop. Mahjoob and Vafai [13] have discussed the effects of micro-structural metal foam properties on heat exchanger performance, and they categorized and investigated the extant correlations for flow and thermal transport in metal-foam heat exchangers. Tube and channel metal-foam heat exchangers were used to evaluate the performance of the heat exchangers, and the results showed a considerable improvement in performance by inserting the metal foam. Ejlali *et al.* [14] numerically investigated the fluid flow and heat transfer of an air-cooled metal-foam heat sink under a high speed laminar jet confined by two parallel walls at Reynolds numbers from 600 to 1000. They compared the performance of the metal-foam heat sink to that of conventional finned design and found that the heat removal rate can be greatly improved without additional cost.

In the open literature, there are numerous studies of material properties and transport phenomena, and fewer studies of metal-foam heat sinks. However, there are very few (if any) studies of metal-foam heat exchangers in heating, air-conditioning, and refrigeration applications. Heat exchangers are important to the overall efficiency, cost, and size of such systems. Since high-porosity open-cell metal foam has been shown promising for heat transfer applications, there are sound reasons to explore the performance of heat exchangers with metal-foam fins for space-conditioning systems. In this study, a thermal-hydraulic performance model based on the ε-N_{TU} method was developed to compare the flat-tube, serpentine louver-fin heat exchanger with the novel flat-tube metal-foam heat exchanger. Based on the same performance (fan power and heat transfer rate), the volume, mass, and cost were compared.

G.2 Modeling

G.2.1 Heat Exchanger Configuration

A flat-tube, serpentine louver-fin heat exchanger configuration was selected from the literature as representative of the current state of the art for air-side heat exchanger design in HVAC&R systems [15]. The configuration is similar to that shown in Fig. G.1 and the geometrical description is provided in Table G.1.

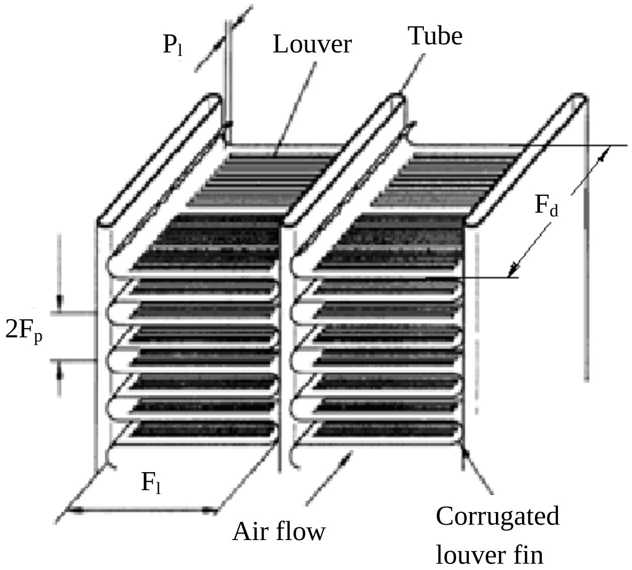

Figure G.1: Flat-tube heat exchanger with corrugated louver fins and rectangular air-flow channels (figure from Chang and Wang [16])

Table G.1: Geometrical description of flat-tube serpentine louver-fin heat exchanger

source	L_p (mm)	F_p (mm)	F_l (mm)	L_l (mm)	α (deg)	F_d (mm)	T_p (mm)	δ_f (mm)	N_{LB} (-)
Park and Jacobi [15] No.6	1.14	1.4	12.43	11.15	29	25.4	14.26	0.114	2

The air-side configuration of the flat-tube metal-foam heat exchanger is shown in Fig. G.2. The metal foam sample was selected from the study by Calmidi and Mahajan [7]. In their work, the material of the metal foam was aluminum alloy T-6201, but in the current model, the metal foam material is T-6101. Due to a small difference in the solid-phase thermal conductivity between these two materials, the solid-phase effective thermal conductivity of T-6101 metal foam was calculated using the model of Camidi and Mahajan [7]. The metal foam properties are provided in Table G.2.

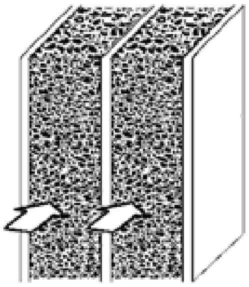

Figure G.2: Schematic illustration of air-side metal-foam fin geometry, which mimics the louver-fin arrangement in Fig. G.1. (adapted from Kim *et al.* [17])

Table G.2: Characteristics of the metal foam sample

source	Porosity (-)	PPI (-)	df (mm)	dp (mm)	ff (-)	K ($\times 10^7$m^2)	k_{se} (W/m k)
Calmidi and Mahajan [7] #6	0.9272	40	0.25	2.02	0.089	0.61	5.83

G.2.2 Methodology for Performance Modeling

From the effectiveness-NTU (ε-N_{TU}) method [18], the following equations were used for calculating heat transfer rate for both heat exchangers. The heat exchanger effectiveness ε is defined as:

$$\varepsilon = \frac{q}{q_{\max}} \tag{G.1}$$

where q_{max} is the maximum possible heat transfer rate,

$$q_{\max} = C_{\mathrm{a}}\left(T_{\mathrm{w},1} - T_{\mathrm{a},1}\right) \tag{G.2}$$

where the minimum heat capacity rate C_{a} is on the air side,

$$C_{\mathrm{a}} = \dot{m}_{\mathrm{a}} c_{p,\mathrm{a}} \tag{G.3}$$

The heat exchanger effectiveness relation is for a single pass, cross flow configuration with both fluids unmixed [18]:

$$\varepsilon = 1 - \exp\left[\left(\frac{1}{C_\mathrm{r}}\right)\left(N_{TU}\right)^{0.22}\left\{\exp\left[-C_\mathrm{r}\left(N_{TU}\right)^{0.78}\right]-1\right\}\right] \tag{G.4}$$

with

$$C_\mathrm{r} = (\dot{m}_\mathrm{a} c_{p,a}) / \left(\dot{m}_\mathrm{w} c_{p,\mathrm{w}}\right) \tag{G.5}$$

The number of transfer units (N_{TU}) was calculated using

$$N_{TU} = \frac{UA}{C_\mathrm{a}} \tag{G.6}$$

and

$$\frac{1}{UA} = \frac{1}{\left(\eta_0 hA\right)_\mathrm{a}} + R_\mathrm{wall} + \frac{1}{\left(\eta_0 hA\right)_\mathrm{w}} \tag{G.7}$$

The overall surface efficiency and fin efficiency, η_o and η_f, respectively in Eq. (G.7), were calculated using Eqs. (G.8) and (G.9). Here a one-dimensional fin with an adiabatic tip case was assumed for both the flat-tube, serpentine louver-fin heat exchanger and the flat-tube metal-foam heat exchanger.

$$\eta_0 = 1 - \frac{A_\mathrm{f}}{A}\left(1 - \eta_\mathrm{f}\right) \tag{G.8}$$

$$\eta_\mathrm{f} = \frac{\tanh(mL)}{mL} \tag{G.9}$$

where $m = \sqrt{\left(hP'\right)/\left(k_\mathrm{f} A_\mathrm{c}'\right)}$.

The fin efficiency calculation was modified to treat the metal foam, using the air-side surface-area-to-volume ratio β. Furthermore, because in this case, the air in the metal foam was not stagnant and the fluid-phase conductivity does not have a considerable impact on the effective thermal conductivity of the metal foam, the solid-phase-only effective thermal conductivity was taken as the effective thermal conductivity of the metal foam. Thus, the model becomes,

$$\beta = \frac{3\pi d_\mathrm{f}}{d_\mathrm{p}^2} \tag{G.10}$$

$$m_{\mathrm{prs}} = \sqrt{h \cdot \frac{\beta}{k_{\mathrm{se}}}} \tag{G.11}$$

$$\eta_{\mathrm{f,prs}} = \frac{\tanh\lfloor m_{\mathrm{prs}} \cdot F_{\mathrm{l,prs}} / 2 \rfloor}{m_{\mathrm{prs}} \cdot F_{\mathrm{l,prs}} / 2} \tag{G.12}$$

In this approach, we rely upon the findings of Calmidi and Mahajan [7] (see Table 2), with a simple extension of fin analysis to account for temperature variations in the metal foam. There are other treatments of foam heat transfer available in the literature (e.g., [19]); however, this current approach is especially well suited for the parametric study of heat exchanger performance undertaken in this work.

G.2.3 Air-side heat transfer and pressure drop

Using the definition of the Coburn- j factor, as given in Eq. (G.13), the Nusselt number and thus convective heat transfer coefficient of flat-tube, serpentine louver-fin at the air side can be obtained using the correlation by Park and Jacobi [20] as given below:

$$j = \frac{Nu}{RePr^{1/3}} \tag{G.13}$$

$$j_{\mathrm{cor}} = 0.872 j_{Re} j_{\mathrm{low}} j_{\mathrm{louver}} \alpha^{0.219} N_{\mathrm{LB}}^{-0.0881} \left(\frac{F_{\mathrm{l}}}{L_{\mathrm{p}}}\right)^{0.149} \left(\frac{F_{\mathrm{d}}}{F_{\mathrm{p}}}\right)^{-0.259} \left(\frac{L_{\mathrm{l}}}{F_{\mathrm{l}}}\right)^{0.54} \left(\frac{F_{\mathrm{l}}}{T_{\mathrm{p}}}\right)^{-0.902} \left(1 - \frac{\delta_{\mathrm{f}}}{L_{\mathrm{p}}}\right)^{2.62} \left(\frac{L_{\mathrm{p}}}{F_{\mathrm{p}}}\right)^{0.301} \tag{G.14a}$$

$$j_{Re} = \mathrm{Re}_{L_p}^{\left[-0.458 - 0.00874 \cosh\left(F_p / L_p - 1\right)\right]} \tag{G.14b}$$

$$j_{\mathrm{low}} = 1 - \sin\left(\frac{L_{\mathrm{p}}}{F_{\mathrm{p}}} \alpha\right) \left[\cosh\left(0.049 \,\mathrm{Re}_{L_p} - 0.142 \frac{F_{\mathrm{d}}}{N_{\mathrm{LB}} F_{\mathrm{p}}}\right)\right]^{-1} \tag{G.14c}$$

$$j_{\mathrm{louver}} = 1 + 0.0065 \tan(\alpha) \left(\frac{F_{\mathrm{d}}}{N_{\mathrm{LB}} F_{\mathrm{p}}}\right) \cos\left[2\pi \left(\frac{F_{\mathrm{p}}}{L_{\mathrm{p}} \tan(\alpha)} - 1.8\right)\right] \tag{G.14d}$$

The air-side convective heat transfer coefficient for the flat-tube metal-foam heat exchanger was obtained from the work of Calmidi and Mahajan [7]. They reported good agreement between experimental data and the prediction given by the following equation.

$$h = 0.52 {Re_{df}}^{0.5} Pr^{0.37} \frac{k_{\mathrm{a}}}{d_{\mathrm{f}}} \tag{G.15}$$

where Re_{df} is the Reynolds number based on fiber diameter and the intrinsic average velocity (Darcy velocity/ porosity).

Using the Fanning friction factor defined by Eq. (G.16), the air-side pressure drop of the flat-tube, serpentine louver-fin heat exchanger can be calculated for a known friction factor and flow properties,

$$f = \frac{A_{\mathrm{min}}\rho_{\mathrm{a},m}}{A\rho_{\mathrm{a},1}}\left[\frac{2\rho_{\mathrm{a},1}\Delta P}{G_c^2} - \left(K_{\mathrm{c}} + 1 - \sigma^2\right) - 2\left(\frac{\rho_{\mathrm{a},1}}{\rho_{\mathrm{a},2}} - 1\right) + \left(1 - \sigma^2 - K_{\mathrm{e}}\right)\frac{\rho_{\mathrm{a},1}}{\rho_{\mathrm{a},2}}\right] \tag{G.16}$$

The entrance and exit loss coefficients, K_c and K_e were evaluated at $Re=\infty$ from Kays and London [21], and the correlation for flat-tube, serpentine louver-fin heat exchangers by Park and Jacobi [20] was used to calculate the friction factor:

$$f_{\mathrm{cor}} = 3.69 f_{Re} N_{\mathrm{LB}}^{-0.256}\left(\frac{F_{\mathrm{p}}}{L_{\mathrm{p}}}\right)^{0.904}\sin(\alpha + 0.2)\left(1 - \frac{F_{\mathrm{l}}}{T_{\mathrm{p}}}\right)^{0.733}\left(\frac{L_{\mathrm{l}}}{F_{\mathrm{l}}}\right)^{0.648}\left(\frac{\delta_{\mathrm{f}}}{L_{\mathrm{p}}}\right)^{-0.647}\left(\frac{F_{\mathrm{l}}}{F_{\mathrm{p}}}\right)^{0.799} \tag{G.17a}$$

$$f_{Re} = \left(Re_{L_p}\frac{F_{\mathrm{p}}}{L_{\mathrm{p}}}\right)^{-0.845} + 0.0013\,\mathrm{Re}_{L_p}^{\left[1.26\left(\delta_{\mathrm{f}}/F_{\mathrm{p}}\right)\right]} \tag{G.17b}$$

For the flat-tube metal-foam heat exchanger, the air-side pressure drop was calculated following Bhattacharya *et al*. [5], with *ff* and *K* provided in Table 2:

$$-\frac{dp}{dx} = \frac{\mu u}{K} + \frac{\rho_{\mathrm{a}} ff}{\sqrt{K}} u^2 \tag{G.18}$$

Equation (G.18) is widely accepted for steady-state, unidirectional pressure drop in a homogeneous, uniform, and isotropic porous medium, for the incompressible flow of a Newtonian fluid.

G.2.4 Tube-side heat transfer and pressure drop

For the purpose of this comparison, the tube-side flow was taken to be water, which is representative of systems with a secondary loop. Were the comparison undertaken with a refrigerant undergoing a tube-side phase change, the reduced tube-side pressure drop and thermal resistance would magnify the air-side differences between the louver-fin and the metal-foam heat exchangers. The Reynolds number is based on hydraulic diameter,

$$Re_D = \frac{\rho_{\mathrm{w}} u_{\mathrm{m}} D_h}{\mu} \tag{G.19}$$

where for a noncircular tube, $D_h = 4A_c/W$, with A_c the cross-sectional flow area and W the wetted perimeter.

For the cases considered, the tube-side flow remains laminar. Again, were turbulent flows considered, the air-side differences would have even more impact. The hydrodynamic and thermal entry lengths are obtained from

$$\left(\frac{x_{\mathrm{fd,h}}}{D_h}\right)_{\mathrm{lam}} \approx 0.05 Re_D \tag{G.20}$$

and

$$\left(\frac{x_{\mathrm{fd,t}}}{D_h}\right)_{\mathrm{lam}} \approx 0.05 Re_D Pr \tag{G.21}$$

The flat tube was treated as a duct flow, and because the thermal conductivity of the metallic tube is high and the heat exchanger was taken to be in crossflow, a uniform wall temperature was assumed. Again, this approach is conservative, because a constant-heat-flux boundary condition gives a higher tube-side Nusselt number. The flow inside the tube was divided into regions of simultaneously developing flow, thermally developing flow, and fully developed flow. The mean Nusselt numbers and friction factors in each region were calculated from Kakac *et al.* [22] for $x_h^* = x_{\mathrm{fd,h}}/(D_h Re_D Pr)$ and $x_t^* = x_{\mathrm{fd,t}}/(D_h Re_D Pr)$:

- for simultaneously developing flow（$0.1 < Pr < 1000$）

$$Nu_{\mathrm{m,T}} = 7.55 + \frac{0.024 x_h{*}^{(-1.14)}}{1 + 0.0358 Pr^{0.17} x_h{*}^{(-0.64)}} \tag{G.22}$$

- for thermally developing flow

$$Nu_{\mathrm{m,T}} = 1.849 x_t{*}^{(-1/3)} \qquad \text{for} \quad x_t{*} \le 0.0005 \tag{G.23a}$$

$$Nu_{\mathrm{m,T}} = 0.6 + 1.849 x{*}^{(-1/3)} \qquad \text{for} \quad 0.0005 < x_t{*} \le 0.006 \tag{G.23b}$$

$$Nu_{\mathrm{m,T}} = 7.541 + 0.0235 / x_t{*} \qquad \text{for} \quad x_t{*} > 0.006 \tag{G.23c}$$

- for fully developed flow

$$Nu_{\mathrm{m,T}} = 7.541 \tag{G.24}$$

When the friction factors for each region were calculated, simultaneously developing flow was treated as hydrodynamically developing flow, while thermally developing flow and fully developed flow were treated as fully developed flow. With $x^+ = x_h^* Pr$ and $\Delta P^* = 2\Delta P_f/(\rho_w u_m^2)$, the appropriate equations are as follows:

- for fully developed flow

$$f \cdot Re_D = 24 \tag{G.25}$$

- for hydrodynamically developing flow

$$f_{\mathrm{app}} \cdot Re_D = \frac{3.44}{x^{+(0.5)}} + \frac{24 + \dfrac{0.674}{4x^+} - \dfrac{3.44}{x^{+(0.5)}}}{1 + 0.000029 x^{+(-2)}} \tag{G.26a}$$

$$f_{\mathrm{app}} \cdot \mathrm{Re}_D = \frac{\Delta P^*}{4x^+} \tag{G.26b}$$

G.3 Results and discussion

The following physical parameters are taken as known for the purpose of comparison: air and water mass flow rates and inlet temperatures, m_a, m_w, $T_{a,1}$, and $T_{w,1}$, respectively, along with the flat-tube, serpentine louver-fin heat exchanger geometry. Both the louver-fin and metal-foam heat exchangers are taken to be made of aluminum alloy (6101).

The comparison is undertaken by calculating the fan power and heat transfer rate for the louver-fin heat exchanger under the prescribed operating conditions, and then calculating the flow depth and face area required for the metal-foam heat exchanger to match the thermal-hydraulic performance of the louver-fin heat exchanger. In particular, the metal-foam flow depth is decreased and tube length (heat exchanger width, X) is increased, until the fan power and heat transfer rate match those of the louver-fin heat exchanger. This comparison is repeated for varying tube pitch (fin length[1]) for the metal-foam heat exchanger, and the entire procedure is repeated for varying operating conditions. A cost comparison and the effects of parametric changes are discussed in the remainder of this section.

G.3.1 Effect of metal-foam fin length

By changing the tube pitch of the metal foam heat exchanger, the fin length F_l is changed; thus, the metal foam fin length is changed. For an operating condition of $T_{a,I}$=30 °C, $T_{w,I}$=60 °C, m_a=0.3 kg/s, m_w=0.1 kg/s, and a heat exchanger height, width and air-flow depth of H=X=360 mm, and Y=25.4 mm (for the louver-fin heat exchanger, Y=F_d), respectively, with the louver geometry given in Table 1, the fan power is 7.4 W and heat transfer rate is 5095 W for the louver-fin heat exchanger. Matching these fan power and heat transfer rate using a metal-foam heat exchanger at various metal-foam fin lengths produced the results shown in Fig. G.3. Over a fin-length range 8 mm to 20 mm, the ratio of the mass of the metal-foam heat exchanger to that of the louver-fin heat exchanger, M_{ratio}, increases with metal-foam fin length. In this range of fin length, the metal-foam heat exchanger always meets the performance of the louver-fin heat exchanger with less material use. From Fig. G.3 it can be seen that the tube length and the air-side flow depth of the metal-foam heat exchanger increase with increasing the metal-foam fin length. Thus, the heat exchanger volume ratio, V_{ratio} increases with fin length. With increasing fin length, the fin efficiency decreases, leading to reduced heat transfer per mass or volume of the heat exchanger; therefore, a larger heat exchanger is required to meet the heat duty. Nevertheless, for these conditions, the volume of the metal-foam heat exchanger is smaller than that of louver-fin heat exchanger over most of the fin-length range.

In order to compare heat exchanger costs, louver fin stock was assigned a cost of \$7/kg, metal

---

[1] For the metal-foam heat exchanger, the fin length is the tube pitch minus a tube thickness.

foam was assigned a cost of \$466/kg, and tubing cost \$5/kg. A fixed brazing cost of \$30 was assumed for each heat exchanger. Figure G.4 shows the cost variation with changing metal-foam fin length. Since the dimensions of the louver-fin heat exchanger were fixed, its cost is also fixed. For these conditions, the cost of the louver-fin heat exchanger is \$38, while the cost for a metal-foam heat exchanger varies from \$174 to \$357 with increasing metal-foam fin length.

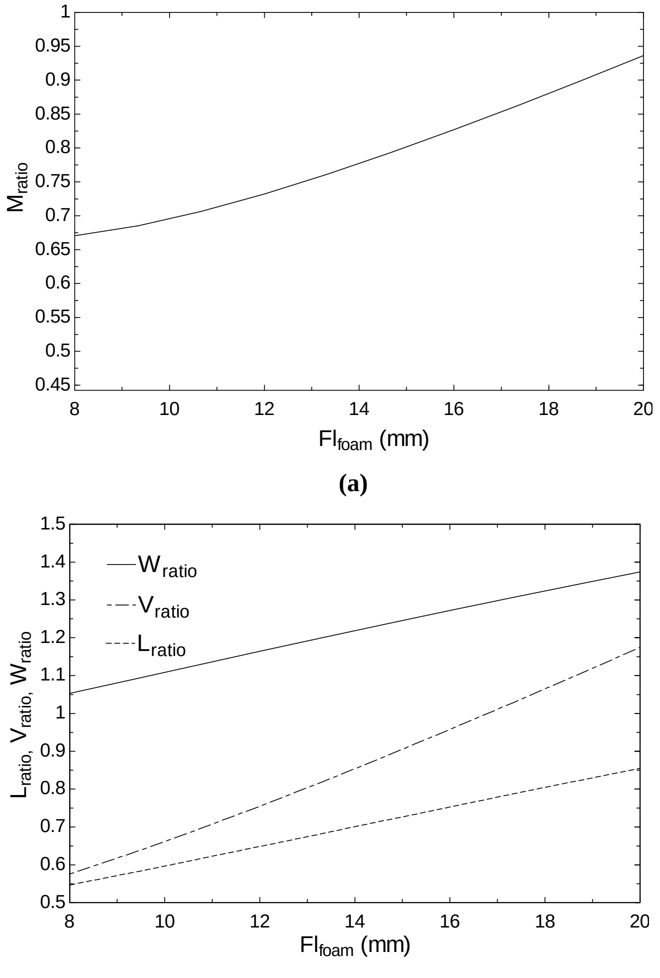

(a)

(b)

Figure G.3: The effect of metal-foam fin length on (a) mass and (b) dimensions, for a fixed louver-fin design

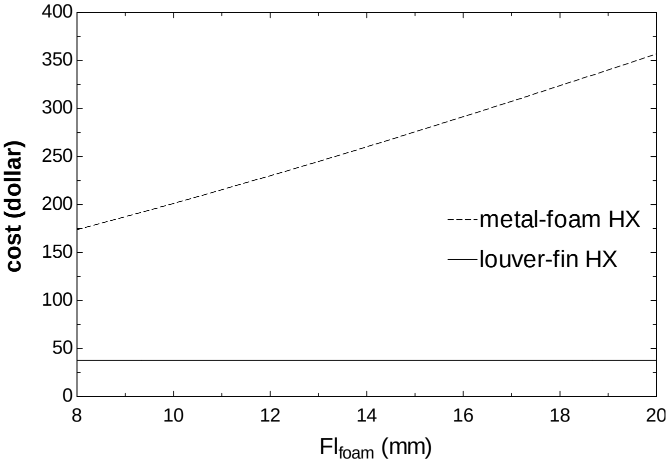

Figure G.4: Effect of fin length on the cost of heat exchangers

With advances in manufacturing techniques, and in mass production, the cost of metal foam is expected to be significantly lower than its current cost. Because the current cost of the metal-foam heat exchanger is dominated by material cost, it is useful to explore how the costs change as the metal foam becomes cheaper. Were the cost of the metal foam reduced to $7/kg (equal to louver fin stock), then the metal-foam heat exchanger would cost $35 for an 8 mm fin length. The two heat exchangers would have equal prices when the metal foam cost is $16/kg. These estimations are approximate and specific to the conditions considered. Nevertheless, they are helpful in understanding the costs and can be refined and tailored to other designs.

G.3.2 Effect of air mass flow rate

For a fixed louver-fin heat exchanger design, the effect of air mass flow rate on fan power and heat transfer rate is shown in Fig. G.5. In Fig. G.5, the cost of a metal-foam heat exchanger with the same thermal-hydraulic performance is shown. For this comparison, a metal-foam fin length of 8 mm was adopted. The range of air mass flow rate in these plots corresponds to a frontal velocity from 0.5 m/s to 3 m/s for the louver-fin heat exchanger, and from 0.7 m/s to 2.6 m/s for the metal-foam heat exchanger. The fan power and heat transfer rate increase with increasing air flow rate, and the increase in fan power is larger than the increase in heat transfer rate. The fan power increases from 0.3 W to 19.2 W, while the heat transfer rate increases from 1890 W to 6011 W. For a fixed cost of $38 for the louver-fin heat exchanger, a metal-foam heat exchanger with matching thermal-hydraulic performance has a cost that ranges from \$113 to \$181. In the low air mass flow rate range, the cost of the metal-foam heat exchanger increases faster than at high mass flow rates. The reason for this is because the air flow pattern in the louver-fin design undergoes a transition (from duct-directed to louver-directed flow) at low Reynolds numbers [15], and the accompanying rapid increase in heat transfer coefficient is reflected by the *j*-factor correlation [20]. The metal-foam heat exchanger does not have a flow-pattern change, thus, at low air mass flow rates, as the heat transfer coefficient increases rapidly with air flow for the louver-fin design, the metal-foam design does not enjoy such an increase, and in order to match the increase in louver-fin thermal performance more heat transfer area is need—added metal foam is added cost. It is also interesting to note that the cost of the metal-foam heat exchanger becomes roughly constant at high air flow rates. So the metal-foam heat exchanger is more competitive at low air mass flow rates; in particular the metal-foam heat exchanger is more competitive at flow rates below that at which the flow pattern transition occurs in the louver-fin heat exchanger.

G.3.3 Effect of water mass flow rate

The performance of the baseline, louver-fin heat exchanger is primarily governed by the air-side thermal resistance, and changing the water mass flow rate over a range of 0.1 kg/s to 1 kg/s results in a heat transfer increase of about 25%; moreover, such a change does not impact the air-side fan power at all, and clearly fan power plays a key role in the metal-foam heat exchanger design. Thus, as expected, changing the water mass flow rate does not have a significant effect on the cost of the metal-foam heat exchanger.

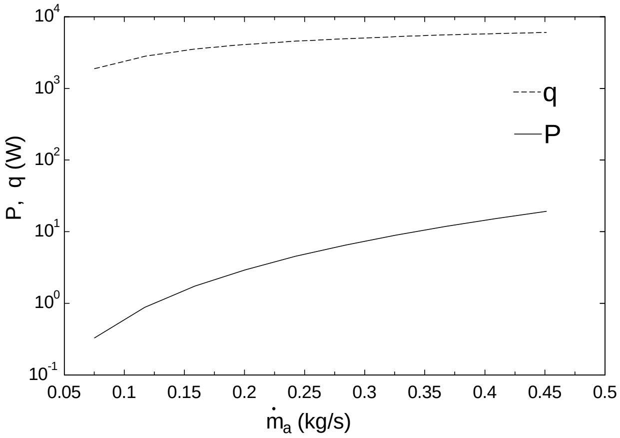

(a)

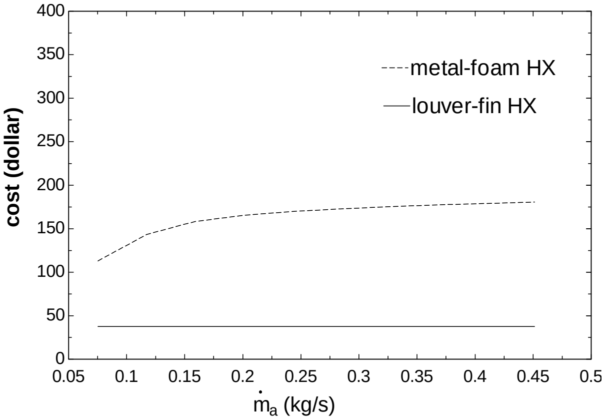

(b)

Figure G.5: Effect of air mass flow rate on (a) fan power, heat transfer rate and (b) cost

G.3.4 Effect of inlet temperature of air and water

Changing the fluid inlet conditions can result in rather large changes in the heat transfer rate, with virtually no change in air-side fan power. Nevertheless, the cost of the metal-foam heat exchanger duplicating the louver-fin performance was insensitive to these changes. The reason for this is because the heat transfer changes are caused by the changes in q_{max}, not in changes to N_{TU}. Thus, in this case, the cost of metal-foam heat exchanger depends only on the change of pan power. These results underscore the importance of fan-power constraints on metal-foam heat exchanger design and strongly suggest that, in order to exploit the advantages of compactness and heat transfer performance of metal foams, designs to minimize fan power should be sought.

G.3.5 Sensitivity study

In order to examine the sensitivity of the analysis to the accuracy of the correlations, the air-side convective heat transfer coefficient and friction factor were multiplied by arbitrary factors *d* and *b*, respectively, and the cost was re-calculated. As there are few data in the literature upon which to base this analysis, a rather wide range of multiplier (0.5-2) was selected. The results in Fig. G.6 show the dependence of metal-foam heat exchanger cost on the heat transfer coefficient estimation. If the correlation of Eq. (G.15) is conservative (i.e., it underestimates the actual heat transfer coefficient), then the cost estimates are slightly inflated. On the other hand, if the correlation is overestimating the true value of the convective coefficient, then the cost estimates might be significantly low. On the other hand, as shown in Fig. G.6, the cost is less sensitive to the estimated pressure drop. With a 200% change in the friction factor, the results change only about ±7%.

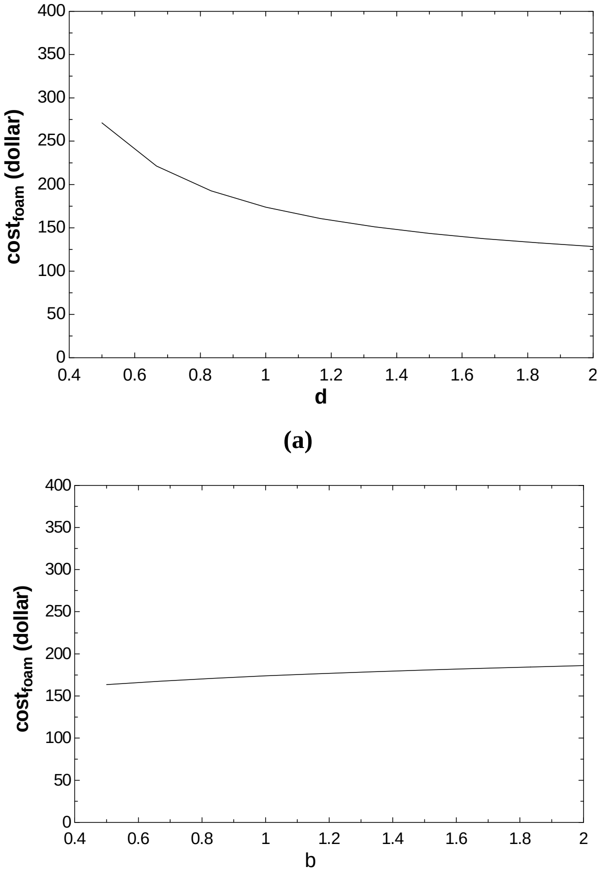

(a)

(b)

Figure G.6: Effect of (a) convective heat transfer coefficient (b) friction factor

G.4 Conclusions

In this study, analytical methods based on empirical correlations were used to compare a novel open-cell metal-foam heat exchanger to a conventional, flat-tube louver-fin heat exchanger. Comparisons of mass and volume as well as initial cost were undertaken. From the results, the following conclusions are drawn:

(1) For the same fan power and heat transfer rate, the metal-foam heat exchanger can be significantly smaller in volume and lighter in weight over a wide range of design space.

(2) If the price of metal foam is reduced to roughly \$16/kg (as opposed to ~\$466/kg currently), the cost of the louver-fin heat exchanger and the metal-foam heat exchanger will be equal for the baseline conditions of this study. The exact price at which cost equivalence is achieved will depend on the design conditions, but this figure can be considered to be a reasonable estimate for the air-to-liquid and air-to-refrigerant applications close to those of this study.

(3) The air and water inlet temperatures and water mass flow rate have little impact on the cost of a metal-foam heat exchanger matching the performance of the louver-fin heat exchanger.

(4) The cost of flat-tube metal-foam heat exchanger is sensitive to the convective heat transfer coefficient of the metal foam. Further experimental work is required before more refined cost estimates can be pursued.

G.5 References

[1] Lu, T., Ultralight porous metals: from fundamentals to applications, *Acta Mechanica Sinica, Chinese J. Mech*, vol.18, pp.457-479, 2002.

[2] Calmidi, V.V, and Mahajan, R.L., The effective thermal conductivity of high porosity fibrous metal foams, *J. Heat Transfer*, vol. 121, pp. 466-471, 1999.

[3] Boomsma, K., and Poulikakos, D., On the effective thermal conductivity of a three-dimensionally structured fluid-saturated metal foam, *Int. J. Heat Mass Transfer*, vol.44, pp.827-836, 2001.

[4] Dai, Z., Nawaz, K., Park, Y., Bock, J., and Jacobi, A.M., Correcting and extending the

Boomsma-Poulikakos effective thermal conductivity model for three-dimensional, fluid-saturated metal foams, *Int. Comm. Heat Mass Trans.*, in press.

[5] Bhattacharya, A., Calmidi, V.V., and Mahajan, R.L., Thermophysical properties of high porosity metal foam, *Int. J. Heat Mass Transfer*, vol. 45, pp.1017-1031, 2002.

[6] Tadrist, L., Miscevic, M., Rahli, O., and Topin, F., About the use of fibrous materials in compact heat exchangers, *Experimental Thermal and Fluid Science*, vol.28, pp. 193-199, 2004.

[7] Calmidi, V.V., and Mahajan, R.L., Forced convection in high porosity metal foams, *J. Heat Transfer*, vol.122, pp.557–565, 2000.

[8] Zhao, C.Y., Lu, T.J., and Hodson, H.P., Natural convection in metal foams with open cells, *Int. J. Heat Mass Transfer*, vol.48, pp.2452-2463, 2005.

[9] Hetsroni, G., Gurevich, M, and Rozenblit, R., Natural convection in metal foam strips with internal heat generation, *Experimental Thermal and Fluid Science*, vol. 32, pp. 1740-1747, 2008.

[10] Boomsma, K., Poulikakos, D., and Zwick, F., Metal foams as compact high performance heat exchangers, *Mechanics of Materials,* vol.35, pp.1161-1176, 2003.

[11] Zhao, C.Y., Lu, W, and Tassou, S.A., Thermal analysis on metal-foam filled heat exchangers. Part Ⅱ: Tube heat exchangers, *Int. J. Heat Mass Transfer*, vol.49, pp.2762-2770, 2006.

[12] Lu, W., Zhao, C.Y., and Tassou, S.A., Thermal analysis on metal-foam filled heat exchangers. Part Ⅰ: Metal-foam filled pipes, *Int. J. Heat Mass Transfer*, vol.49, pp.2751-2761, 2006.

[13] Mahjoob, S., and Vafai, K., A synthesis of fluid and thermal transport models for metal foam heat exchangers, *Int. J. Heat Mass Transfer*, vol.51, pp.3701-3711, 2008.

[14] Ejlali, A., Ejlali, A., Hooman, K., and Gurgenci, H., Application of high porosity metal foams as air-cooled heat exchangers to high heat load removal systems, *Int. Commun Heat Transf*, vol. 36, pp. 674-679, 2009.

[15] Park, Y., and Jacobi, A. M., The air-side thermal-hydraulic performance of flat-tube heat exchangers with louvered, wavy, and plain fins under dry and wet conditions, *J. Heat Transfer*, vol. 131, 061801, 2009.

[16] Chang, Y.J. and Wang, C.C., A generalized heat transfer correlation for louver fin geometry, *Int. J. Heat and Mass Transfer*, vol. 40, pp.533-544, 1997.

[17] Kim, S.Y., Paek, J.W., and Kang, B.H., Flow and heat transfer correlations for porous fin in a plate-fin heat exchanger, *J. Heat Transfer*, vol. 122, pp.572-578, 2000.

[18] Incropera, F.P., and DeWitt, D. P., Fundamentals of heat and mass transfer, 4th ed., *John Wiley & Sons, Inc*, 1996

[19] Dukhan, N., Picon-Feliciano, R., and Alvarez-Hernandez, A.R., Heat Transfer Analysis in Metal Foams with Low-Conductivity Fluids, *J. Heat Transfer*, vol. 128, pp. 784-792, 2006.

[20] Park, Y., Jacobi, A. M., Air-side heat transfer and friction correlations for flat-tube louver-fin heat exchangers, *J. Heat Transfer*, vol. 131, 021801, 2009.

[21] Kays, W. M., and London, A. L., Compact heat exchangers, 3rd ed., *McGraw-Hill*, New York, 1984

[22] Kakac, S., Shah, R.K., and Aung, W., Handbook of single-phase convective heat transfer, *John Wiley & Sons, Inc*, 1987.

Appendix H: Frost formation under natural convection

Aluminum foams

5 PPI

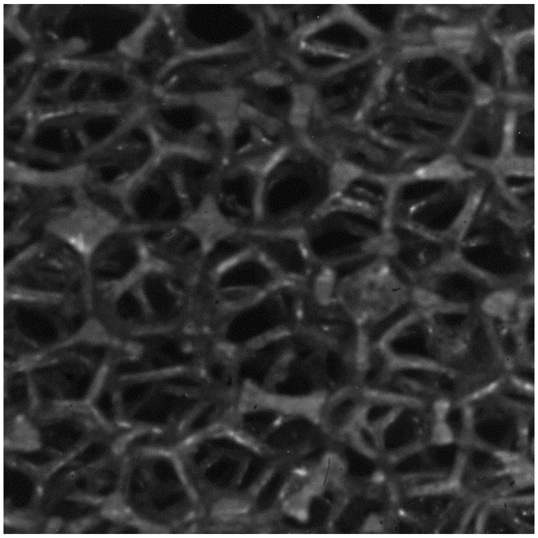

(0 mins)

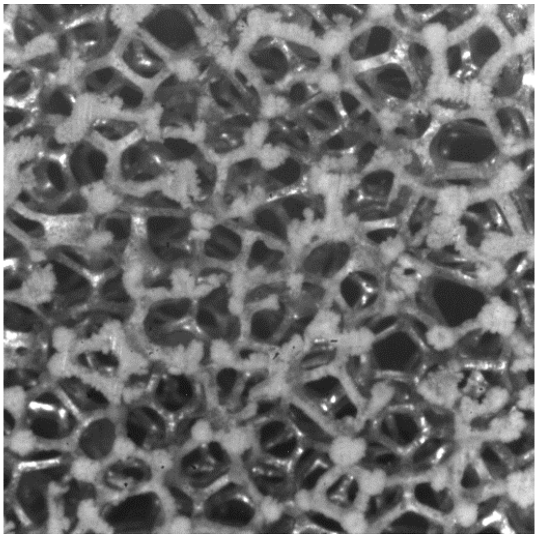

(15 mins)

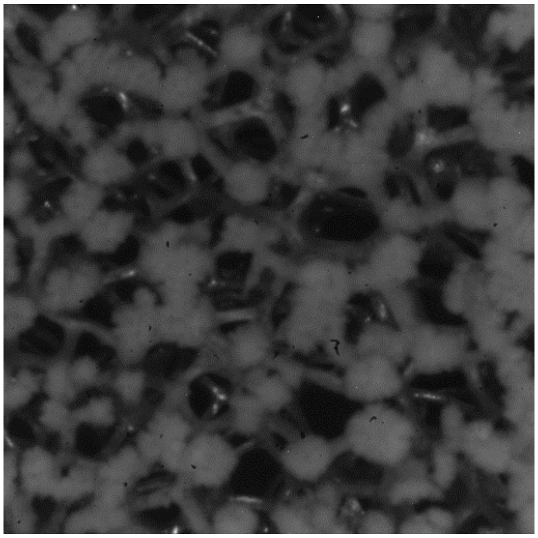

(30 mins)

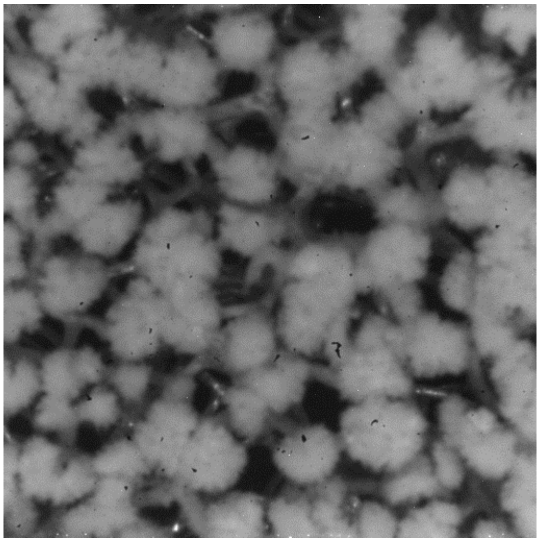

(45 mins)

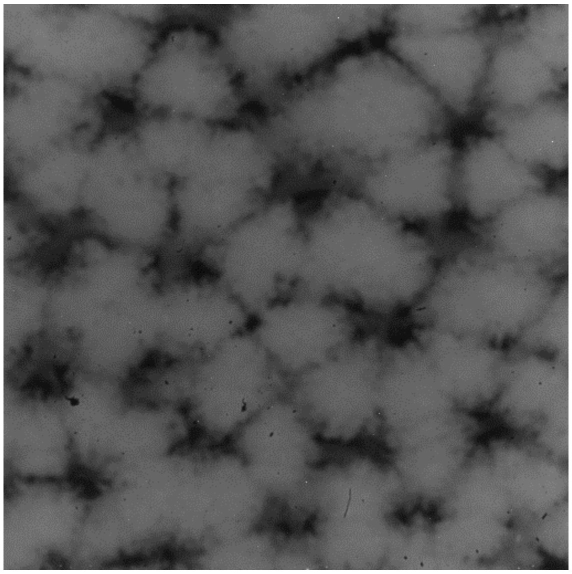

(60 mins)

10 PPI

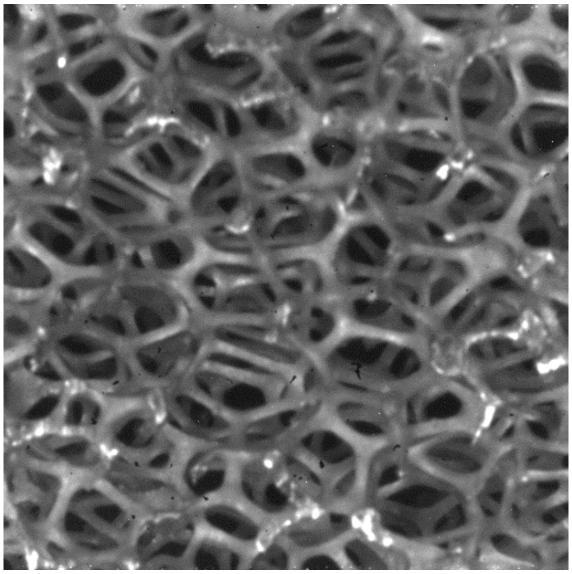

(0 mins)

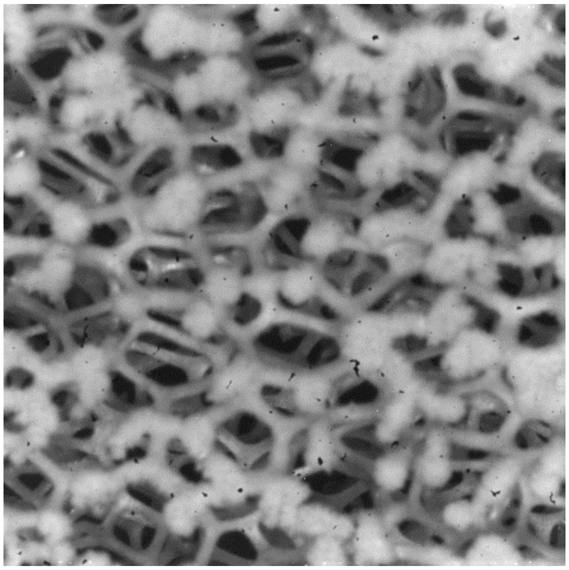

(15 mins)

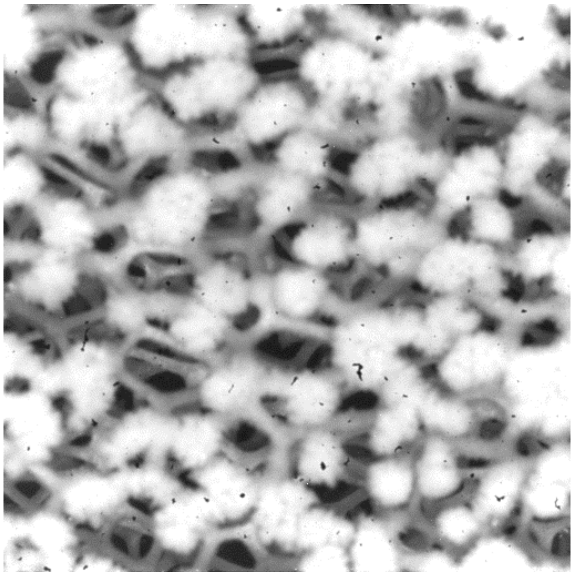

(30 mins)

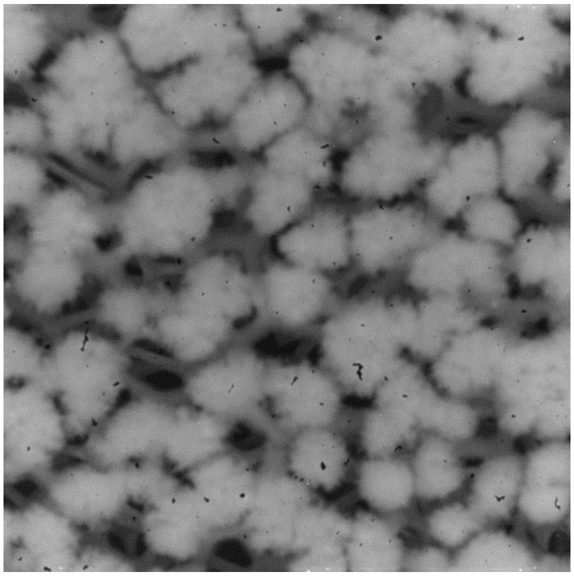

(45 mins)

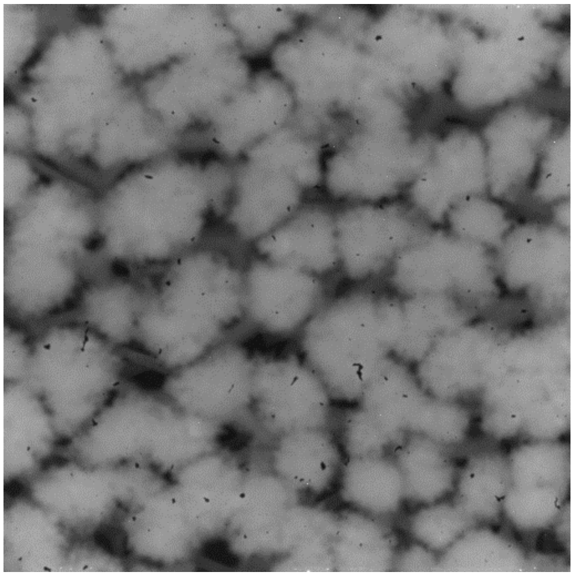

(60 mins)

20 PPI

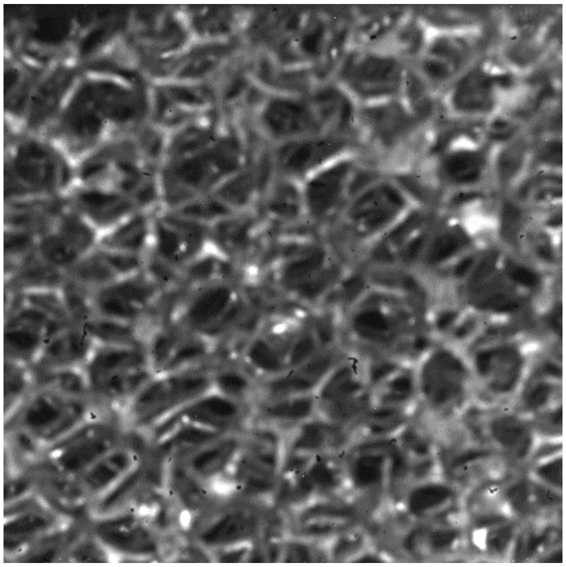

(0 mins)

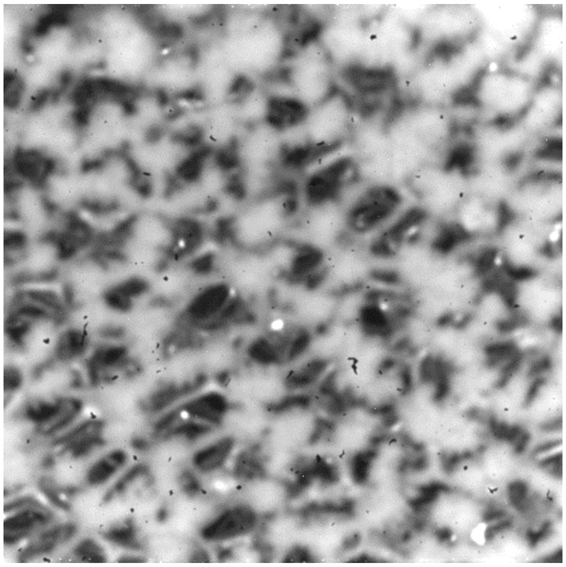

(15 mins)

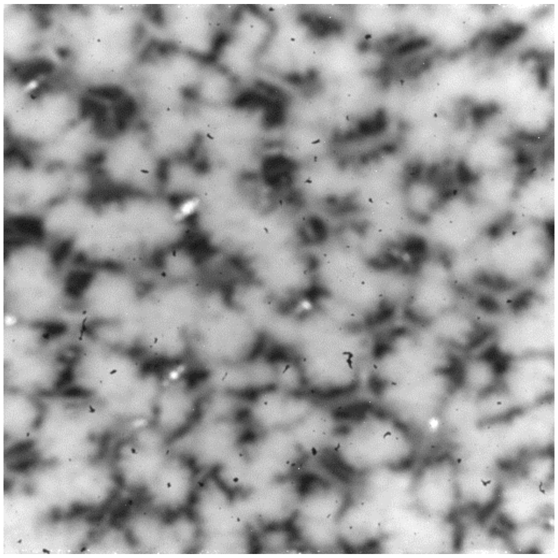

(30 mins)

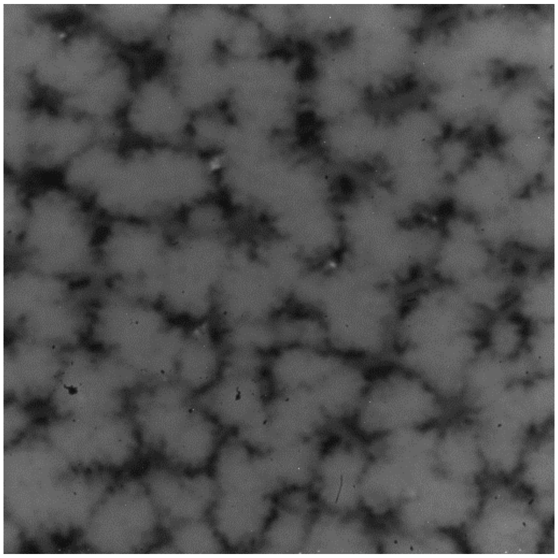

(45 mins)

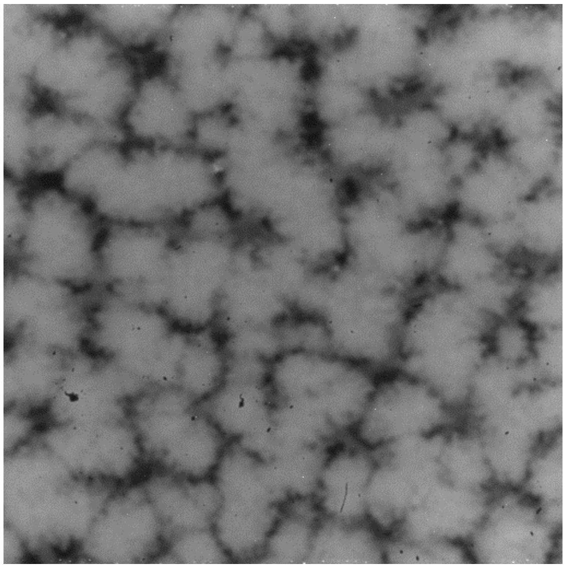

(60 mins)

Copper foams

10 PPI

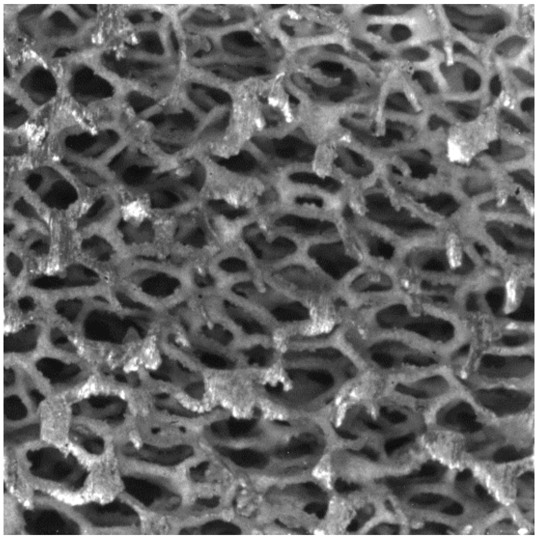

(0 mins)

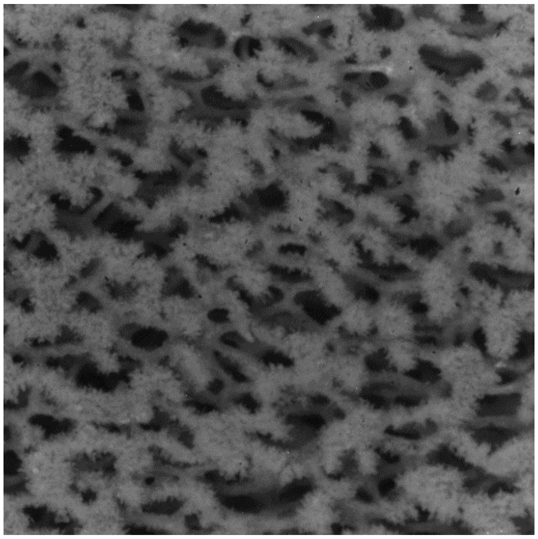

(15 mins)

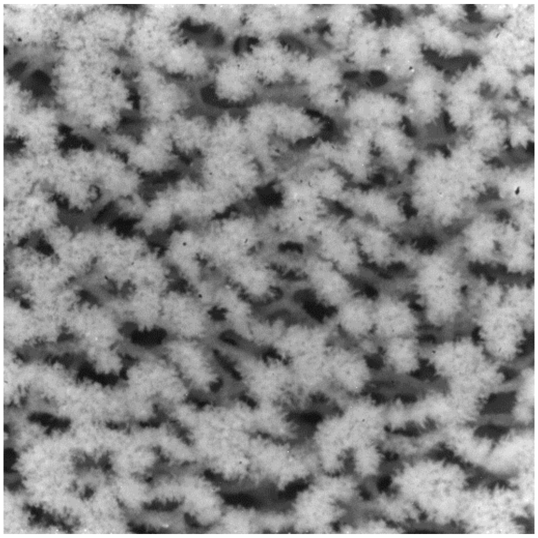

(30 mins)

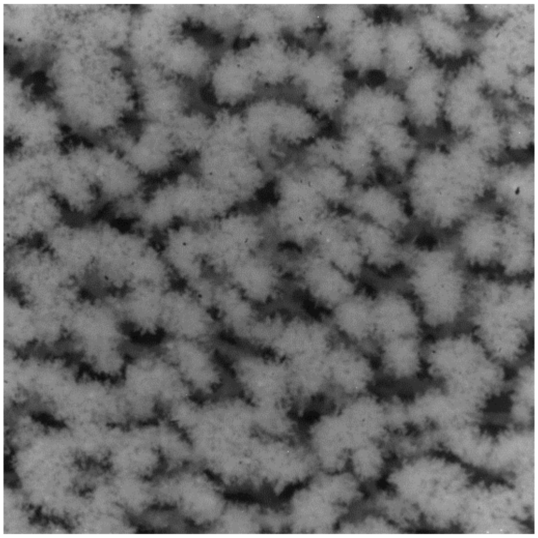

(45 mins)

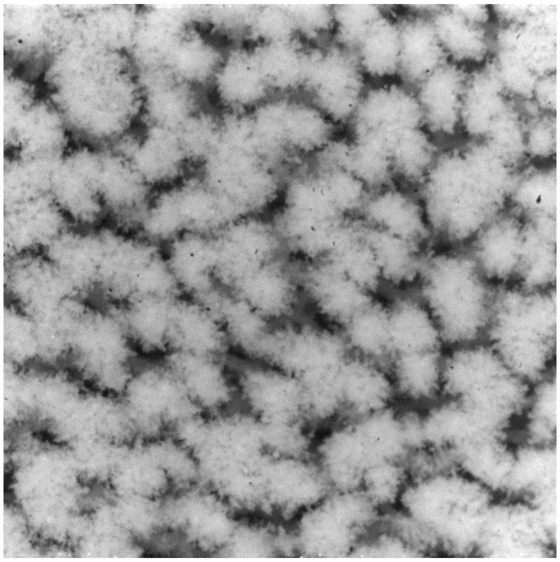

(60 mins)

20 PPI

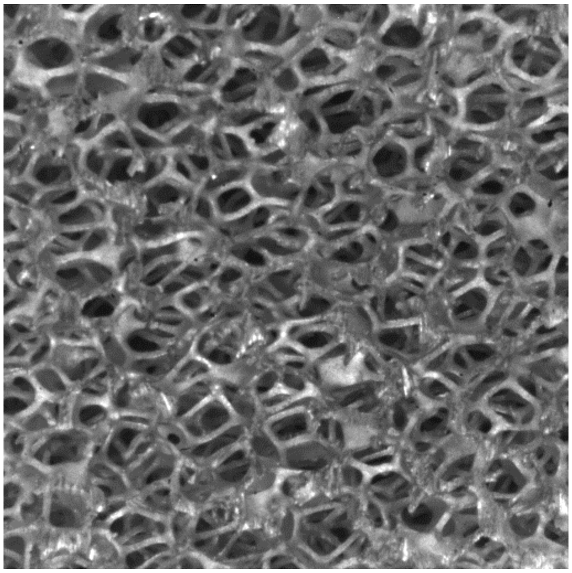

(0 mins)

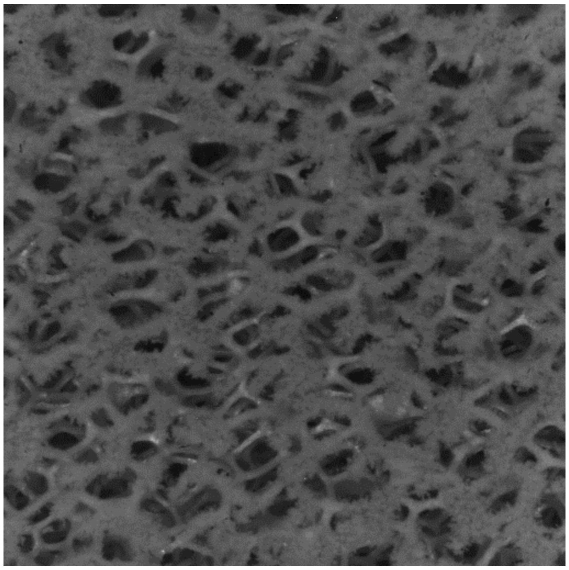

(15 mins)

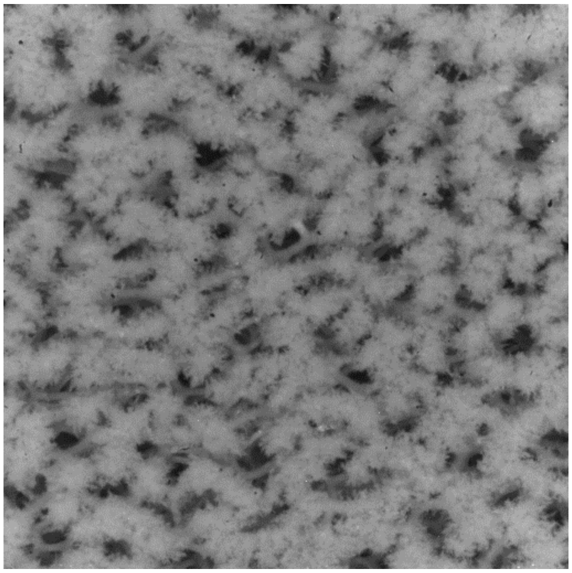

(30 mins)

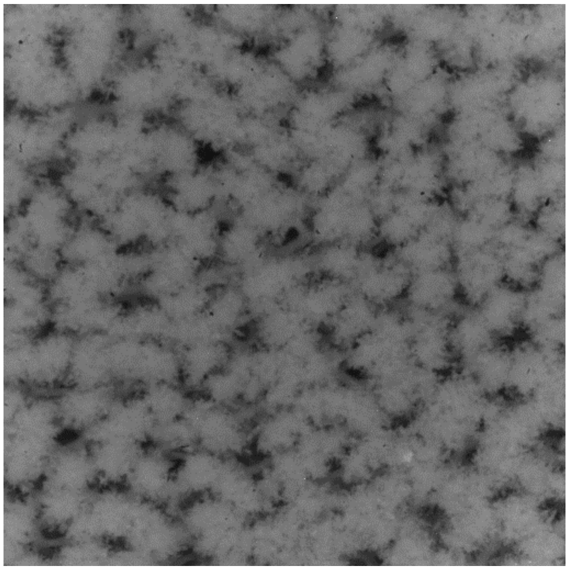

(45 mins)

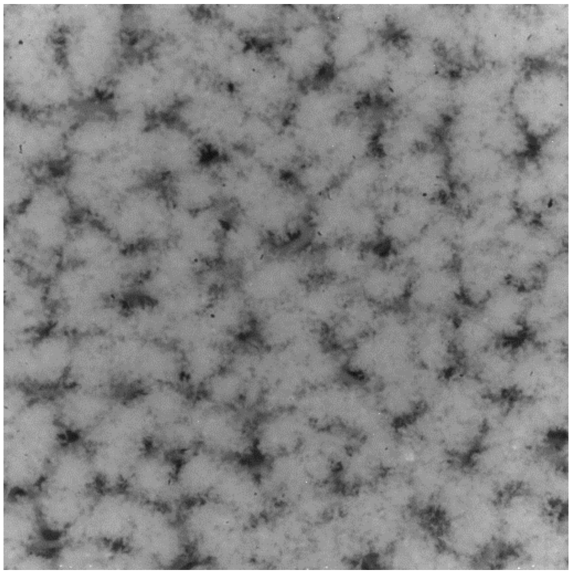

(60 mins)

40 PPI

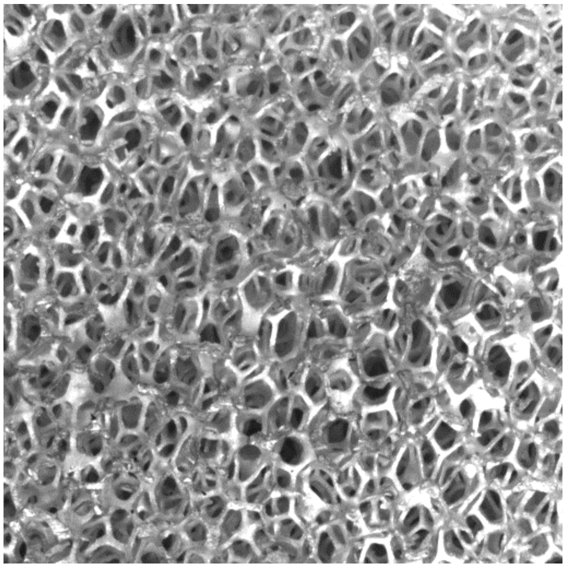

(0 mins)

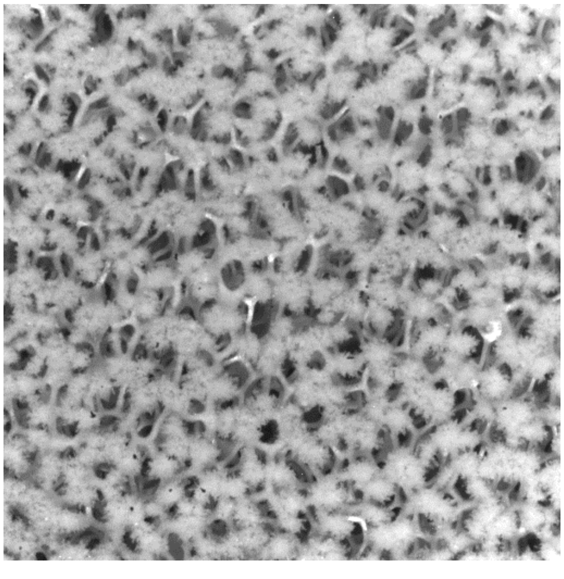

(15 mins)

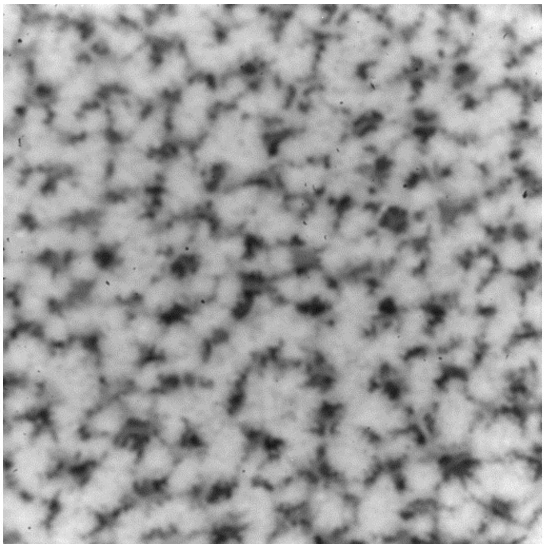

(30 mins)

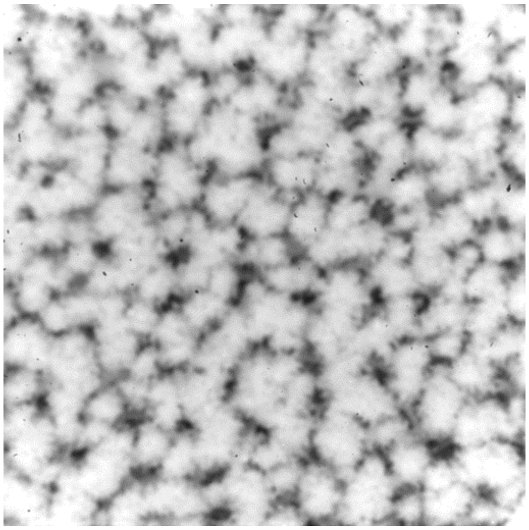

(45 mins)

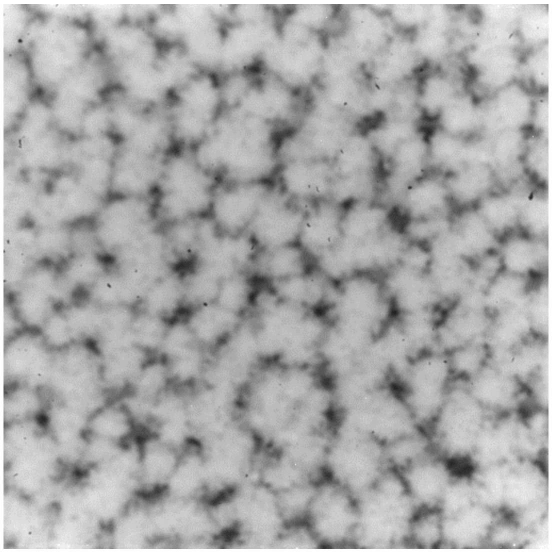

(60 mins)

Appendix I: Resulting articles

Archival Journal Articles:

1. C. T'Joen, C., Y. Park, Q. Wang, A. Sommers, X. Han, and A.M. Jacobi, "A Review on Polymer Heat Exchangers for HVAC&R Applications," International Journal of Refrigeration, 32(5): 763-779, 2009.
2. Dai, Z., K. Nawaz, Y. Park, J. Bock, and A.M. Jacobi, "Correcting and Extending the Boomsma–Poulikakos Effective Thermal Conductivity Model for Three-dimensional, Fluid-saturated Metal Foams," International Communications in Heat and Mass Transfer, 37(6): 575-580, 2010.
3. Sommers, A., Q. Wang, X. Han, C. T'Joen, Y. Park, and A.M. Jacobi, "Ceramic and Ceramic Matrix Composites for Heat Exchangers in Advanced Thermal Systems-A Review," Applied Thermal Engineering, 30:1277-1291, 2010.
4. Dai, Z., K. Nawaz, Y. Park, Q. Chen, and A.M. Jacobi, "A Comparison of Metal Foam Heat Exchangers to Compact, Multilouver Designs for Air-side Heat Transfer Applications," Heat Transfer Engineering, 33:21-30, 2012.
5. Han, X., Q. Wang, Y. Park, C. T'Joen, A. Sommers, and A.M. Jacobi, "A Review of Metal Foam and Metal Matrix Composites for Heat Exchangers and Heat Sinks," accepted, Heat Transfer Engineering, 2012.
6. Wang, Q., X.H Han, A. Sommers, Y. Park, C. T'Joen, and A.M. Jacobi, "A Review on Application of Carbonaceous Materials and Carbon Matrix Composites for Heat Exchangers and Heat Sinks," accepted International Journal of Refrigeration, 2012.

We anticipate submitting three more journal papers, one on metal foam structure and condensate retention, and a two-part paper on pressure-drop and heat transfer performance.

Reviewed Conference Proceedings:

1. Dai, Z., K. Nawaz, Y. Park, Q. Chen, and A.M. Jacobi, "A Comparison of Metal-Foam Heat Exchangers to Compact Multilouver Designs for Air-Side Heat Transfer Applications," Seventh International Conference on Enhanced, Compact and Ultra-Compact Heat Exchangers: From Microscale Phenomena to Industrial Applications, Costa Rica, 2009
2. Nawaz, K., J. Bock, Z. Dai, and A.M. Jacobi, "Experimental Studies to Evaluate the Use of Metal Foams in Highly Compact Air-cooling Heat Exchangers," 13th International Refrigeration and Air Conditioning Conference at Purdue, West Lafayette, IN., 2010.

We anticipate submitting two more conference papers, one on water retention in metal foams, and one on thermal-hydraulic performance.

Two M.S. theses have resulted from this work.